

2015

## Numerical Simulations of Reacting Flow in an Inductively Coupled Plasma Torch

Maximilian Dougherty  
*University of Vermont*

Follow this and additional works at: <https://scholarworks.uvm.edu/graddis>

 Part of the [Aerospace Engineering Commons](#), [Mechanical Engineering Commons](#), and the [Plasma and Beam Physics Commons](#)

---

### Recommended Citation

Dougherty, Maximilian, "Numerical Simulations of Reacting Flow in an Inductively Coupled Plasma Torch" (2015). *Graduate College Dissertations and Theses*. 512.  
<https://scholarworks.uvm.edu/graddis/512>

---

This Dissertation is brought to you for free and open access by the Dissertations and Theses at UVM ScholarWorks. It has been accepted for inclusion in Graduate College Dissertations and Theses by an authorized administrator of UVM ScholarWorks. For more information, please contact [scholarworks@uvm.edu](mailto:scholarworks@uvm.edu).

NUMERICAL SIMULATIONS OF REACTING FLOW IN AN INDUCTIVELY  
COUPLED PLASMA TORCH

A Dissertation Presented  
by  
Maximilian Dougherty  
to  
The Faculty of the Graduate College  
of  
The University of Vermont

In Partial Fullfillment of the Requirements  
for the Degree of Doctor of Philosophy  
Specializing in Mechanical Engineering

May, 2015

Defense date: March 16, 2015  
Dissertation Examination Committee:

Douglas Fletcher, Ph.D., Advisor  
Adrian Del Maestro, Ph.D., Chairperson  
Yves Dubief, Ph.D.  
Darren Hitt, Ph.D.  
Cynthia J. Forehand, Ph.D., Dean of the Graduate College

# Abstract

In the design of a thermal protection system for atmospheric entry, aerothermal heating presents a major impediment to efficient heat shield design. Recombination of atomic species in the boundary layer results in highly exothermic surface-catalyzed recombination reactions and an increase in the heat flux experienced at the surface. The degree to which these reactions increase the surface heat flux is partly a function of the heat shield material. Characterization of the catalytic behavior of these materials takes place in experimental facilities, however there is a dearth of detailed computational models for the fluid dynamic and chemical behavior of such facilities.

A numerical model coupling finite rate chemical kinetics and high temperature thermodynamic and transport properties with a computational fluid dynamics flow solver has been developed to model the chemically reacting flow in the inductively coupled plasma torch facility at the University of Vermont. Simulations were performed modeling the plasma jet for hybrid oxygen-argon and nitrogen plasmas in order to validate the models developed in this work by comparison to experimentally-obtained data for temperature and relative species concentrations in the boundary layer above test articles. Surface boundary conditions for wall temperature and catalytic efficiency were utilized to represent the different test article materials used in the experimental facility. Good agreement between measured and computed data is observed. In addition, a code-to-code validation exercise was performed benchmarking the performance of the models developed in this dissertation by comparison to previously published results. Results obtained show good agreement for boundary layer temperature and species concentrations despite significant differences in the codes. Lastly, a series of simulations were performed investigating the effects of recombination reaction rates and pressure on the composition of a nitrogen plasma jet in chemical nonequilibrium in order to better understand the composition at the boundary layer edge above a test article. Results from this study suggest that, for typical test conditions, the boundary layer edge will be in a state of chemical nonequilibrium, leading to a nonequilibrium condition across the entire boundary layer for test article materials with high catalytic efficiencies.

# Acknowledgements

Far from being any sort of brave solo effort, the simple fact that this dissertation exists is the result of an untold amount of support from colleagues, friends, and family.

First and foremost, thank you to everyone who called Perkins 211 home over the past six years: Walt, Andrew, Nick, Jürgen, and Steve. The utter lack of seriousness, foosball, and occasional technical discussion were invaluable and resulted in that rare occurrence of work being genuinely fun.

Thank you Crocker for all of your help with numerics, bad sci-fi, and things such as seals.

Thank you to my fellow charter members of the BNSSSDRC, Rose and Karl. Few experiences compare to finding oneself hungry, tired, and cold 8 miles from Burlington on the bike path in the dark. Making this fun can only happen with great company.

Professors Dubief and Fletcher, thank you both for your confidence in me throughout this undertaking even in the moments when all seemed lost.

Thank you to my parents for providing unwavering support and confidence throughout this entire process.

Lastly, thank you to Maria for hearing every gripe, groan, and complaint while providing steadfast and unyielding support every day.

Funding for this work has been provided by AFOSR Grant FA9550-11-1-0201 and NASA Grant NNX11AR69G.

# Table of Contents

<b>Acknowledgments .....</b>	<b>ii</b>
<b>List of Tables.....</b>	<b>vi</b>
<b>List of Figures.....</b>	<b>vii</b>
<b>List of Symbols.....</b>	<b>xii</b>
<b>Chapter 1 Introduction.....</b>	<b>1</b>
1.1 Overview of past work .. . . . .	5
1.1.1 Early correlations for stagnation point heat transfer .. . . . .	5
1.1.2 Modern approaches for modeling reentry and plasma flow .. . . . .	8
1.2 Inductively coupled plasma torch facility .. . . . .	16
1.3 Computing resources .. . . . .	18
1.4 Objective and scope of this dissertation .. . . . .	19
<b>Chapter 2 Flow solver, high temperature gas properties, and chemistry ..</b>	<b>20</b>
2.1 Navier-Stokes flow solver .. . . . .	20
2.1.1 Governing equations .. . . . .	21
2.1.2 CFL condition .. . . . .	23
2.1.3 WENO scheme for scalar transport .. . . . .	24
2.1.4 Scalar boundary conditions .. . . . .	25

2.1.5	Catalytic wall . . . . .	27
2.1.6	Outlet buffer region . . . . .	30
2.1.7	Finite rate chemistry . . . . .	31
2.1.8	Parallel partitioning . . . . .	34
2.2	High temperature gas properties . . . . .	38
2.2.1	Overview . . . . .	38
2.2.2	Equation of state . . . . .	38
2.2.3	Thermodynamic properties . . . . .	39
2.2.4	Transport properties . . . . .	42
2.2.5	Species production rates . . . . .	47
<b>Chapter 3</b>	<b>Simulations . . . . .</b>	<b>49</b>
3.1	Plasma torch geometry . . . . .	49
3.2	Reynolds number of the plasma jet . . . . .	53
3.3	Grid considerations . . . . .	55
3.3.1	Grid generation method . . . . .	55
3.3.2	Grid independence . . . . .	58
3.4	Parallel scaling . . . . .	61
3.5	Gas mixtures . . . . .	61
3.5.1	5 species air . . . . .	61
3.5.2	Oxygen - Argon . . . . .	63
3.5.3	5 species nitrogen . . . . .	65
3.6	Inlet conditions . . . . .	66
3.6.1	Velocity inlet boundary condition . . . . .	67
3.6.2	Temporal inlet velocity ramping . . . . .	69
3.6.3	Temperature and species inlet boundary conditions . . . . .	69
3.7	Velocity field initialization from analytical solution . . . . .	70

<b>Chapter 4 Results .....</b>	<b>73</b>
4.1 Experimental technique . . . . .	74
4.1.1 Calculation of temperature and relative mole fractions . . . . .	76
4.1.2 Determination of TPS material catalytic efficiencies . . . . .	77
4.2 Argon-buffered oxygen mixture in UVM ICP facility . . . . .	79
4.2.1 Copper test article, $T_{\infty} = 5000$ K, $T_w = 650$ K . . . . .	80
4.2.2 Cold quartz test article, $T_{\infty} = 4500$ K, $T_w = 800$ K . . . . .	82
4.2.3 $\alpha$ -SiC test article, $T_{\infty} = 4500$ K, $T_w = 1500$ K . . . . .	86
4.3 Pure nitrogen in UVM ICP facility . . . . .	91
4.3.1 Copper, $T_{\infty} = 6000$ K, $T_w = 650$ K . . . . .	92
4.3.2 Cold quartz test article, $T_{\infty} = 6000$ K, $T_w = 800$ K . . . . .	94
4.3.3 $\alpha$ -SiC test article, $T_{\infty} = 6000$ K, $T_w = 1500$ K . . . . .	96
4.4 Code-to-code validation of UVM ICP facility model . . . . .	99
4.5 Effects of nonequilibrium behavior of nitrogen on plasma jet composition .	105
4.5.1 Effect of varying N atom recombination reaction rates . . . . .	107
4.5.2 Effect of varying pressure on plasma jet composition and temperature	114
<b>Chapter 5 Summary and future work .....</b>	<b>123</b>
5.1 Contributions of this dissertation . . . . .	123
5.2 Recommendations for future work . . . . .	124
<b>Appendix A Reaction constants for O<sub>2</sub> / Ar hybrid mixture.....</b>	<b>126</b>
<b>Appendix B Reaction constants for 5 species N<sub>2</sub> mixture.....</b>	<b>127</b>
<b>Appendix C Reaction constants for 5 species air mixture.....</b>	<b>128</b>
<b>References.....</b>	<b>129</b>

# List of Tables

1.1	Plasma torch operating parameters . . . . .	17
3.1	Relevant geometric parameters. . . . .	51
3.2	Grid parameters for independence study. . . . .	58
4.1	Conditions for O <sub>2</sub> -Ar simulations. . . . .	79
4.2	Conditions for N <sub>2</sub> simulations . . . . .	91
4.3	Conditions simulated for comparison between NGA and LEMANS.. . . . .	99
4.4	Inlet conditions for N <sub>2</sub> nonequilibrium simulations. . . . .	105
4.5	Pressures used for N <sub>2</sub> nonequilibrium simulations. . . . .	114
A.1	Reaction rates for 7 species O <sub>2</sub> -Ar mixture. . . . .	126
B.1	Reaction rates for 5 species N <sub>2</sub> mixture. . . . .	127
C.1	Reaction rates for 5 species air mixture. . . . .	128

# List of Figures

1.1	Flow regimes and thermochemical behavior in the stagnation region of a 30.5 cm sphere in air from Gupta [1]. . . . .	4
1.2	Schematic of full ICP torch facility including power supply and gas supply [2].	17
2.1	Schematic of staggered grid with vector quantities at cell faces and scalars at cell centers. [3] . . . . .	21
2.2	Window function (equation 2.30) used to scale computed change in density in outlet buffer region. . . . .	31
2.3	Diagram showing partitioning of processors along $x$ , $y$ , and $z$ directions for a computational domain with $npx = npy = npz = 2$ . The solid lines represent the boundaries of the domain and regions within the dashed lines indicate the partitions created for each processor. . . . .	35
2.4	Parallel partitioning in NGA for a simple one dimensional domain with 2 processors. The filled circles represent nodes within the flow and the outlined circles represent the ghost nodes. . . . .	37
2.5	Equilibrium and frozen specific heats and species mass fractions of a binary oxygen mixture at 10 kPa. . . . .	42
2.6	Comparison of dynamic viscosity computed with MUTATION++ and Sutherland's formula. . . . .	45

3.1	Schematic of the plasma torch test chamber. Diameter and height of chamber are not to scale in order to preserve clarity for quartz tube and sample. . . . .	50
3.2	View of plasma jet within test chamber. In this image, $L_{jet}$ is approximately 110 mm [4]. . . . .	52
3.3	View of plasma jet within test chamber for a significantly smaller value of $L_{jet}$ , approximately 50 mm [4]. . . . .	52
3.4	Schematic of a 25mm test article used for hot wall measurements. [5] . . . . .	53
3.5	Facility Reynolds number based on sample diameter. . . . .	54
3.6	Grid for cases with a sample in the flow. Generated using equations 3.2-3.5 at low resolution ( $64 \times 64$ ) for clarity. Here, $r_x = 1.9$ and $r_y = 2.0$ . . . . .	57
3.7	Grid for a free jet with no obstacle in the flow. Generated using equations 3.2-3.5 at low resolution ( $64 \times 64$ ) for clarity. For this grid, $r_x = 0.001$ and $r_y = 2.0$ . . . . .	57
3.8	Boundary layer temperature profile computed with varying grid resolution.	59
3.9	$L_2$ error norm for temperature plotted against grid resolution, $N = N_x = N_y$ . Near second order convergence is achieved with $m = -1.92$ . . . . .	60
3.10	Major species mass fractions for 5 species air mixture. . . . .	62
3.11	Major species mass fractions for 11 species air mixture. . . . .	62
3.12	Minor species mass fractions for 5 species air mixture. . . . .	63
3.13	Minor species mass fractions for 11 species air mixture. . . . .	63
3.14	Mole fractions for O <sub>2</sub> / Ar mixture in LTE. . . . .	64
3.15	Log plot of mole fractions for O <sub>2</sub> / Ar mixture in LTE. . . . .	64
3.16	Mole fractions for 5 species N <sub>2</sub> mixture in LTE. . . . .	65
3.17	Log plot of mole fractions for 5 species N <sub>2</sub> mixture in LTE. . . . .	65
3.18	Inlet $U$ velocity profile computed from equation 3.9 with $R_{inlet} = 0.018$ [m], representative of UVM ICP facility geometry. . . . .	68
3.19	Profile of axial velocity field for simulation initialization, from equation 3.13.	71

3.20	Contours of velocity for initial field calculated using equation 3.13.	72
3.21	Contours of velocity for fully-developed, steady plasma jet.	72
4.1	Schematic of TALIF measurement configuration in the UVM ICP facility. [6]	75
4.2	Schematic of stagnation point measurement location for temperature and species composition.	76
4.3	Temperature profile for case O <sub>2</sub> /Ar-1.	80
4.4	Relative O atom mole fraction from simulations compared to measured LIF data for case O <sub>2</sub> /Ar-1.	81
4.5	Temperature profile from simulation compared with LIF data for case O <sub>2</sub> /Ar-2	83
4.6	Relative O atom mole fraction from simulations compared to measured LIF data for case O <sub>2</sub> /Ar-2.	84
4.7	Detailed view of the 0.1 mm region above the sample surface to show slight differences in curves for $\gamma = 0$ and $\gamma = 0.000582$ for case O <sub>2</sub> /Ar-2.	85
4.8	Temperature profile from simulation compared with LIF data for case O <sub>2</sub> /Ar-3, $\gamma = 0.001057$ .	86
4.9	Relative O atom mole fraction from simulations compared to measured LIF data for case O <sub>2</sub> /Ar-3, $\gamma = 0.001057$ .	87
4.10	Temperature profile from simulation compared with experimental data for case O <sub>2</sub> /Ar-4, $\gamma = 0.003579$ .	88
4.11	Relative O atom mole fraction from simulations compared to measured LIF data for case O <sub>2</sub> /Ar-4, $\gamma = 0.003579$ .	89
4.12	Temperature profile from simulation compared with LIF data for case N <sub>2</sub> -1, $\gamma = 0.0173$ .	92
4.13	Relative N atom mole fraction from simulations compared to measured LIF data for case N <sub>2</sub> -1, $\gamma = 0.0173$ .	93
4.14	Temperature profile from simulation compared with LIF data for case N <sub>2</sub> -2, $\gamma = 0.000755$ .	94

4.15	Relative N atom mole fraction from simulations compared to measured LIF data for case N <sub>2</sub> -2, $\gamma = 0.000755$ . . . . .	95
4.16	Temperature profile from simulation compared with LIF data for case N <sub>2</sub> -3, $\gamma = 0.00587$ . . . . .	97
4.17	Relative N atom mole fraction from simulations compared to measured LIF data for case N <sub>2</sub> -3, $\gamma = 0.00587$ . . . . .	98
4.18	Temperature profiles from NGA and LEMANS for $\gamma = 0, 1$ . . . . .	101
4.19	Temperature profiles for $\gamma = 0.0$ from NGA and LEMANS. . . . .	102
4.20	Temperature profiles for $\gamma = 1.0$ from NGA and LEMANS. . . . .	102
4.21	Relative nitrogen atom number density profiles from NGA and LEMANS for varying $\gamma$ values. . . . .	103
4.22	Contours of nitrogen atom mass fraction for LTE inlet conditions, $T_{in} = 6000K$ .107	
4.23	Mass fraction of N atom along plasma jet axis for varying inlet conditions. .	108
4.24	Mass fraction of N atom along plasma jet axis for varying inlet conditions. .	109
4.25	Temperature along plasma jet axis for varying values of $k_f$ . . . . .	110
4.26	Mass fraction of N atom along plasma jet axis for $k_f = k_f/10$ . . . . .	111
4.27	Mass fraction of N atom along plasma jet axis for $k_f$ at published value. .	112
4.28	Mass fraction of N atom along plasma jet axis for $k_f = 10k_f$ . . . . .	113
4.29	Mass fraction of N atom along plasma jet axis for varying pressures. . . . .	115
4.30	Mass fraction of N atom along plasma jet axis for varying pressures. Zoomed to the first 5 cm of the simulated domain to more clearly show nonequilibrium behavior near inlet. . . . .	116
4.31	Temperature along plasma jet axis for varying pressures. . . . .	117
4.32	Nonequilibrium mass fraction of N atom along plasma jet axis compared to LTE values at 10132 Pa. . . . .	118
4.33	Nonequilibrium mass fraction of N atom along plasma jet axis compared to LTE values at 15198 Pa. . . . .	119

4.34 Nonequilibrium mass fraction of N atom along plasma jet axis compared to LTE values at 20264 Pa. . . . .	120
4.35 Nonequilibrium mass fraction of N atom along plasma jet axis compared to LTE values at 30396 Pa. . . . .	121

# List of symbols

## Acronyms

AHF	Arc Heating Facility
ARTS	Advanced Reactive Turbulent Simulator
CFD	Computational Fluid Dynamics
DPLR	Data Parallel Line Relaxation
EAST	Electric Arc-Driven Shock Tube
GSLR	Gauss-Seidel Line Relaxation
HYPRE	High Performance Preconditioners
ICP	Inductively Coupled Plasma
LHTS	Local Heat Transfer Simulation
LAURA	Langley Aerothermodynamic Upwind Relaxation Algorithm
LTE	Local Thermodynamic Equilibrium
MPI	Message Passing Interface
MUTATION	Multi-component Transport And Thermodynamic Properties / chemistry for Ionized Gases
NGA	Next Generation ARTS
PEGASE	Perfect Gase Equation
RF	Radio frequency
TPS	Thermal Protection System
VACC	Vermont Advanced Computing Core
WENO	Weight Essentially Non-Oscillatory

## Roman symbols

Symbol	Units	Description
$C$	—	Courant number
$c_p$	J kg <sup>-1</sup> K <sup>-1</sup>	Specific heat at constant pressure
$C_i$	mol m <sup>-3</sup>	Molar concentration of species $i$
$C_f$	m <sup>3</sup> kg <sup>-1</sup> s <sup>-1</sup>	Arrhenius rate equation pre-exponential factor
$d_{inlet}$	m	Diameter of plasma jet inlet
$d_{sample}$	m	Diameter of test sample

$\mathcal{D}_{i,j}$	$\text{m}^2 \text{ s}^{-1}$	Binary diffusion coefficient of species $i, j$
$h$	$\text{J kg}^{-1}$	Mixture enthalpy
$h_D$	$\text{J kg}^{-1}$	Dissociation enthalpy
$h_i$	$\text{J kg}^{-1}$	Enthalpy of species $i$
$\Delta h_{F,i}$	$\text{J kg}^{-1}$	Standard enthalpy of formation of species $i$
$h(x)$	—	Window function for $\partial\rho$ scaling
$\vec{J}$	$\text{m}^{-1}$	Diffusion flux of species $i$
$k_b$	—	Backward reaction rate coefficient
$k_f$	—	Forward reaction rate coefficient
$K_{eq}$	—	Equilibrium constant
$L$	$\text{m}$	Length of computational domain
$L_{jet}$	$\text{m}$	Distance from inlet to sample surface
$Le$	—	Lewis number
$m_i$	$\text{kg}$	Mass of species $i$
$\mathcal{M}_i$	$\text{kg mol}^{-1}$	Molar mass of species $i$
$M_i$	$\text{kg}$	Molecular weight of species $i$
$Ma$	—	Mach number
$\vec{n}$	$\text{m}$	Wall-normal coordinate
$n$	$\text{m}^{-3}$	Mixture number density
$n_i$	$\text{m}^{-3}$	Number density of species $i$
$\hat{n}_i$	$\text{m}^{-3}$	Relative number density of species $i$
$n_x, n_y$	—	Number of grid points in $x$ and $y$ directions
$N_A$	$\text{mol}^{-1}$	Avogadro's number
$N_{sp}$	—	Number of species in a mixture
$Nu$	—	Nusselt number
$P, p$	$\text{Pa}$	Pressure
$\dot{Q}$	—	Scalar source term in residual form
$r$	$\text{m}$	Radial coordinate
$r_x, r_y$	—	Grid stretching factors in $x, y$
$R_u$	$\text{J mol}^{-1} \text{ K}^{-1}$	Universal gas constant
$s$	—	Maximum slope of window function
$\mathbf{u}$	$\text{m s}^{-1}$	Velocity vector
$T$	$\text{K}$	Temperature
$x_i$	—	Mole fraction of species $i$
$y_i$	—	Mass fraction of species $i$
$Z$	—	Transported scalar

## Greek symbols

Symbol	Units	Description
$\alpha_i$	$\text{kg m}^{-1} \text{ s}^{-1}$	Diffusivity of species $i$
$\gamma$	—	Catalytic efficiency
$\Gamma_i$	$\text{m}^{-3} \text{ s}^{-1}$	Net flux of species $i$ at the wall
$\epsilon$	$\text{m}$	Length of $\partial\rho$ buffer region

$\zeta$	—	Coordinate matrix in computational space
$\eta$	—	Transformed boundary layer coordinate
$\lambda$	$\text{W m}^{-1} \text{ K}^{-1}$	Mixture thermal conductivity
$\mu$	$\text{Pa s}$	Dynamic viscosity
$\nu_{i,j}$	—	Stoichiometric matrix for species $i$ in reaction $j$
$\xi$	—	Transformed boundary layer coordinate
$\rho$	$\text{kg m}^{-3}$	Mixture density
$\rho_i$	$\text{kg m}^{-3}$	Density of species $i$
$\sigma$	—	Prandtl Number
$\chi_i$	—	Mole fraction of species $i$
$\hat{\chi}_i$	—	Relative mole fraction of species $i$
$\dot{\omega}_i$	$\text{kg m}^{-3} \text{ s}^{-1}$	Net production rate of species $i$
$\omega_{x^+}, \omega_{x^-}$	—	Weighting coefficient for WENO scheme
$\Omega_{i,j}^{p,q}$	—	Collision integral ( $p, q$ ) for species $i, j$

## Subscripts

0	Thermodynamic reference condition
$\delta, e$	Boundary layer edge
$e$	Electron
$h$	Heavy particle
$i, j, k$	coordinate index, species index
$int$	Internal
$m$	Cell mid-point value
$p$	Value at constant pressure
$s$	Stagnation point value
$w$	Wall value

## Superscripts

$\epsilon$	Lees-Dorodnitsyn parameter
$k$	subiteration index

# Chapter 1

## Introduction

The design of thermal protection systems (TPS) for missions involving atmospheric entry to other planets and reentry to the Earth's atmosphere is an ongoing challenge. During atmospheric entry, a vehicle traveling at hypersonic speeds creates a bow shock which causes the ambient atmosphere to drastically increase in temperature and thus dissociate and ionize as it passes through the shock. In the post-shock region, the gas tends toward thermochemical equilibrium towards the vehicle surface, however it is generally accepted that within the boundary layer, the gas does not achieve equilibrium. This condition results in recombination of atomic species at the surface, often by way of highly exothermic reactions. These reactions can significantly increase the heat flux experienced by the heat shield relative to an equilibrium condition. Owing to insufficient knowledge of material catalycity, conservative design methodologies are employed with regard to predicted heat transfer such that the heat shield mass must be increased at the expense of the scientific payload.

Determination of the response of TPS materials to the high temperatures encountered during planetary (re)entry poses significant challenges. Using experimental techniques, it is not possible to fully recreate the flow encountered by an entry vehicle in a laboratory setting and instead, it is considered sufficient to match the post-shock total pressure, total enthalpy, and stagnation point velocity gradient. Various types of facilities exist for this,

chiefly among them are arc-jets and inductively coupled plasma torches. Although unable to match flight conditions exactly, both types of facilities are able to operate in supersonic configurations and generate high surface heat flux rates, effectively replicating the post-shock nonequilibrium boundary layer above the TPS material.

Arc-jets generate a supersonic plasma flow by running a large current between copper electrodes, a method which can potentially introduce contaminants into the flow in the form of molten copper. In North America, arc-jets represent the dominant form of plasma wind tunnel used to study (re)entry flows. Some of these facilities are NASA's Ames Arc Heating Facility (AHF) and Interaction Heating Facility (IHF), the NASA Johnson Arc Jet Complex, and the Boeing Large Core Arc Tunnel. CIRA's SCIROCCO facility and the DLR LBK and L3K are some of the few arc-jets in use in Europe.

Inductively coupled plasma (ICP) torches create plasma via induction heating within a quartz tube upstream of the test chamber (this is explained in great detail in [2]). One of the primary benefits of induction heating relative to arc heating is that no contaminants are introduced into the plasma, ensuring that the test gas composition is known, making them preferable for studying chemical behavior in the flow. ICP facilities represent the dominant form of ground test facility in Europe. Examples of these include the Von Karman Institute's 15 kW Minitorch facility, the 1.2 MW Plasmatron facility, and the 100 kW ICP torch at the Institute for Problems in Mechanics in Moscow. In North America, the University of Vermont ICP torch is the only facility of its kind used for testing TPS materials. It is worth noting briefly that ICP technology has many industrial applications, including ICP mass spectrometry and reactive ion etching for semiconductor production, however these topics are not considered here.

Shock tubes represent another common type of facility used to study atmospheric entry flows. Unlike arc-jets and ICP torches, they are able to achieve high hypersonic speeds, however test durations are extremely short: the upper limit is on the order of milliseconds. Conversely, ICP torches and arc-jets allow to test durations greater than one hour. Some

examples of shock tube facilities are the Von Karman Institute Longshot and NASA's Electric Arc-driven Shock Tube (EAST).

In the computational realm, there is no shortage of capable flow solvers available in the commercial or open source domains suitable for modeling high Mach number reentry flows. However, there exists a dearth of solvers coupled with the ability to handle finite rate chemistry and high temperature thermodynamic and transport properties necessary for accurate simulations of subsonic plasma flow within a ground test facility. This problem is treated in the present work.

Unlike ground-based experiments, the scope of simulations can be much more wide-ranging. The two main areas of interest are the simulation of full flight conditions and geometry and simulating the behavior of ground test facilities. These present two drastically different flow regimes. In the case of (re)entry flow, the vehicle is traveling at hypersonic speeds (5-25 km/s, depending on the mission, see Figure 1.1) and the flow is typically in thermal nonequilibrium. Accurate simulation of this requires numerical schemes capable of handling the large gradients that accompany shocks and the use of multiple temperatures for the chemical species. Depending on the atmospheric composition and temperature range, a radiation model may be required, significantly increasing the complexity and computational cost of the simulation.

Regions with chemical and thermal nonequilibrium		Chemical species in high-temperature air	
Region	Aerothermal phenomenon	Region	Air chemical model
(A)	Chemical and thermal equilibrium	I	2 species $O_2, N_2$
(B)	Chemical nonequilibrium with thermal equilibrium	II	5 species $O_2, N_2, O, N, NO$
(C)	Chemical and thermal nonequilibrium	III	7 species $O_2, N_2, O, N, NO, NO^+, e^-$
		IV	11 species $O_2, N_2, O, N, NO, O_2^+, N_2^+, O^+, N^+, NO^+, e^-$

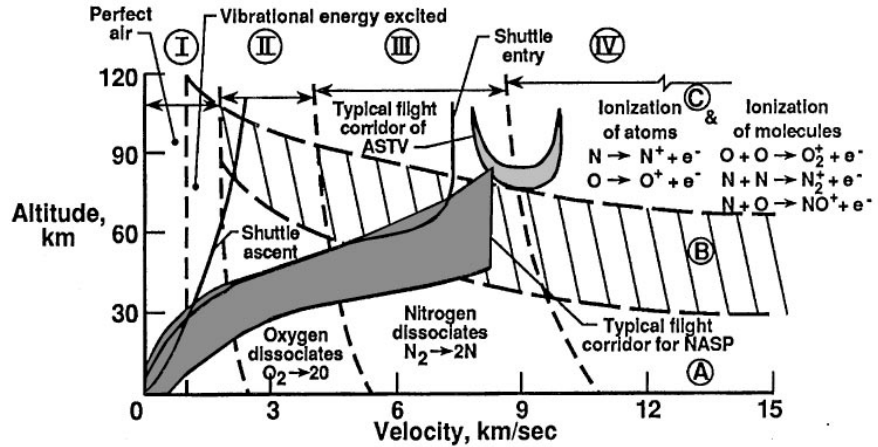


Figure 1.1: Flow regimes and thermochemical behavior in the stagnation region of a 30.5 cm sphere in air from Gupta [1].

Ground test facilities feature a very different regime of high-enthalpy flow: the flow speeds are much lower, often subsonic for ICP facilities, and while the plasma may be in chemical nonequilibrium, the degree of thermal nonequilibrium is relatively weak owing to the modest pressures; thus the use of a single temperature model suffices. Owing to these differences, specifically the subsonic nature of ICP flows, many codes used to study flight conditions employ numeric schemes designed for high speed (Mach number  $> 1$ ) flow which are not directly applicable to the simulation of ground test facilities. Previous studies of inductively coupled plasma torch facilities have included models for the electromagnetic forces, including the magnetic and electric fields generated by the induction coil and the heating of the test gas, although this is not strictly necessary when the regions of interest are the bulk flow of the plasma jet or the boundary layer above a test article. The elec-

tromagnetic forces relevant to plasma generation occur within the induction region of the ICP torch. Outside of this region, it is sufficient to model the plasma as a dissociated gas comprised of multiple chemical species.

## 1.1 Overview of past work

Atmospheric reentry became an active area of research during the 1940s and 1950s, when the driving force for the field was ensuring the survival of ballistic missiles as they approached their targets [7]. With the advent of manned missions to space in the late 1950s, the field began to shift towards its present state. While the bulk flow in this regime presented its own challenges, interest in the behavior of the boundary layer and the resultant stagnation point heat transfer built the foundation for modern research in the field of reentry aerothermodynamics.

Much of the early effort toward characterizing reentry flows resulted in the development of correlations for surface heat transfer instead of direct computations, owing to the absence of computing power at that time. For the same reason, all early numerical studies relied on simplified equation sets, taking the form of coordinate transformations based on similarity for boundary layer flow. These can be viewed as significantly more advanced cousins of the Blasius boundary layer solution which include terms for temperature and the composition of the gas in terms of chemical species. These approaches are valid but as a result of their reduced form, they lack detailed information about the behavior of the flow. As such, they are not suitable for detailed study when compared to modern computational fluid dynamics (CFD) methods.

### 1.1.1 Early correlations for stagnation point heat transfer

One of the earliest treatments of heat transfer during reentry is Lees' 1956 paper [8] which focused on two limiting cases for laminar heat transfer over a blunt-nosed body: 1) local thermodynamic equilibrium (LTE) with chemical reactions being considered very fast

relative to a characteristic convective timescale; and 2) diffusion as rate-limiting whereby recombination reactions take place more slowly than diffusion across streamlines, *i.e.* the case of frozen flow. In the LTE case, it is assumed that all heat transfer to the surface takes place by way of conduction. In the case of diffusion as rate-limiting, the heat transfer results from both conduction and heat released by atoms recombining on the surface. For the LTE regime, Lees determined that the heat transfer to the surface could be obtained directly from the surface pressure distribution. For a frozen flow, it was found that the maximum value of the heat transfer resulting from either diffusion or conduction could be related to one another by the Lewis number

$$\text{Le} = \left( \frac{\rho D_{12} c_p}{\lambda} \right)_w^{2/3} \quad (1.1)$$

where  $\rho$  is the gas density,  $D_{12}$  is a binary diffusion coefficient,  $c_p$  is the specific heat at constant pressure, and  $\lambda$  is the thermal conductivity, with all quantities taken at the wall. This term effectively represents the ratio of diffusive to conductive heat transfer and in the case of frozen flow, was found to be equal to about 1.3, implying that diffusion is the dominant mechanism for heat transfer. In the LTE regime, it was determined that the heat transfer rate was independent of the mechanism and this term was equal to 1.

The 1958 work of Fay and Riddell [9] expanded upon Lees' work by developing a set of transformed boundary layer equations for a general condition wherein the state of the flow could be considered on the spectrum between frozen and equilibrium. This was accomplished by introducing a gas phase recombination rate parameter as a function of the chemical rate constant for atomic recombination, pressure, temperature, and velocity gradient at the stagnation point. This parameter indicates the chemical behavior of the flow such that a null value represents frozen flow with no gas phase recombination and an infinite value represents the LTE condition. The effects of the recombination rate parameter were studied at the two extremes and with finite recombination rates for the limiting wall cases of a non-catalytic wall, on which no recombination takes place, and a catalytic wall which forces the chemical composition at the wall to the LTE state at the wall temperature. This

differs from later work in which the wall catalycity is varied but the chemical reaction rates are allowed to proceed at normal speed.

More notably, this work produced the well-known correlation for stagnation point heat transfer for equilibrium flow:

$$q = 0.76\sigma^{-0.6} (\rho_\delta \mu_\delta)^{0.1} (\rho_w \mu_w)^{0.4} \left[ 1 + (\text{Le}^{0.52} - 1) \left( \frac{h_D}{h_\delta} \right) \right] \sqrt{\left( \frac{du_\delta}{dx} \right)_w} \quad (1.2)$$

where  $\sigma$  is the Prandtl number,  $\mu$  is the gas viscosity, and  $h$  is the mixture enthalpy, and  $h_D$  is the dissociation enthalpy. The subscript  $\delta$  refers to quantities taken at the boundary layer edge and  $w$  denotes the wall values, both at the stagnation point. However, because this expression does not apply for nonequilibrium flow, a heat transfer parameter was introduced, defined as:

$$\frac{\text{Nu}}{\sqrt{\text{Re}}} = \left( \text{Le}^n - 1 \frac{h_D}{h_e} \right) \quad (1.3)$$

where  $n = 0.52$  for equilibrium flow and  $0.63$  for nonequilibrium flow (both determined from correlations) and Nu and Re are the Nusselt and Reynolds numbers. Using this parameter, it was determined that for a catalytic wall and a Lewis number near 1, the chemical state of the gas does not drastically effect the resultant heat transfer at the surface. Conversely, for a non-catalytic wall, the heat transfer is significantly decreased. This finding is supported by practically all later results and marks the beginnings of work studying wall catalycity in earnest.

Goulard's paper from later in 1958 [10] built upon the work of Fay and Riddell while investigating the effects of wall catalycity with the assumption of frozen flow. Goulard recognized that Fay and Riddell's catalytic wall was actually an extreme limiting case (identical, in fact, to the modern assumption of a supercatalytic wall) and as such emphasized the effects of finite surface recombination rates on stagnation point heat transfer. It was noted that at the wall, the net flux of atoms is the result of diffusion alone (expressed in the form of Fick's law) and thus the chemical boundary condition could be set to a diffusive flux scaled by a catalytic speed. Thus, the commonly used recombination efficiency  $\gamma$  was

introduced, defined as the ratio of atoms recombining at the wall to the total number of atoms striking the wall.

Taking the same approach as Fay and Riddell, Goulard characterized the heat transfer in terms of a non-dimensional parameter, in this case written as:

$$\frac{\text{Nu}}{\sqrt{\text{Re}}} = 0.664\sigma^{1/3} \left[ 1 + \left( \text{Le}^{2/3}\phi - 1 \right) \frac{h_w c_w}{h_\delta} \right] \quad (1.4)$$

where  $\phi$  is a correlation factor based on the Schmidt number, the velocity gradient, the catalytic speed, and the gas viscosity and density. Results obtained with this correlation were found to match both Lees' and Fay and Riddell's work, while also being able to study the effects of wall catalycity. Wall temperature was determined to have a positive effect on recombination, such that if wall temperature were allowed to increase, it would lead to greater rates of recombination, resulting in more heat transferred to the surface; ultimately an undesirable situation for any reentry vehicle. This finding holds true to the extent that increasing temperature has a positive relation to reaction rates. However, beyond a certain point an increasing wall temperature would lead to less recombination because the composition would trend towards a state with higher dissociation.

### 1.1.2 Modern approaches for modeling reentry and plasma flow

During the early 1980s, much of the computational efforts were of a more theoretical nature, with the two main advances being work with parabolized Navier-Stokes equations and improved methods for modeling viscous shock layers. Later in the decade, the field saw improvement in upwinding schemes and scalar transport schemes suitable for high-temperature, reacting flow. Preliminary studies towards the simulation of inductively coupled plasma were also performed [11] well outside of the field of atmospheric entry. These studies did, however, provide an initial basis for the notion that the flow in the induction region of an ICP torch is in equilibrium. A thorough history of this period can be found in Gnoffo's detailed report on computational aerothermodynamics [12] but the remainder of this review will focus on the more recently developed methods focusing on applications.

Originally developed in the late 1980s, the Langley Aerothermodynamic Upwind Relaxation Algorithm (LAURA) [13] was designed at NASA for the simulation of hypersonic flow during atmospheric entry. It is built around a structured grid, finite volume solver with a symmetric total variation diminishing algorithm for the inviscid flux, allowing it to accurately capture shocks. It includes finite rate chemistry capability for dissociated and ionized gas mixtures, as well as equilibrium models for air and a two temperature model for thermal nonequilibrium. The Stefan-Maxwell equations are included for multi-component diffusion [14]. Owing to its longevity, it has undergone many improvements: notably the non-trivial task of converting it from its original design for multiprocessor vector-based computers to the modern, parallelized Message Passing Interface (MPI) standard. LAURA has been used for aerothermodynamic calculations for many NASA missions, including the Shuttle Orbiter, Mars Pathfinder, and Single Stage to Orbit (SSTO) [15]. More recently, it has been coupled with the HARA radiation code [16] for a more complete description of the heating taking place in certain flow regimes. It has also recently been used for the simulation of arc jet facilities [17], but to the author’s knowledge has not been used to simulate a subsonic ICP torch facility.

The Data Parallel Line Relaxation (DPLR) code [18] developed at the University of Minnesota was designed for hypersonic applications and utilized improvements on the Gauss-Seidel line relaxation method (GSLR). The DPLR method achieves parallel efficiency by replacing the Gauss-Seidel sweep, which exhibit a data dependence between processors, with line relaxation steps. The nature of this method allows for extremely high aspect ratio cells ( $\frac{\Delta x}{\Delta y} \sim 1.25 \times 10^5$ ) near the surface which are required to adequately resolve the boundary layer in a hypersonic flow regime. In addition to the standard gas phase chemistry, its surface chemistry models range from the use of a specified catalytic efficiency to finite rate surface kinetics. The latter can be applied with great detail using the model of Marschall [19]. The line-by-line radiation code NEQAIR has been coupled to DPLR and it was found that the inclusion of a radiant source term significantly reduces the heat load experienced

during reentry and also brings the bow shock closer to the body [20]. Unlike LAURA, DPLR has been used for subsonic simulations: the 2008 work of Pejakovic *et al.* [21] utilized DPLR to model experiments characterizing nitric oxide production from oxygen and nitrogen recombination within a diffusion tube side-arm reactor. The results were found to be in good agreement with the experimental data, despite DPLR's original design goal of simulating hypersonic flow. Although DPLR has not been used to simulate an ICP torch, the diffusion tube reactor experiments indicate that this should be possible.

The 1999 doctoral dissertation of Bottin [22] presented the PEGASE (Perfect Gas Equation) thermodynamic and transport property library and a fully implicit finite volume flow solver to work towards a model of the Von Karman Institute's Plasmatron facility. The MUTATION++ gas library used in the present work is effectively a third-generation descendent of PEGASE. As with the codes that came after it, PEGASE employed kinetic theory for the calculation of transport properties and statistical thermodynamics for thermodynamic properties. Although PEGASE had finite rate chemistry capability, Bottin determined that for engineering purposes, only the two extremes of frozen and equilibrium flow required examination. Furthermore, the code was written employing the Euler equations, under the assumption that viscous effects, too, were beyond the scope of an engineering model. Thus, a quasi-1D formulation was utilized and tested for subsonic, transonic, and supersonic nozzles. The assumption of chemical equilibrium in ICP flow is generally assumed to be valid within the induction region of the torch and jet exit, as will be seen shortly, but is not applicable to the boundary layer above a test article. Despite the simple nature of Bottin's simulations, PEGASE represented a significant step forward for easily-portable, detailed gas property libraries.

Utilizing the PEGASE library, Degrez [23] presented a thorough model for an inductively coupled plasma, including the calculation of magnetohydrodynamic effects in the induction region. An 11 species air mixture was used to study the plasma behavior exclusively within the heating chamber (*i.e.* the induction region or quartz tube) of the Plasmatron

facility. Three flow regimes were studied: LTE with constant elemental fractions and two different chemical kinetics models (Park rates implemented by Gnoffo [24] and Selle [25]). It was found that within this region, the thermal and chemical behavior of the flow using a nonequilibrium model closely matched the equilibrium case using the rates of Selle, but it was suspected that the absence of thermal nonequilibrium in the Gnoffo/Park model contributed to a more significant difference in composition from the equilibrium flow. These results support the approach in the current work wherein the flow conditions at the jet exit are assumed to be in thermochemical equilibrium.

The PEGASE library was again used in Barbante's work developing an axisymmetric boundary layer code for bodies of revolution developed at the Von Karman Institute [26] [27]. Unlike previous work utilizing PEGASE, the intent of this code was the simulation of actual reentry conditions rather than ICP torch behavior. The boundary layer equations were reduced to an axisymmetric form with the Lees-Dorodnitsyn transformation, which maps physical coordinates into a computational space that implicitly accounts for boundary layer growth through the following relations:

$$\xi = \int_0^x (\rho \mu u)_\delta r^{2\epsilon} ds \quad (1.5)$$

$$\eta(x, y) = \frac{u_\delta r^\epsilon}{\sqrt{2\xi}} \int_0^y \rho dy \quad (1.6)$$

where  $\xi$  and  $\eta$  are the transformed coordinates,  $u$  is the velocity,  $r$  is the radial coordinate,  $s$  is the arc length along the surface,  $\delta$  represents conditions taken at the boundary layer edge, and  $\epsilon$  is a factor that is equal to 1 for axisymmetric flow or 0 for two-dimensional flow. This transformation has the property that the transformed equations remain parabolic and thus at the stagnation point the transformed equations can be reduced to a set of ordinary differential equations. Wall catalycity was modeled by way of a specified catalytic probability for a given reaction set. This method has been adopted for the present work as it represents a good intermediate between using a fixed wall composition and implementing a true finite rate wall chemistry model. The boundary layer code was coupled to a code

for the bulk flow using the Euler equations and compared to full Navier-Stokes simulations for various benchmark cases. It was also used in a standalone manner to exclusively study boundary layer behavior. In both uses, the boundary layer code yielded results that were in agreement with the Navier-Stokes simulations and previously published results.

Kolesnikov's 2003 work [28] examining the behavior of the 100 kW IPG-4 plasmatron at the Institute for Problems in Mechanics took an approach similar to Barbante's with splitting the flow into separate problems. Specifically, the flow in the torch was separated into 3 regimes: 1) a magnetohydrodynamic simulation of the induction region in thermochemical equilibrium; 2) an axisymmetric simulation of the plasma jet, also in thermochemical equilibrium; and 3) the stagnation point boundary layer with finite thickness, modeled using a one-dimensional similarity solution. The boundary layer was assumed to be in thermal equilibrium (thus using one temperature) and chemical nonequilibrium. The work focused on a Martian atmospheric entry and utilized a 5 species CO<sub>2</sub> mixture using Park's reaction rates. Owing to the combination of the simulations, the composition at the boundary layer edge was taken from the axisymmetric jet simulation and as such was in thermochemical equilibrium. Effective catalytic recombination probabilities were determined for oxygen on a silicon-based surface based on the approach used by Marschall. While approach of splitting the CFD problem into different flow regimes is valid, modern computing resources allow for the more direct approach used in the present work wherein the torch is modeled in one simulation from the jet exit downstream, including appropriate resolution of the boundary layer on the test sample surface.

In his doctoral dissertation [29], Magin outlined the framework for the MUTATION library that would serve as the replacement to PEGASE. This improved upon the formulations used in PEGASE by implementing algorithms for the calculation of transportation properties that were more accurate and less computationally expensive. In addition, Magin developed a model for ICP torches wherein the induction region and the bulk flow of the plasma jet were addressed in the same simulation by a solver that coupled the electromagnetic and

fluid dynamic behavior of the flow. Owing to the full consideration of inductive heating, the temperature field within the induction region was computed based on the electromagnetic field being generated. Simulations were performed for air and CO<sub>2</sub> plasmas studying the Von Karman Institute's Minitorch and Plasmatron facilities assuming LTE throughout the plasma jet. Magin's work went on to implement a method for Local Heat Transfer Simulation (LHTS) wherein non-dimensional parameters are used to relate actual flight conditions to those achievable in an ICP facility, building on the works of Kolesnikov and Degrez. Noting that the fluid dynamic behavior of the jet is almost entirely dependent on inlet mass flow, these parameters were kept constant at the boundary layer edge independent of other quantities, allowing for duplication of flight conditions within the boundary layer. Using this methodology, simulations modeling full chemical nonequilibrium were performed to assess heat flux on a quartz and copper calorimeters in order to build a heat flux abacus relating wall temperature and recombination probability to heat transfer on a surface. The result was in agreement with experimental data but no data regarding the chemical composition of the boundary layer was provided.

In his 2006 paper, Rini presented a model for LTE elemental demixing in ICP torches [30]. Elemental demixing allows for departures from the standard elemental mass fractions as a result of diffusion processes. Simulations were performed using an air mixture for the induction region of the VKI Plasmatron with 3 chemical regimes: LTE with constant elemental fractions, LTE with variable elemental fractions, and chemical nonequilibrium. Thermal equilibrium was assumed owing to the relatively high pressures (that is, relative to a true high altitude reentry condition) with an ICP torch, although this assumption would not apply extending this model to a reentry flow. An extension of this work to reentry modeling can be found in [31]. Elemental fractions of oxygen were found to differ between the nonequilibrium and variable elemental fraction flows, specifically towards the walls of the quartz tube, however there was not a great effect on the temperature field. Lastly, it was found that with increasing pressure (and thus faster reaction rates) the nonequilib-

rium model approaches the solution of the LTE variable elemental fraction model, which is supported by Rini's previous work [32]. The present work does not consider the induction region of the torch, but owing to the similar operating pressures, it can be assumed that a nonequilibrium approach will suffice in place of a model that considers elemental demixing.

Fletcher, Thömel, and Marschall's 2009 paper [33] presented an analysis of the UVM ICP facility utilizing the boundary layer code developed by Barbante. The code is formulated such that it is equally adaptable to modeling reentry or ground test facility flows and thus no modification was required to study the ICP boundary layer. Duplication of conditions was achieved by matching enthalpy, pressure, and velocity gradient at the boundary layer edge. The first two quantities are functions of the flow, however the velocity gradient can be calculated based on the test article radius, thus indirectly specifying the sample geometry. Utilizing a 5 species air mixture in chemical nonequilibrium and thermal equilibrium, the effects of wall catalycity, pressure, and sample radius on species and temperature gradients were studied. It was found that increased pressure significantly thinned the boundary layer and it was suggested that for increased pressures, a larger-radius sample should be used to counteract this thinning. In studies of catalycity, oxygen and nitrogen recombination was assumed to take place at the wall in the absence of competition from the formation of nitric oxide (NO) although the authors note that this mechanism is possible. Temperature-driven formation of NO was found to occur in the boundary layer, as would be expected for the temperatures encountered in this region. The cases studied represent a significant step forward in the study of the ICP boundary layer, although direct comparisons between numerical and experimental results were not provided. However, a series of future steps was presented for a more detailed study of nitrogen plasma and some of these have been performed experimentally and are considered from a numerical perspective in this dissertation

A 2011 technical report from Chazot, Schwartzentruber, Lani, Villedieu, and Barbante [34] presented a series of numerical efforts towards the study of ICP facilities utilizing various codes, specifically US3D from the University of Minnesota [35], the VKI LTE code, VKI's

CooLFLUID platform [36], and VKI’s Cosmic code [37].

US3D was originally developed for hypersonic flows and this work represented an improvement to it by modifying it to be suitable for nonequilibrium low speed flow simulation. Results from it were compared with results from the VKI LTE and found to be in good agreement. Importantly, full 3D simulations were performed and compared to axisymmetric simulations. The stagnation line and boundary layer profiles for the two were found to be virtually indistinguishable, providing further support for the use of an axisymmetric model for ICP simulations.

CooLFLUID is a large platform designed for the simulation of fluid flow in various regimes. Its libraries for modeling reentry and plasma flows were implemented by Lani as part of his Ph.D. dissertation. The simulations performed with CooLFLUID included coupling of the Navier-Stokes equations with the electromagnetic field equations such that the induction region of the ICP torch was fully modeled in addition to the plasma jet and test article geometry. A two temperature model for thermal nonequilibrium was included, as well as capability for full chemical nonequilibrium. This configuration was used to study the behavior of a test probe composed of two TPS materials with different catalytic behavior. Intuitively, the region with higher catalycity was found to have a slightly higher wall temperature and significantly higher heat flux. Although conditions representing an actual test case from the Plasmatron facility were used, no comparison to experimental results was presented.

The VKI Cosmic code was used to simulate the same case as the above example with CooLFLUID with a 5 species air mixture and an assumption of thermal equilibrium. Only nitrogen and oxygen recombination were considered at the wall, with equal recombination probabilities for both species. Two sets of simulations were performed with different assumed values of the catalytic probability for the low catalycity material. The results showed a noticeable difference in surface temperature between these cases for the low catalycity material. Experimental data was compared to these results and was shown to be in qualitatively

good agreement, however the simulations significantly under-predicted surface temperature for the surface with low catalycity.

In her Ph.D. dissertation, Anna [38] used the LEMANS code [39] to investigate the behavior of a nitrogen plasma in the UVM ICP facility. The simulations used an axisymmetric configuration and only considered the plasma flow from the outlet of the quartz tube with a 2 species nitrogen mixture. Simulations were performed comparing thermal equilibrium and non-equilibrium and the results suggested that thermal nonequilibrium should be considered in simulations of this type, although this finding contradicts many prior studies. A comparison was performed between a finite rate surface chemistry model and a simpler, kinetics-based binary recombination model. No difference was found to exist between these models for the simplified mixture, though it was noted that this may not hold true for more complex mixtures. Results were compared to experimental data obtained in the UVM ICP facility and generally showed good agreement. To the author's best knowledge, this represents the first direct comparison between CFD results and data from this facility. This dissertation significantly expands upon this for more complex mixtures.

## 1.2 Inductively coupled plasma torch facility

The plasma diagnostics lab at the University of Vermont is built around a 30 kW ICP Torch. Figure 1.2 shows a schematic representation of the power supply, the ICP torch and its associated cooling equipment, and the gas supply to the test chamber. The torch itself is comprised of three main systems: the radio frequency (RF) power supply, the injector block assembly, and the test chamber. The power supply can generate up to 30 kW at frequencies from 2.5 to 4 MHz. The plasma is generated within a quartz tube connected to the injector block. Quartz is used because of its properties as an electrical insulator and its durability at high temperature. Surrounding the quartz tube is a water-cooled copper coil through which current is run from the power supply, inducing an RF magnetic field within the quartz tube which creates the plasma through inductive heating. Gas flows are metered

by mass flow controllers and a vacuum pump is used to regulate the static pressure in the test chamber. A table of the ICP Torch Facility operating parameters is given in Table B.1.

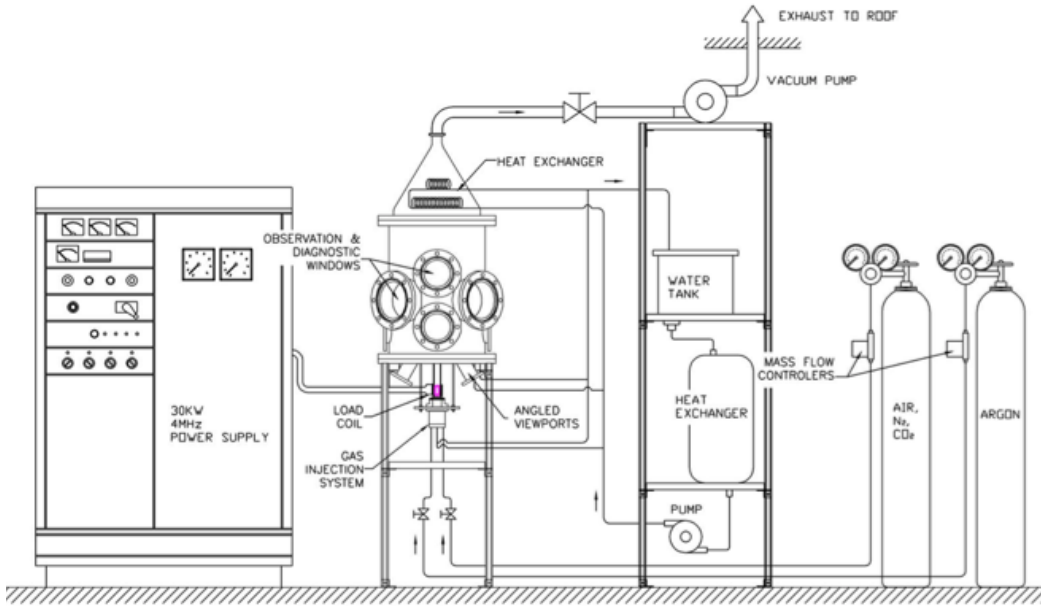


Figure 1.2: Schematic of full ICP torch facility including power supply and gas supply [2].

---

Inductive heater power [kW]	30
Enthalpy range [ $\text{MJ kg}^{-1}$ ]	10 - 40 (for air)
Mach range	< 0.3 to 1
Stagnation point heat flux [ $\text{W cm}^{-2}$ ]	10-150
Stagnation pressure [atm]	0.05 - 1.0
Plasma jet diameter [mm]	36
Test gas	air, Ar, N <sub>2</sub> , O <sub>2</sub> , CO <sub>2</sub> , variable mixture fractions

---

Table 1.1: Plasma torch operating parameters

Test sample surface temperature is measured with a two-color pyrometer that observes the sample surface directly through an angled viewport on the bottom flange of the test

chamber. A two-color pyrometer is used for its ability to measure surface temperature without requiring knowledge of the material surface emissivity. By calibrating both pyrometer channels, the device can also provide an emissivity value for the detection wavelength. Heat flux measurements are taken with either a slug calorimeter or a gardon gage before samples are placed in the plasma flow. Temperature measurements for the slug calorimeter are obtained from a thermocouple attached to the back of the copper slug. Measured heat flux values from the facility have been reported elsewhere [2]. Test chamber static pressure measurements are obtained from a port on the chamber.

### 1.3 Computing resources

Much of the work within this dissertation was performed using the Vermont Advanced Computing Core (VACC), a high-performance computing facility at the University of Vermont. The facility is comprised of various types of nodes but the present work utilized the facility's Infiniband-connected 36 dual-processor 6-core IBM dx360m3 nodes running Redhat Enterprise Linux 5. GNU Fortran and C/C++ compilers were used with MVAPICH2 and OpenMPI protocols for parallel computing. The external library HYPRE 2.9.0b was used for its package of linear solvers.

NASA's Pleiades supercomputing cluster was also used for computations in this dissertation. At the time of this writing, Pleiades is comprised of 11,176 Infiniband-connected nodes utilizing Intel Xeon Westmere, Sandy Bridge, and Ivy bridge processors and 184,800 CPU cores. The operating system is SUSE Linux on a Lustre filesystem. GNU Fortran and C/C++ compilers were used with MVAPICH2 protocols and the same external libraries were used for computations as on the VACC.

## 1.4 Objective and scope of this dissertation

***Chapter 2.*** A thorough description of the flow solver is provided with discussion of the numerical schemes used, boundary conditions implemented for scalar quantities (namely, chemical species and temperature), schemes developed to stabilize the solver in the presence of steep gradients, methods used for the implementation of finite rate chemistry, and an overview of the parallelization of the code as a whole. In addition, a detailed description of high temperature thermodynamic and transport properties is presented.

***Chapter 3.*** Details are provided regarding the practical implementation of the methods outlined in Chapter 2. Discussion of standard computational considerations such as Reynolds number of the plasma jet, grid independence, and parallel scaling is provided. Boundary and initial conditions are presented in addition to a detailed look at the gas mixtures and chemical reaction sets used in this work.

***Chapter 4.*** Results from the simulations introduced in Chapter 3 are presented. Simulations were performed for argon-buffered oxygen, pure nitrogen, and air plasmas. Numerical results are compared to experimental results for temperature and species composition in the boundary layer about a test article in the UVM ICP facility. A study is presented examining the nonequilibrium behavior of nitrogen on the composition and temperature within the plasma jet. In addition, a code-to-code validation exercise is performed and results are presented for a test case modeling the UVM ICP facility.

***Chapter 5.*** An overview is provided summarizing the key results presented in this dissertation and contributions from this work. Finally, recommendations for future work are suggested which build upon the framework developed in this dissertation.

## Chapter 2

# Flow solver, high temperature gas properties, and chemistry

### 2.1 Navier-Stokes flow solver

The core of the present work is the NGA/ARTS (Next Generation ARTS / Advanced Reactive Turbulent Simulator) CFD code, an arbitrarily high-order flow solver for the variable density, incompressible Navier-Stokes equations. It was originally developed for the study of chemically reacting, turbulent flows for combustion applications. It is able to simulate three-dimensional flows with or without walls in cartesian and cylindrical coordinate systems using uniform or non-uniform meshes. Its treatment of the governing equations (seen below in 2.1a, 2.1b, 2.1c) allows it to discretely conserve mass, momentum, and kinetic energy in a periodic domain. In a bounded domain, the boundary conditions enforce conservation of these quantities. It uses a staggered grid arrangement wherein all scalar quantities (pressure, density, transported scalars) are stored at the cell centers and components of velocity are stored at the cell faces. A schematic of this is seen in figure 2.1. This arrangement improves convergence, stabilizes the solution for pressure (which is coupled to the velocity field), and reduces dissipative errors [3].

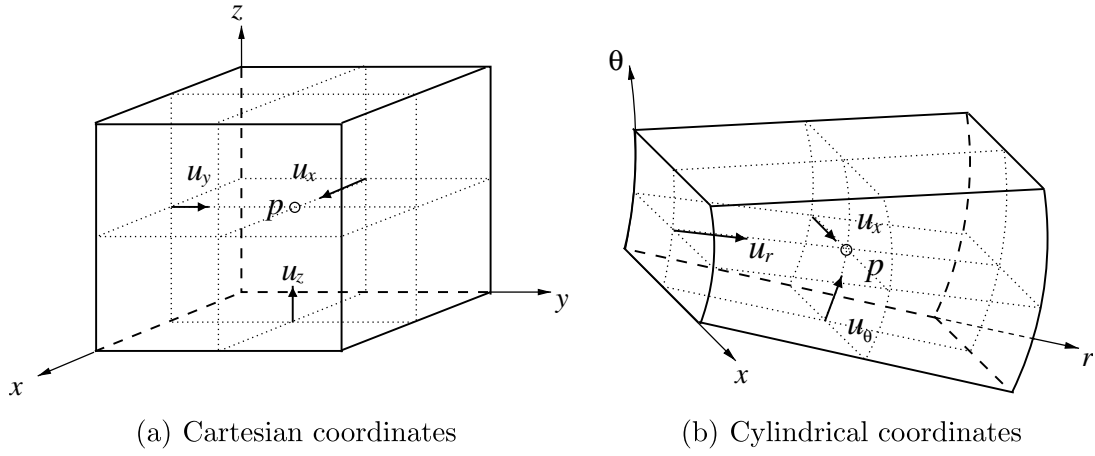


Figure 2.1: Schematic of staggered grid with vector quantities at cell faces and scalars at cell centers. [3]

### 2.1.1 Governing equations

The variable density, incompressible Navier-Stokes equations are given in equations 2.1a and 2.1b. Additionally, a scalar transport equation is solved and is seen in equation 2.1c.

$$\frac{\partial \rho}{\partial t} + \nabla \cdot \rho \mathbf{u} = 0 \quad (2.1a)$$

Equation 2.1a is the conservation of mass, where  $\rho$  is the density and  $\mathbf{u}$  is the velocity vector,  $\mathbf{u} = (u_1, u_2, u_3)$ , where the coordinate directions correspond to either  $(x, y, z)$  or  $(x, r, \theta)$  depending on the coordinate system being used. The present work utilizes axisymmetric cylindrical coordinates and, as such, that is what will be referenced from here onward.

$$\frac{\partial \rho \mathbf{u}}{\partial t} + \nabla \cdot (\rho \mathbf{u} \otimes \mathbf{u}) = -\nabla p \cdot \mathbb{I} + \nabla \cdot \left( \mu(\nabla \mathbf{u} + \nabla^T \mathbf{u}) - \frac{2}{3}\mu \nabla \cdot \mathbf{u} \mathbb{I} \right) \quad (2.1b)$$

Equation 2.1b is the conservation of momentum, where  $p$  is the pressure and  $\mu$  is the dynamic viscosity, and  $\mathbb{I}$  is the identity matrix. The enclosed term on the right hand side represents the deviatoric stress tensor.

$$\frac{\partial \rho Z}{\partial t} + \nabla \cdot (\rho \mathbf{u} Z) = \nabla \cdot (\rho \alpha_Z \nabla Z) + \dot{Q}_Z \quad (2.1c)$$

Equation 2.1c is the scalar transport equation where  $Z$  is any transported scalar,  $D_Z$  is the diffusivity of the scalar, and  $\dot{Q}_Z$  is the source term for scalar species due to chemical reactions. The latter term is of central importance to this work and its calculation will be discussed later.

Within NGA, the coordinates corresponding to the physical domain are mapped with uniform spacing into the computational domain. The coordinates of this domain are given by  $\zeta = (\zeta_1, \zeta_2, \zeta_3)$  where the subscripts correspond to the respective physical coordinates. The Jacobian used to scale coordinates between the physical and computational domains is written as:

$$h_i = \frac{dx_i}{d\zeta_i}, \quad J = h_1 h_2 h_3 \quad (2.2)$$

The solver in NGA only accounts for the main diagonal of the matrix that results from this equation, a condition which necessitates that all grids must be purely cartesian.

### Operators for discretization of convective terms

NGA achieves an arbitrarily high order of accuracy by using discrete interpolation and differentiation operators for the convective terms of the Navier-Stokes equations. To do this, an interpolation weight is defined as

$$\sum_{l=1}^{n/2} (2l - 1)^{2(l-1)} \alpha_l = \delta_{il} \quad (2.3)$$

where  $n$  is the order of accuracy sought,  $\alpha_l$  is the interpolation weight, and  $\delta_{il}$  is the Kronecker delta. From this, both interpolation (2.4) and differentiation (2.5) operators are calculated as:

$$\bar{\phi}^{nth\zeta_i} = \sum_{l=1}^{n/2} \alpha_l \bar{\phi}^{2(l-1)\zeta_i} \quad (2.4)$$

$$\frac{\delta_{nth}\phi}{\delta_{nth}\zeta_i} = \sum_{l=1}^{n/2} \alpha_l \frac{\delta_{2l-1}\phi}{\delta_{2l-1}\xi_i} \quad (2.5)$$

## Operators for discretization of viscous terms

Owing to the dissipative and inherently more stable nature of the viscous terms of the Navier-Stokes equations, a simpler treatment for discretization operators is applied to them. The interpolation (2.6) and differentiation (2.7) operators are constructed from an  $(n - 1)^{\text{th}}$  order Lagrange polynomial and its derivative, respectively.

$$\bar{\phi}^{n^{\text{th}}\zeta_i} = P(x) \quad (2.6)$$

$$\frac{\delta_{n^{\text{th}}}\phi}{\delta_{n^{\text{th}}}x_i} = P'(x) \quad (2.7)$$

As seen in equation 2.7, these operators are applied directly in the physical space, which separates them from their convective counterparts.

## Temporal integration

The Navier-Stokes equations are integrated in time using a variation on the second-order Crank-Nicholson method developed by Pierce [40]. Instead of integrating all quantities at the same points in time, the scalar field, density field, and momentum field are integrated separately and in the order listed. Following the advancement of these quantities, a Poisson equation for pressure is solved using a multi-grid solver from the HYPRE library [41].

NGA computes an implicit correction for the scalar and momentum equations in order to reduce the considerable time step limitations encountered when using cylindrical coordinates. This correction introduces the need to solve a poly-diagonal system for each velocity component and in each implicitly-treated direction. In the case of variable density, however, Desjardins [3] notes that this methodology does not discretely conserve kinetic energy.

### 2.1.2 CFL condition

The Courant-Friedrichs-Lowy (CFL) condition is a metric for the stability of explicit or, as is the case for temporal integration in NGA, semi-implicit integration of partial differential

equations. It is expressed in the form of  $C$ , the Courant number:

$$C = \Delta t \sum_{i=1}^3 \frac{u_i}{\Delta x_i} \quad (2.8)$$

It is effectively a metric quantifying the propagation of information from one point in a grid to an adjacent grid point. In order for an integration to maintain stability, the Courant number must not be exceeded based on the right hand side of equation 2.8. In practice, this stipulates that increasing grid resolution leads to a more restrictive time step for the same Courant number.

### 2.1.3 WENO scheme for scalar transport

A third-order Weighted Essentially Non-Oscillatory scheme (WENO-3) was selected for the discretization of the scalar transport equation. Typically, WENO schemes are chosen for applications where strong discontinuities exist, such as shocks. They also have the desired property of conserving scalar boundedness in cylindrical coordinates. This is particularly important for the flows treated in this work where the boundedness of the transported scalars is directly linked to the conservation of mass in the flow.

WENO schemes involve the computation of coefficients for different stencils such that the smoothest stencil is always used. Only the  $x$ -direction will be considered, but application in other directions is identical. First, centrally-differenced operators are computed:

$$cd_{x^+} = \frac{x_{m,i} - x_i}{x_{m,i} - x_{m,i-1}} \quad (2.9)$$

$$cd_{x^-} = \frac{x_i - x_{m,i}}{x_{m,i} - x_{m,i-1}} \quad (2.10)$$

where  $x^+$  indicates use for flow in the  $+i$  direction and  $x^-$  indicates use for flow in the  $-i$  direction. These operators are used to quantify the spacing between the cell mid-points (subscript  $m$ ) and the cell faces. Next, similar operators for upwinding are computed:

$$up_{x^+} = \frac{x_{m,i} - x_i}{x_{m,i-1} - x_{m,i-2}} \quad (2.11)$$

$$up_{x^-} = \frac{x_{m,i+1} - x_i}{x_{m,i+1} - x_{m,i}} \quad (2.12)$$

These operators are functions of the grid spacing only and are computed once at the beginning of a simulation. The WENO coefficients, however, must be computed at every step because they are functions of the scalar field. Values for the weighting of the coefficients are computed as:

$$r_{x^+,i} = \frac{\epsilon (Z_{i-1} - Z_{i-2})^2}{\epsilon + ((Z_i - Z_{i-1}) \Delta x_{m,i-1})^2} \quad (2.13)$$

$$r_{x^-,i} = \frac{\epsilon (Z_{i+1} - Z_{i-})^2}{\epsilon + ((Z_i - Z_{i-1}) \Delta x_{m,i-1})^2} \quad (2.14)$$

$$\alpha_i = \frac{1}{1 + 2r_i^2} \quad (2.15)$$

where  $\epsilon$  is a small constant, typically  $10^{-6}$ . Finally, the WENO-3 coefficients are calculated:

$$\omega_{x^+,i} = (1 - \alpha_i) cd_{x^+} + \alpha_i up_{x^+} \quad (2.16)$$

$$\omega_{x^-,i} = (1 - \alpha_i) cd_{x^-} + \alpha_i up_{x^-} \quad (2.17)$$

The coefficients  $\omega_x$  are applied in the calculation of the scalar residual. Specifically, they are used to discretize the convective term  $\rho u Z$ . This takes the form of:

$$\rho_i u_i \sum_{i=2}^i \omega_{x^+,i} Z \quad (2.18)$$

or, for flow in the  $-i$  direction:

$$\rho_i u_i \sum_{i=1}^{i+1} \omega_{x^-,i} Z \quad (2.19)$$

More detail on WENO schemes can be found in the work of Liu and Osher [42] and Jiang [43].

#### 2.1.4 Scalar boundary conditions

For the case of a bounded, non-periodic flow, it is necessary to define physical boundary conditions for the scalar transport equation (2.1c). NGA previously had simple Neumann boundary conditions for scalars, imposed as:

$$\left( \frac{dZ}{d\vec{n}} \right)_w = 0 \quad (2.20)$$

In the case of temperature, this represents an adiabatic condition and for a chemical species, this would be analogous to a frozen boundary layer in which no gas phase or surface reactions are taking place. For the flows covered in the present study, this is not a physical nor useful boundary condition. New boundary conditions have been introduced for both temperature and chemical species that are more physically meaningful.

In the case of temperature, a Dirichlet condition has been implemented for an isothermal wall. Owing to the discretization of the finite volume scheme, specifically the staggering of scalar and vector quantities (figure 2.1), the value of a scalar in the first fluid cell,  $Z_{i_m-1}$  (in the case of a right hand boundary) must be interpolated from values at the ghost nodes. The interpolation allows this method to maintain  $\mathcal{O}^2$  accuracy at the boundary. This is expressed as:

$$Z_w = \frac{Z_{um} - Z_{i_m-1}}{x_{i_m} - x_{i_m-1}} (x_{i_m} - x_{i_m-1}) - Z_{i_m-1} \quad (2.21)$$

which can be arranged to yield the value at the first fluid cell:

$$Z_{i_m-1} = 2Z_w - Z_{i_m} \quad (2.22)$$

In order for this formulation to be reasonably stable, it must be enforced implicitly during the calculation of the the scalar residual. For the WENO-3 scheme in one dimension, the residual calculation takes the form:

$$a\mathbf{Z}_{i-2}^{n+1} + b\mathbf{Z}_{i-1}^{n+1} + c\mathbf{Z}_i^{n+1} + d\mathbf{Z}_{i+1}^{n+1} + e\mathbf{Z}_{i+2}^{n+1} = \mathbf{R}_x \quad (2.23)$$

where the subscripts represent physical space and the superscripts indicate time. The resultant system is in the form of a pentadiagonal matrix although due to the upwinding inherent in the WENO-3 scheme, the term for either  $(i-2)$  or  $(i+2)$  will always be zero,

depending on flow direction. In matrix form, this is written:

$$\begin{bmatrix} c_{i=1} & d_{i=1} & e_{i=1} & 0 & \cdots & 0 & 0 \\ b_{i=2} & c_{i=2} & d_{i=2} & e_{i=2} & 0 & \cdots & 0 \\ & & & \ddots & \ddots & & \\ \vdots & a_i & b_i & c_i & d_i & e_i & \vdots \\ & & & \ddots & \ddots & & \\ 0 & \cdots & 0 & a_{i=n_x-1} & b_{i=n_x-1} & c_{i=n_x-1} & d_{i=n_x-1} \\ 0 & 0 & \cdots & 0 & a_{i=n_x} & b_{i=n_x} & c_{i=n_x} \end{bmatrix} \begin{Bmatrix} Z_{i=1}^{n+1} \\ Z_{i=2}^{n+1} \\ \vdots \\ Z_i^{n+1} \\ \vdots \\ Z_{n_x-1}^{n+1} \\ Z_{n_x}^{n+1} \end{Bmatrix} = \begin{Bmatrix} R_{i=1} \\ R_{i=2} \\ \vdots \\ R_i \\ \vdots \\ R_{i=n_x-1} \\ R_{i=n_x} \end{Bmatrix} \quad (2.24)$$

Unlike the Dirichlet condition, a Neumann boundary condition for the flux of a scalar at the wall,  $\nabla Z$ , is less involved. No interpolation is required because the derivative term is located at the cell face rather than the center, thus  $\mathcal{O}^2$  accuracy is retained. The discretized form of the flux at the boundary is given by:

$$\frac{Z_{i_m} - Z_{i_m-1}}{x_{i_m} - x_{i_m-1}} = \vec{J}_{i,wall} \quad (2.25)$$

where  $\vec{J}_{i,wall}$  is the flux specified at the wall. This can either be specified directly or computed using the method outlined in section 2.1.5. Owing to the absence of an interpolation, the left hand side of equation 2.25 is the exact value of the flux at the boundary. This results in a formulation wherein the computed diffusive flux at a wall is simply replaced by  $\vec{J}_{i,wall}$  during the calculation of the residual. As opposed to the zero flux condition where  $Z_{i_m} = Z_{i_m-1}$ , this formulation allows the flux of a scalar at the wall to alter the scalar gradient within the boundary layer.

### 2.1.5 Catalytic wall

Developing an accurate model for the surface of a TPS material required that boundary conditions addressing the catalytic behavior of the wall be implemented into NGA. In addition to the gas phase reactions taking place in the boundary layer, both in a reentry flow and a ground test facility, the catalytic effects of a surface can have a significant impact

on the heat flux experienced at the wall owing to highly exothermic recombination reactions. The catalytic behavior of a wall is typically categorized into different types:

- **supercatalytic:** all dissociated species recombine to their free stream values;
- **fully-catalytic:** surface reactions occur with an infinite rate;
- **partially catalytic:** used when catalytic properties of the surface material are known for all recombining species, includes finite reaction rates;
- **non-catalytic:** no surface recombination reactions occur;

Supercatalytic behavior has a somewhat misleading definition if applied to a ground test facility. In this situation, the free stream is typically dissociated to some degree and returning to this composition at the wall actually implies that the flow is frozen. Of course, for a reentry vehicle, this is not the case because ahead of the shock the ambient atmosphere is at a low temperature and there is no dissociation, so the post-shock conditions will be drastically different and recombination to the free stream composition will result in significant heat released from reactions. The fully catalytic case is a more realistic upper limit for the behavior of a ground test facility and would likely yield the highest heat flux. The partially-catalytic assumption is the most realistic and, in a design situation, requires specific knowledge of a given material's catalytic properties. A non-catalytic wall is the extreme which would experience the least heat flux and result in a frozen boundary layer. For an ICP facility, supercatalytic and non-catalytic boundary conditions are effectively one in the same.

Modeling wall catalycity is an intermediate approach to the problem of the chemical composition at the wall. The simplest way to approach wall chemistry is to specify chemical composition at the wall with a Dirichlet boundary condition, whereas the ideal, physics-based wall chemistry model would address different modes of surface reaction (Eley-Rideal, Langmuir-Hinshelwood, sublimation etc) using finite rate kinetics for all reactions taking place. Such models exist [19] but are beyond the scope of this work.

It is assumed that for plasma flows in ground test facilities the wall maintains a no-slip condition for velocity, although this does not necessarily hold true for reentry flows at high altitude and very low pressure. With a no slip condition, the convective flux at the wall is identically zero and diffusion is the mechanism for mass transfer between the gas phase and wall. This assumption is valid for a non-ablating surface; with an ablative material, mass can be introduced into the gas phase through other mechanisms. Thus, for a stationary surface at steady state, a boundary condition exists such that the diffusion flux of a species at the wall is balanced by the rate of production or destruction of that species at the wall:

$$\vec{J} \cdot \vec{n}_{wall} = \dot{\omega}_{i,wall} \quad (2.26)$$

This is expanded by defining a catalytic probability,  $\gamma$ , which is the ratio of atoms of species  $i$  that impinge on the wall to the total flux of species  $i$  at the wall:

$$\gamma_i = \frac{\Gamma_{i,recomb}}{\Gamma_{i,total}} \quad (2.27)$$

Because the production of a molecular species at the wall is balanced by the diffusion flux of its constituent atomic species, equation 2.26 can be re-written as:

$$\dot{\omega}_{i,wall} = \gamma_i m_i \Gamma_{i,total} \quad (2.28)$$

Following the formulation of Barbante [27], the diffusion flux  $\Gamma_i$  is developed from kinetic theory. The particles at the wall are assumed to adhere to a Maxwellian velocity distribution with the addition of a Chapman-Enskog perturbation. The perturbation term is necessary because the gas composition at the wall is not necessarily in LTE for that temperature and pressure. From this, the impingement flux for species  $i$  at the wall is:

$$\dot{\omega}_i = \frac{2\gamma_i}{2 - \gamma_i} m_i n_i \sqrt{\frac{k_B T_w}{2\pi m_i}} \quad (2.29)$$

where  $n_i$  is the species number density at the wall and  $k_B$  is the Boltzmann constant. The term  $m_i n_i$  is equivalent to the species density at the wall. In NGA this has been implemented as  $\rho y_i$ .

This approach is limited in that even for  $\gamma = 1$ , the wall composition does not necessarily fully reach an LTE state. If an LTE boundary condition were desired, it could easily be achieved by imposing the species composition at the wall in the form of a Dirichlet boundary condition.

Within NGA, this boundary condition has been implemented such that it replaces the term for the diffusive flux of a species,  $(\rho \alpha_Z \nabla Z)$ , in equation 2.1c at the first cell within a wall using the methods discussed in section 2.1.4.

### 2.1.6 Outlet buffer region

The formulation used within NGA to calculate outlet velocity necessitates that the first term in equation 2.1a,  $\frac{\partial \rho}{\partial t}$ , be zero. Physically, this is not always the case for a variable-density reacting flow within a bounded domain. The plasma flow features sharp density gradients, relatively high velocities, and stiff chemical source terms which result in a flow that 1) requires small time steps; and 2) features large temporal density gradients. Owing to the time step limitations, a window function was introduced to maintain stability by scaling the term  $\partial \rho$  smoothly towards zero near the outlet of the computational domain. Doing so is necessary only during the start-up of the jet: when the plasma jet reaches steady state, the temporal change in density at every cell approaches zero. The method presented in [44] was implemented in a more general form for an arbitrary domain and takes the form of a scaling function:

$$h(x) = \frac{1}{2} \left( \tanh \left( 2s \left[ \frac{x_m + L - \epsilon/2}{\epsilon} \right] \right) - \tanh \left( 2s \left[ \frac{x_m - L + \epsilon/2}{\epsilon} \right] \right) \right) \quad (2.30)$$

where  $s$  is the maximum slope of the function,  $L$  is the total length of the domain,  $\epsilon$  is the length of the buffer region, and  $x_m$  is the midpoint location of a cell where  $\rho$  and the temporal change in density,  $(\rho^k - \rho^{k-1})$ , are stored.

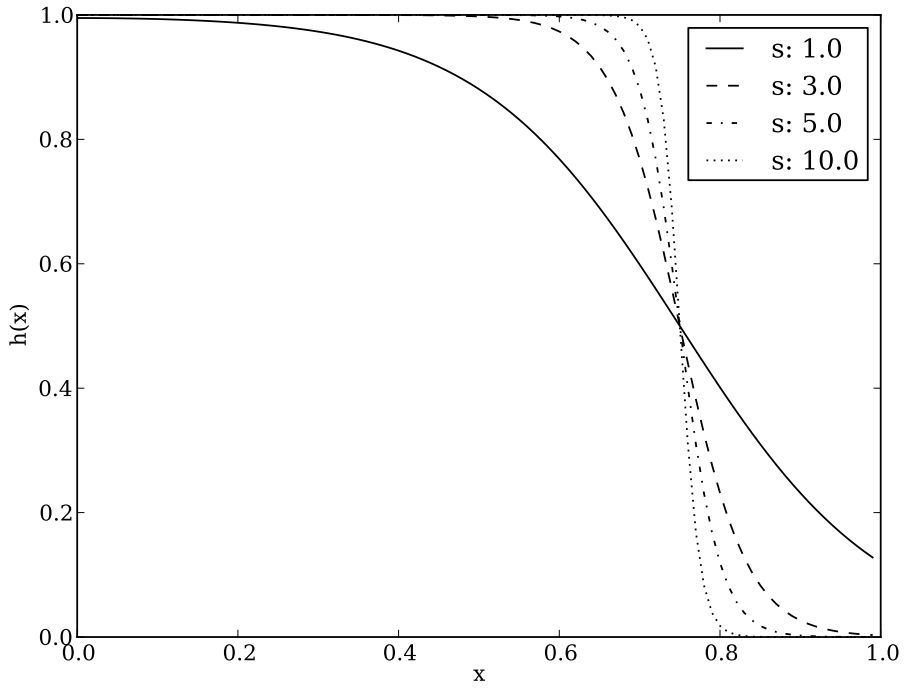


Figure 2.2: Window function (equation 2.30) used to scale computed change in density in outlet buffer region.

Figure 2.2 shows the window function computed with varying  $s$  values over a domain of length  $L = 1$  and a buffer region of width  $\epsilon = 0.5$ . It is seen that for values of  $s$  less than 3, the window function does not reach zero before the end of the domain owing to the choice of the buffer region length relative to the total domain size. Thus, it is apparent that these values must be selected carefully such that the density change is not being filtered in a region of interest and that it is forced to zero by the end of the domain.

### 2.1.7 Finite rate chemistry

The built-in finite rate chemistry module in NGA has been modified to allow the use of MUTATION++ (discussed in section 2.2) for thermodynamic and transport properties and

chemical production terms. The original purpose of the chemistry module in NGA was combustion modeling, in which complex gas mixtures are required to accurately simulate the chemical processes taking place. As an example, a combustion model of *n*-heptane requires a mixture with 41 species and 185 reactions which stands in stark contrast to the mixtures presented in section 3.5. Additionally, the previous chemistry implementation was cumbersome: it required the use of an external code to initialize the mixture and build look-up tables before starting a simulation. While this is not a bad practice (the use of look-up tables is common in combustion-oriented flow modeling) the framework had two significant shortcomings which rendered it unsuitable for plasma modeling and created the need for the MUTATION++ implementation: the temperature range was insufficient for plasma flow and the techniques used to calculate transport properties were only suitable for neutral species, preventing the use of mixtures with ions and electrons.

The relatively small temperature range covered by the previous model is a direct function of the needs of modeling combustion. The temperatures seen in a typical combusting hydrocarbon simulation are markedly lower than those of an inductively coupled plasma. The maximum valid temperature in the previous model was 5000 K, which is significantly lower than even the boundary layer edge temperature in a plasma. In addition, the calculation of transport properties relied on the use of Lennard-Jones potentials, an approach which is invalid for charged species. Plasmas created in an ICP torch typically have some degree of ionization and can feature temperatures at the ICP torch outlet on the order of 10,000 K or more.

The integration of differential equations resulting from chemistry source terms is performed using the DVODE package [45]. DVODE is designed to integrate an arbitrarily large set of stiff equations, making it ideal for the integration of chemical source terms in this setting. The system of equations for chemical source terms in NGA is seen in its most general form in equation 2.31 in:

$$f(t, y_i) = \frac{dZ}{dt} = \frac{dy_i}{dt} \quad (2.31)$$

where  $f(t, y_i)$  represents the resulting species mass fractions and temperature within a given cell. This array has the form of  $[1, \dots, N_{sp}, T]$  where  $N_{sp}$  is the total number of species in the mixture. The right hand side of equation 2.31 is computed as:

$$\dot{y}_i = \frac{\dot{\omega}_i}{\rho} \quad (2.32)$$

where  $\dot{\omega}_i$  is the rate of production for species  $i$  in  $\left[ \frac{kg}{m^3 \cdot s} \right]$  and  $\rho$  is the density in  $\left[ \frac{kg}{m^3} \right]$  within that cell. The determination of  $\dot{\omega}_i$  will be discussed in section 2.2.5. The dimensional production term,  $\dot{\omega}_i$ , is converted to a rate of change in mass fraction in order to adhere to the convention of transporting scalars in non-dimensional form.

The temperature rate of change for equation 2.31 is computed as a function of the mass fraction rate of change, species enthalpies, and the specific heat of the mixture at that grid point:

$$\phi = - \sum_{i=1}^{N_{sp}} h_i \dot{y}_i \quad (2.33)$$

$$\frac{dT}{dt} = \frac{\phi}{c_{p,mix}} \quad (2.34)$$

where  $\phi$  is a dummy variable introduced to keep the coded implementation of this equation set legible. A variation of this technique is seen in [46]. Using the computed right hand side terms from equations, 2.32 and 2.34, DVODE performs the integration per equation 2.31, resulting in updated species mass fractions and temperature. The source term transported by the scalar scheme is then computed as:

$$\dot{Q} = Z^k - Z^{k-1} \quad (2.35)$$

which is the difference between the old scalar value and the integrated value at the present time step. Then, the source term is scaled with the change in thermodynamic pressure between time steps:

$$\dot{Q} = \dot{Q} + \frac{P^k - P^{k-1}}{c_p} \quad (2.36a)$$

and put into a form suitable for use in equation 2.1c during the calculation of the scalar residual:

$$\dot{Q} = \dot{Q} + \rho \dot{Q} \quad (2.36b)$$

### 2.1.8 Parallel partitioning

NGA is fully parallelized and can be run with an arbitrary number of processors in all coordinate directions. Partitioning is necessary in order to efficiently distribute the computational workload among available processors. The process of partitioning breaks the computational domain into smaller regions, each of which are handled by an individual processor. Ideally, the computational regions handled by each processor should be similar in scale. When this is not the case, simulations can be slowed down by a processor that encompasses a larger computational domain than others.

The total number of processors used must obey:

$$n_{proc} = np_x \times np_y \times np_z$$

where  $n_{proc}$  is the total number of processors and  $np_x$ ,  $np_y$ , and  $np_z$  are the number of processors along the  $x$ ,  $y$ , and  $z$  directions respectively. The process is identical in cylindrical coordinates, with the partitions being considered to represent the  $x$ ,  $r$ , and  $\theta$  directions.

In order to visualize the partitioning process, a schematic of a basic computational domain in cartesian coordinates is seen in Figure 2.3. In this example,  $np_x = np_y = np_z = 2$  such that  $n_{proc} = 8$ . It is generally advisable to ensure that each partition is the same size and in this example the partitions are visualized as being identical although in practice this is sometimes not possible.

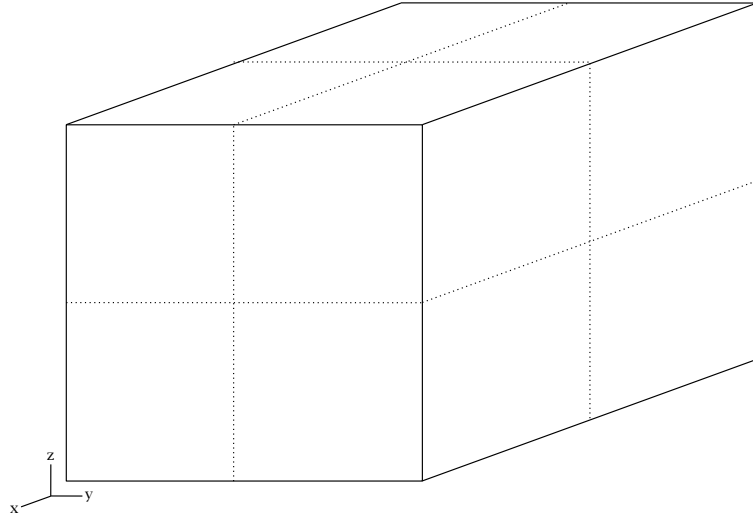


Figure 2.3: Diagram showing partitioning of processors along  $x$ ,  $y$ , and  $z$  directions for a computational domain with  $npx = npy = npz = 2$ . The solid lines represent the boundaries of the domain and regions within the dashed lines indicate the partitions created for each processor.

Partitioning of the domain is performed once at the start of the simulation and thus the load balancing is static. The process is based solely on the number of grid points in each direction within the computational domain, whose mapping is shown in equation 2.2 and has uniform spacing that is independent of physical mesh spacing. Owing to the uniform spacing in this domain, the partitions created are based on the number of grid points per processor and not physical dimensions. With non-uniform physical grid spacing, partitions containing regions of sharper gradients in the flow (thus, more grid points for a given area) occupy less physical space than partitions containing regions of less active flow. These more densely-gridded regions often require more time to resolve relative to those with less active

flow which causes an imbalance in computing time per partition.

In the interest of brevity, only the  $x$ -direction will be discussed here as the procedure is identical for all 3 coordinate directions. The algorithm for this is seen in algorithm 1. In the event that the domain is sized such that the partitions are not even, the algorithm attempts to evenly size as many of the partitions are possible. Ghost cells are necessary for the application of boundary conditions (both physical and between partitions) and are specified in the variable  $nover$ . The actual overlap between partitions ends up being twice the value of  $nover$ , such that no cells within the flow are treated solely as ghost cells.

```

for  $iproc = 1$  to  $npx$  do
     $q = \frac{nx}{npx}$ ,  $r = mod(nx, npx)$ ;
    if  $iproc \leq r$  then
         $nx_- = q + 1$ ;
         $imin_- = imin + (iproc - 1)(q + 1)$ ;
    else
         $nx_- = q$ ;
         $imin_- = imin + r(q + 1) + q(iproc - r - 1)$ ;
    end
     $nover = 2$ ;
     $nxo_- = nx_- + 2 \cdot nover$ ;
     $imax_- = imin_- + nx_- - 1$ ;
     $imino_- = imin_- - nover$ ;
     $imaxo_- = imax_- + nover$ ;
end
```

Algorithm 1: Algorithm for partitioning the computational domain across  $npx$  processors.

A trailing underscore denotes coordinates local to a given processor.

A visualization of the result of the partitioning algorithm appears in figure 2.4 for a one

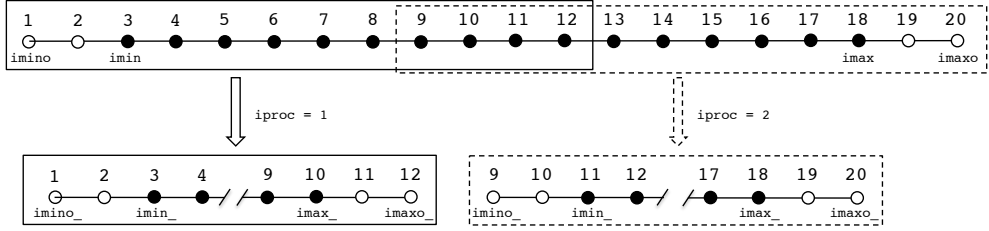


Figure 2.4: Parallel partitioning in NGA for a simple one dimensional domain with 2 processors. The filled circles represent nodes within the flow and the outlined circles represent the ghost nodes.

dimensional domain over two processors, with an ideally specified number of nodes such that the partitions are evenly sized. In this case, the actual number of user-specified nodes,  $nx$ , is 16 but with the addition of ghost cells the total number becomes 20. The number of fluid cells handled by each node is 8 and it is seen that there is no actual overlap in terms of cells that are considered fluid cells: if a cell is a fluid cell at the edge of one processor, it will be a ghost cell on the neighboring processor. This overlap results in 12 cells per processor even though there are only 20 actual cells and two processors. This process easily extends to all three coordinate directions, although the visualization becomes increasingly difficult.

## 2.2 High temperature gas properties

### 2.2.1 Overview

MUTATION++ (**M**ULTicomponent **T**ransport **A**nd **T**hermodynamic properties / chemistry for **I**ONized gases in C++) is the most recent iteration in a family of libraries developed at the von Karman Institute to compute high temperature gas properties for computational fluid dynamics applications [47] [29]. It can be used as either a standalone utility or as a library interfaced to a CFD code, the latter being the case in the present work.

### 2.2.2 Equation of state

In the context of aerothermodynamics, a plasma is characterized by its high temperature and low density which results in intermolecular forces that are negligible relative to the kinetic energy of the particles in the flow. These forces only become considerable at extremely high pressures or very low temperatures, neither of which occur in an ICP facility or a reentry flow. As such, for the purposes of selecting an equation of state, the plasma within the facility can be considered a perfect gas. We can write the equation of state for an ideal gas in terms of individual species molecular weights as:

$$\rho = \frac{p \sum_{i=1}^{N_{sp}} \mathcal{M}_i}{R_u T} \quad (2.37)$$

where  $\rho$  is the mixture density,  $p$  is the pressure,  $\mathcal{M}_i$  is the molar mass of species  $i$ ,  $R_u$  is the universal gas constant, and  $T$  is the temperature of the gas. Accordingly, we can also write the total density of the mixture in terms of the individual species densities:

$$\rho = \sum_{i=1}^{N_{sp}} \rho_i \quad (2.38)$$

It follows that the mass fraction of species  $i$  can be defined:

$$y_i = \frac{\rho_i}{\rho} \quad (2.39)$$

The conservation of mass stipulates that at any point in the mixture, the following relation must be obeyed:

$$\sum_{i=1}^{N_{sp}} y_i = 1 \quad (2.40)$$

Mass fraction is used in the formulation of the present work to track behavior of individual species owing to its simplicity, non-dimensional nature, and the ability to quickly ensure that conservation is maintained.

A similar quantity to mass fraction is the mole fraction of a species, defined as:

$$\chi_i = \frac{n_i}{n} \quad (2.41)$$

where  $n$  is the mixture number density with units  $[m^{-3}]$ . Mole fraction requires slightly more care in its use than mass fraction because as temperature increases and molecules dissociate, the total number of moles in a mixture increases, resulting in non-constant mole fractions for species that are unchanging in terms of mass.

### 2.2.3 Thermodynamic properties

Thermodynamic properties are computed in MUTATION++ using statistical thermodynamics, wherein the gas is viewed as a system of microscopic particles that exchange energy with one another. Unlike kinetic theory, discussed in section 2.2.4, statistical thermodynamics does not focus on the mechanisms of energy exchange, rather it deals only with the energy itself. The particles that comprise the gas are considered from a quantum mechanical perspective, in which their energy exists in discrete states. The distribution of energy across these states is described with a partition function,  $Q$ , which is a product of the translational, rotational, vibrational, and electronic contributions:

$$Q = Q_{tr}Q_{rot}Q_{vib}Q_e \quad (2.42)$$

This form of representing the energy distribution can then be applied to the calculation of thermodynamic properties for the gas. This view of the energy distribution is valid for

the low-density flows encountered in the present work; it is worth noting, however, that at higher densities, perturbations occur between energy levels as a consequence of the increased collision frequency and the present model is not sufficient for modeling these interactions. A thorough description of the foregoing overview is provided by Vincenti and Kruger [48].

## Energy

The mixture energy is given by the sum of the contributions from each species:

$$e = \sum_{i=1}^{N_{sp}} y_i(e_i + \Delta h_{F,i}) \quad (2.43)$$

where  $\Delta h_{F,i}$  is the standard enthalpy of formation of species  $i$ . The reference conditions for this value are  $p = 1$  atm and  $T = 298$  K. The enthalpy of formation for an element that exists as an atom at these conditions or any homogenous molecule is zero. Without this quantity, equation 2.43 represents the mixture energy in the absence of any change in composition or temperature of the mixture.

## Enthalpy

In keeping with the form established for the energy in equation 2.43, the enthalpy of the mixture is written as:

$$h = \sum_{i=1}^{N_{sp}} y_i(h_i + \Delta h_{F,i}) \quad (2.44)$$

This suffices for the mixture enthalpy but the individual species enthalpies require slightly more care in their calculation. In practice, the species enthalpies can be quickly computed using a polynomial [1] of the form:

$$h_i = \left( \sum_{n=1}^5 \frac{A_n T^{n-1}}{n} + \frac{A_6}{T} \right) R_u T \quad (2.45)$$

where the coefficients  $A_n$  have been calculated from experimental data. Individual  $A_n$  values vary depending on the temperature range in which an enthalpy is sought. This is necessary to achieve accuracy in the polynomial being fit to experimental data [1].

## Specific heat

Specific heat of the mixture is a property that requires particular consideration in the presence of finite rate chemical reactions. For a subsonic plasma flow, it is the only property that features a thermodynamic derivative as part of its calculation. This requirement results in the specific heat having two distinct possible values depending on the state of the mixture. The general equation for specific heat at constant pressure is given as:

$$c_p = \left( \frac{\partial h}{\partial T} \right)_p \quad (2.46)$$

However, this formulation obscures the details of the calculation. Taking the previous expression for enthalpy, equation 2.44, and combining it with 2.46, we find:

$$c_{p,eq} = \sum_{i=1}^{N_{sp}} \left[ \left( \frac{\partial y_i}{\partial T} \right)_p (h_i + \Delta h_{F,i}) + y_i \left( \frac{\partial h_i}{\partial T} \right)_p \right] \quad (2.47)$$

In the absence of chemical reactions, the term  $\left( \frac{\partial y_i}{\partial T} \right)_p$  becomes zero. Applying the definition from equation 2.46 we find an expression for the frozen specific heat:

$$c_{p,frozen} = \sum_{i=1}^{N_{sp}} y_i c_{p,i} \quad (2.48)$$

Figure 2.5 shows a comparison between the frozen and equilibrium specific heats for an oxygen mixture plotted with the corresponding equilibrium mass fractions. The dependence on the first term in equation 2.47 is readily apparent for the equilibrium specific heat in the range of approximately 2000-4000 K. The chemical reactions are most active in this range, evidenced by the change in composition, and thus the equilibrium specific heat experiences the largest changes. Through this region the frozen specific continues its slight increasing trend but does not vary substantially relative to the equilibrium value. It is seen that at temperatures outside of this range, i.e. in the absence of active dissociation or recombination, the equilibrium specific heat is effectively equal to the frozen value.

Owing to the significant differences between the two possible values of specific heat, it is necessary that the appropriate choice be made for a particular flow. In the present work

wherein the reacting plasma is modeled using a nonequilibrium approach, the frozen specific heat is used. This is necessary to ensure that there is not an erroneous heat source or sink, given that equation 2.34 already essentially addresses the rate of change of enthalpy, albeit with respect to time rather than temperature.

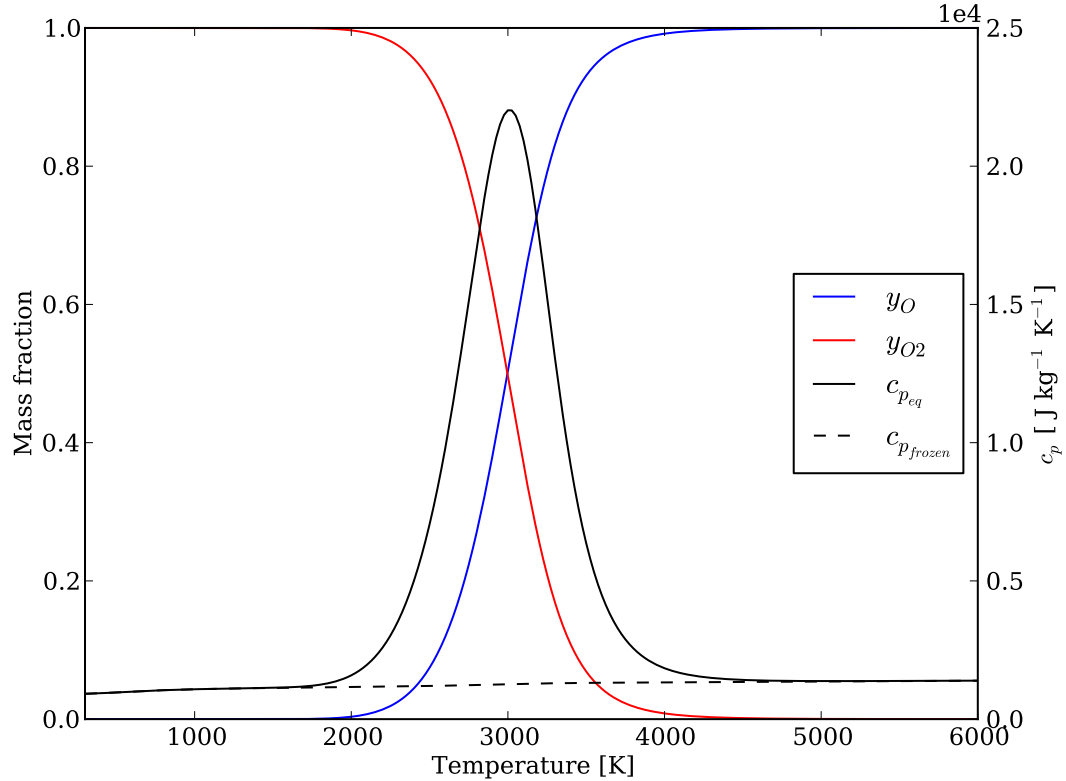


Figure 2.5: Equilibrium and frozen specific heats and species mass fractions of a binary oxygen mixture at 10 kPa.

#### 2.2.4 Transport properties

The calculation of transport properties in MUTATION++ is performed with a rigorous treatment of the underlying kinetic theory. This approach treats the gas from a molecular perspective and relates the particle speeds and collisions at this scale to observable macro-

scopic properties. A rigorous treatment of the calculation of transport properties is found in [29] and the following overview presents the aspects of this process most relevant to the present work.

## Viscosity

Previously, NGA used Wilke's method for the computation of viscosity. This implementation relied on tabulated data derived from Lennard-Jones potentials, which cannot be applied to ionized species, as discussed in section 2.1.7, and as such was an inappropriate model to use for modeling a plasma of arbitrary composition. MUTATION++ uses the Gupta-Yos mixture rule to compute viscosity. This mixture rule is an approximation based on the more intensive Chapman-Enskog formula that yields accurate results with a modest computational demand for weakly ionized gases [49] and thus is well-suited to the current modeling needs.

The main equation for the Gupta-Yos formulation is:

$$\mu = \frac{\sum_{i=1}^{N_{sp}} \chi_i / (A_i + a_{av})}{1 - a_{av} \sum_{i=1}^{N_{sp}} \chi_i / (A_i + a_{av})} \quad (2.49)$$

where  $\chi_i$  is a species mole fraction,  $A_i$  is a coefficient computed from species properties, and  $a_{av}$  is an average of the off-diagonal matrix elements from the Chapman-Enskog formula.  $a_{av}$  is written as:

$$a_{av} = \frac{\sum_{i,j=1}^{N_{sp}} \chi_i \chi_j \left( \frac{1}{A_i} - \frac{1}{A_j} \right)^2 a_{ij}}{\sum_{i,j=1}^{N_{sp}} \chi_i \chi_j \left( \frac{1}{A_i} - \frac{1}{A_j} \right)^2} \quad (2.50)$$

Finally, four remaining quantities must be defined:

$$A_i = \sum_{l=1}^{N_{sp}} \chi_l \frac{N_A}{M_i} \Delta_{il}^{(2)} \quad (2.51)$$

$$a_{ij} = \frac{N_a}{M_i + M_j} \left( 2\Delta_{ij}^{(1)} - \Delta_{ij}^{(2)} \right) \quad (2.52)$$

$$\Delta_{ij}^{(1)} = \frac{16}{5} (1.546(10^{-20})) \left[ \frac{2M_i M_j}{\pi R_u T (M_i + M_j)} \right]^{\frac{1}{2}} \pi \bar{\Omega}_{ij}^{(1,1)} \quad (2.53)$$

$$\Delta_{ij}^{(2)} = \frac{16}{5} (1.546(10^{-20})) \left[ \frac{2M_i M_j}{\pi R_u T (M_i + M_j)} \right]^{\frac{1}{2}} \pi \bar{\Omega}_{ij}^{(2,2)} \quad (2.54)$$

where  $M$  is the molecular weight of a species and  $N_A$  is Avogadro's number.  $\bar{\Omega}_{ij}^{(p,q)}$  are collision integrals which are taken from tabulated data.

Sutherland's formula was implemented as an intermediate step between the use of Wilke's method and the implementation of MUTATION++. It is well known that Sutherland's formula is inaccurate for higher temperatures but it provided a basis to perform low temperature test cases while awaiting the completion of MUTATION++. The formula is seen below in equation 2.55:

$$\mu = \mu_0 \left( \frac{T_0 + C}{T + C} \right) \left( \frac{T}{T_0} \right)^{\frac{3}{2}} \quad (2.55)$$

where  $\mu_0$  represents a reference viscosity at 273 K and  $C$  is a constant with a value of 113, as suggested by Sutherland [50]. A plot comparing Sutherland's formula with the Gupta-Yos mixture rule and the error between the two is shown in figure 2.6. As expected, the agreement is good below 1000 K but at higher temperatures the divergence between the two makes it apparent that Sutherland's law is not a valid method for calculation the viscosity of high temperature gases. This is largely because Sutherland's formula is based on rough approximations for the effective diameter of colliding particles whereas the more rigorous Gupta-Yos formulation relies on computed collision integrals and effectively accounts for the higher relative speeds of molecules at higher temperatures which result in shorter times for collisions and thus viscosity that increases in the manner shown.

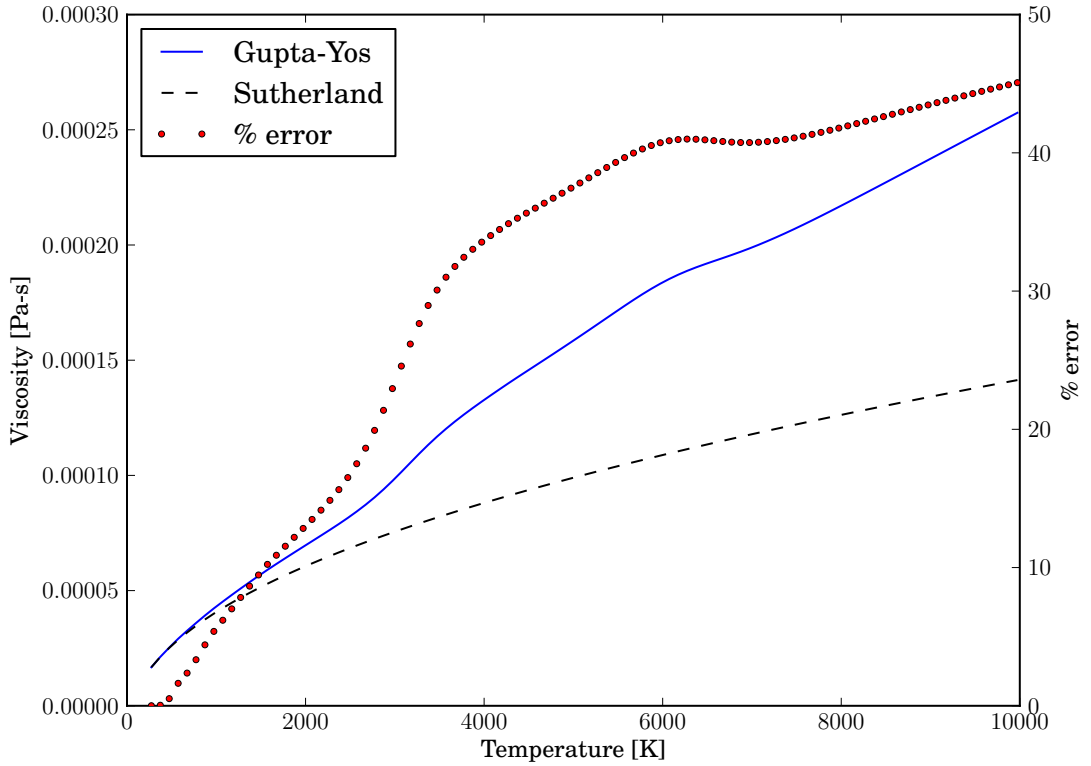


Figure 2.6: Comparison of dynamic viscosity computed with MUTATION++ and Sutherland’s formula.

### Thermal conductivity

The total thermal conductivity of the mixture is given as the sum of contributions:

$$\lambda = \lambda_h + \lambda_e + \lambda_{int} \quad (2.56)$$

where  $\lambda_h$  is the heavy particle translational thermal conductivity,  $\lambda_{int}$  is the internal thermal conductivity (which itself is the sum of contributions from rotational, vibrational, and electronic modes) and  $\lambda_e$  is the electron translational thermal conductivity. In chemical nonequilibrium, the total thermal conductivity is also known as the frozen thermal conductivity for a mixture. This approach is not complete for a mixture in LTE; in that case an

additional term must be included for the reactive thermal conductivity which, accounting for chemical reactions.

The heavy particle thermal conductivity is given by:

$$\lambda_H = \sum_i^{\mathcal{H}} \alpha_j^{\lambda_h} \chi_j \quad (2.57)$$

where  $\alpha_j^{\lambda_h}$  is a coefficient used in a Goldstein expansion [51] of a Laguerre-Sonine polynomial. This results in a linear system whose solution can be obtained with a conjugate gradient method.

The rotational, vibrational, and electronic contributions to internal thermal conductivity are calculated from:

$$\lambda_R = \sum_i^{N_{\mathcal{H}_m}} = \frac{\rho_i c_{R,i}}{\sum_{j \in \mathcal{H}} (\chi_j / \mathcal{D}_{ij})} \quad (2.58a)$$

$$\lambda_V = \sum_i^{N_{\mathcal{H}_m}} = \frac{\rho_i c_{V,i}}{\sum_{j \in \mathcal{H}} (\chi_j / \mathcal{D}_{ij})} \quad (2.58b)$$

$$\lambda_E = \sum_i^{N_{\mathcal{H}}} = \frac{\rho_i c_{E,i}}{\sum_{j \in \mathcal{H}} (\chi_j / \mathcal{D}_{ij})} \quad (2.58c)$$

where the symbol  $\mathcal{H}$  refers to all heavy particles, its subscript  $m$  refers to molecules only,  $c$  is the specific heat corresponding to a given mode, and  $\mathcal{D}_{ij}$  is the binary diffusion coefficient.

Finally, the contribution from electrons is given as:

$$\lambda_e = \frac{\chi_e^2 \Lambda_{ee}^{22}}{\Lambda_{ee}^{11} \Lambda_{ee}^{22} - (\Lambda_{ee}^{12})^2} \quad (2.59)$$

where  $\Lambda_{ee}^{ij}$  is a matrix for mass and energy transport.

## Diffusivity

Instead of computing individual species diffusion coefficients, which can be computationally expensive, mass diffusivity is reduced to a single coefficient. The basic equations to compute diffusivity are seen in equations 2.60[a,b] where  $Le_i$  is the Lewis number for a given species, i.e. the ratio of thermal diffusivity to mass diffusivity. For the present simulations, the

Lewis number is chosen as 1. This assumption is valid as the Lewis number remains on the order of unity until the onset of ionization [22].

$$\alpha_i = \frac{\lambda Le_i}{c_p} \quad (2.60a)$$

$$\alpha_T = \frac{\lambda}{c_p} \quad (2.60b)$$

Owing to the treatment of temperature as a transported scalar, the same formulation is used for thermal diffusivity,  $\alpha_T$ , but without a Lewis number scaling.

### 2.2.5 Species production rates

Dissociation, recombination, and ionization reactions are addressed with the Arrhenius equation for forward reaction rates:

$$k_f = C_f T^n e^{-\theta_D/T} \quad (2.61)$$

where  $C_f$  is the pre-exponential factor,  $n$  is an exponential factor, and  $\theta_D$  is the dissociation temperature. Determination of appropriate rate coefficients is an ongoing area of study: a given set of rate coefficients may be invalid above or below certain temperatures as a result of the conditions from which they were calculated. As such, reaction rates can be a cause of significant uncertainty in high temperature gas modeling.

The backward reaction rate is the ratio of the forward rate to the equilibrium constant, written as:

$$k_b = \frac{k_f}{K_{eq}} \quad (2.62)$$

The equilibrium constant,  $K_{eq}$  is expressed as:

$$K_{eq} = \left( \frac{P_{atm}}{R_u T} \right)^{\Delta \nu_j} e^{\left( -\frac{\Delta G^\circ_j}{R_u T} \right)} \quad (2.63)$$

where  $\nu_j$  is a stoichiometric coefficient of a species and  $\Delta G^\circ_j$  is the change in Gibbs free energy for species  $j$ .

Chemical reactions occurring within the plasma can be viewed as a balance of some number of moles of each species being created and destroyed at all times (accordingly, at equilibrium the production and destruction of a given species will balance one another) and thus can be written

$$\dot{\omega}_i = \mathcal{M}_i \sum_j^{N_{reactions}} (\nu_{ij}'' - \nu_{ij}') \left[ k_{f,j} \prod_i^{N_{sp}} C_i^{\nu_{ij}'} - k_{b,j} \prod_i^{N_{sp}} C_i^{\nu_{ij}''} \right] \quad (2.64)$$

where  $i$  and  $j$  represent species and reaction indices, respectively, and  $C_i$  is the molar concentration of species  $i$ . From this expression, it is clearly seen that species production rates are strongly dependent on species concentrations and thus the pressure of the mixture or the partial pressure of each species.

# Chapter 3

## Simulations

### 3.1 Plasma torch geometry

As a first-order approximation, the geometry used in the present work is a simplified version of that found in the actual ICP torch facility owing to limitations of the NGA base code. Consequently, grid generation is wholly algebraic: coordinates in each direction are computed independently on a purely cartesian grid with any corners being sharp right angles. In the experimental facility, test articles feature rounded edges as a means of reducing heat transfer at the corners, heat load being inversely proportional to the square of the radius. As such, the emphasis of this work is on the chemical behavior of flow at the stagnation point and the fluid dynamic behavior of the bulk flow and not the details of the flow behavior around the test article.

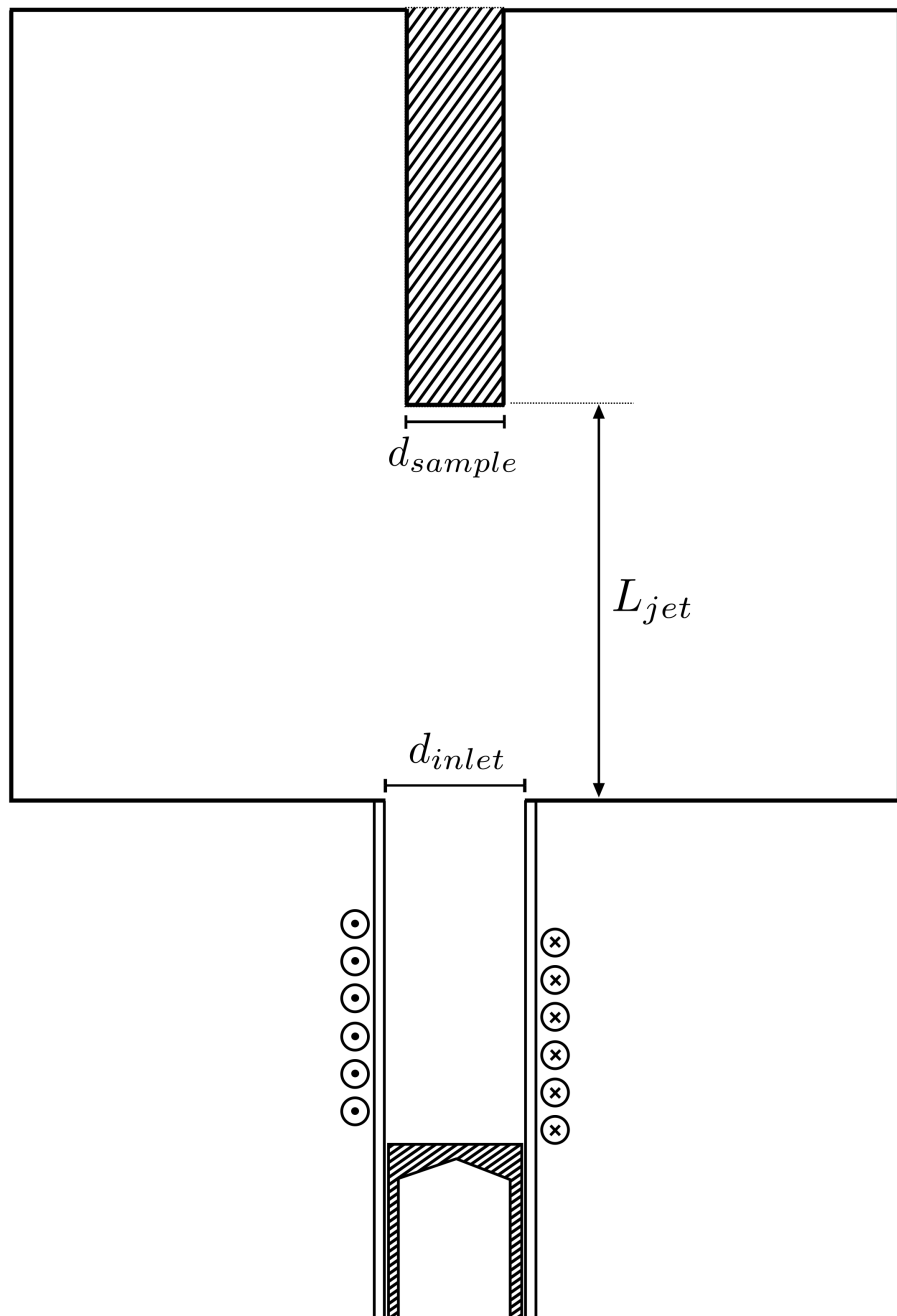


Figure 3.1: Schematic of the plasma torch test chamber. Diameter and height of chamber are not to scale in order to preserve clarity for quartz tube and sample.

Figure 3.1 shows a diagram of the test chamber between the outlet of the quartz tube and the test sample. Gas is injected in an annulus at the base of the quartz tube. Within the quartz tube, the gas is inductively heated and becomes a plasma, exiting into the test chamber as a laminar plasma jet and flowing over the TPS material sample. Table 3.1 lists values for the physical parameters of the test chamber relevant to this work. The quartz tube outlet diameter,  $d_{inlet}$ , is a fixed value, however the sample diameter,  $d_{sample}$  can be varied. Also, the distance from the quartz tube outlet to the sample surface,  $L_{jet}$ , can be varied. The values in Table 3.1 represent the geometry used in this work.

<b>d<sub>inlet</sub></b> [mm]	<b>d<sub>sample</sub></b> [mm]	<b>L<sub>jet</sub></b> [mm]
36	25	110

Table 3.1: Relevant geometric parameters.

Figures 3.2 and 3.3 show the inside of the test chamber while the torch is in operation. The internal geometry is seen from the exit of the quartz tube to the sample surface, effectively the top half of figure 3.1. In the first image,  $L_{jet}$  is approximately 110 mm. In the second, this distance is reduced by roughly half during a test to obtain a higher heat flux on the surface.

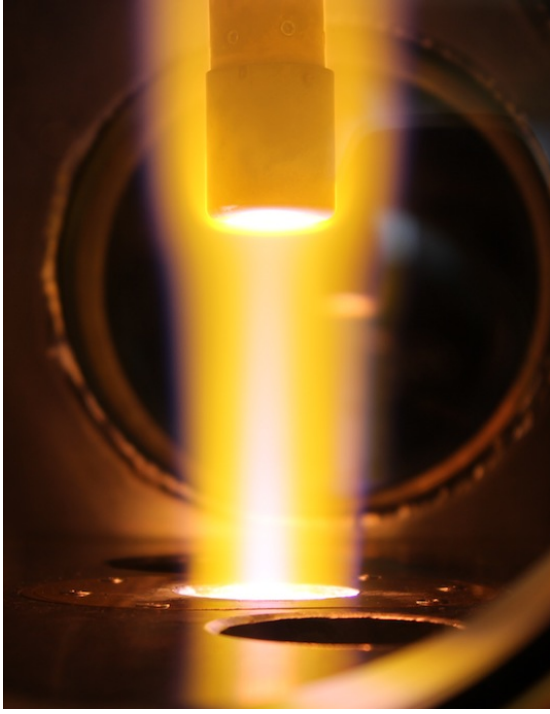


Figure 3.2: View of plasma jet within test chamber. In this image,  $L_{jet}$  is approximately 110 mm [4].



Figure 3.3: View of plasma jet within test chamber for a significantly smaller value of  $L_{jet}$ , approximately 50 mm [4].

Figure 3.4 shows a schematic for a 25 mm diameter test sample used for hot wall measurements. Owing to the previously discussed inverse relationship between diameter and heat transfer [7], some experiments have been performed using samples with smaller diameters to achieve higher heat transfer rates. All of the present work focuses on the idealized version of the 25 mm diameter geometry in which the corner radius is zero (*i.e.* a sharp right angle) instead of 3.2 mm.

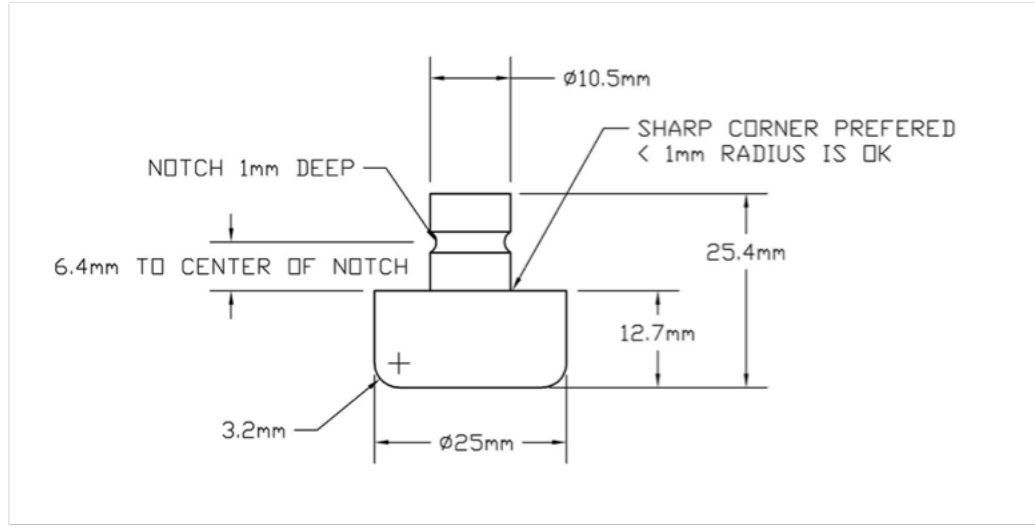


Figure 3.4: Schematic of a 25mm test article used for hot wall measurements. [5]

### 3.2 Reynolds number of the plasma jet

A brief study was undertaken to determine the range of Reynolds numbers within which the plasma torch facility operates. The plasma flow within the torch is characterized by its low density and high viscosity, both of which are direct results of the high temperature of the plasma. This combination results in a flow with a Reynolds number significantly lower than would be expected for a similar flow at lower temperatures.

The Reynolds number for the facility is calculated as:

$$Re = \frac{\rho U d_{sample}}{\mu} \quad (3.1)$$

where the sample diameter is taken as the reference length. The Reynolds number using the jet exit diameter as a reference length instead of that of the test article would yield similar results as the two are similar in scale.

A plot of computed Reynolds number versus temperature is seen in Figure 3.5. The dramatic variation in  $Re$  is a direct result of the decrease in density and increase in viscosity with increasing temperature. Although the actual ICP torch operates at a relatively high

subsonic velocity, the Reynolds number implies that the flow should be largely laminar. In practice, the plasma jet can exhibit instabilities but the present numerical model is free of fluctuations in the flow arising from the ICP torch power supply, ensuring a laminar jet with constant inlet conditions. While the present simulations do not focus on the exact ICP torch geometry, with regard to the rounded edges of the test article, the Reynolds number assumption remains accurate. From Figure 3.5, it can be seen that for a boundary layer edge temperature of, 5000 K, which is a typical value for various test gases (see chapter 4 for examples), the Reynolds number is roughly 100.

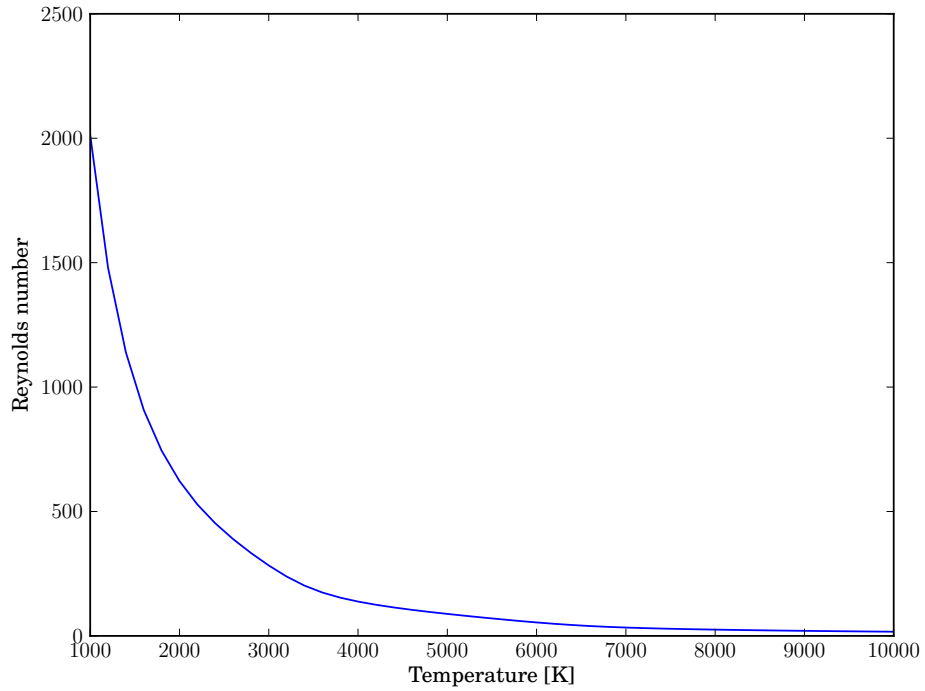


Figure 3.5: Facility Reynolds number based on sample diameter.

### 3.3 Grid considerations

#### 3.3.1 Grid generation method

Owing to the grid limitations of NGA, the grid generation method used is relatively simple. Axial grid spacing between the inlet and the sample is computed using a hyperbolic tangent function in order to achieve reasonably regular spacing in the bulk flow while time allowing for high resolution in the boundary layer above the test article. Equation set 3.2 shows the method used to build the grid from the inlet to the sample surface in the  $x$ -direction.

$$\delta = n_x - n_{x,sample} \quad (3.2a)$$

$$\tilde{x} = \frac{\delta + 1 - i}{\delta - 1} \quad (3.2b)$$

$$x_i = (L_x - L_{sample}) \left( \frac{\tanh(r_x \tilde{x})}{\tanh(r_x)} \right) \quad (3.2c)$$

where  $\delta$  is the number of grid points before the sample,  $\tilde{x}$  is a transformed coordinate,  $r_x$  is the stretching parameter (values  $<<1$  yield effectively constant spacing),  $L_x$  is the full length of the domain, and  $L_{sample}$  is the length of the test article.

Beyond the sample surface, the grid in  $x$  mirrors the grid within  $[0, L_{sample}]$ . Because the stretching in the grid spacing is now increasing with increasing  $x$  ( $dx_i > dx_{i-1}$ ), the method to generate this section of the grid differs slightly from the above approach and is seen below in Equations 3.3:

$$\tilde{x} = \frac{i + 1}{n_{x,sample} + 1} - 2.0 \quad (3.3a)$$

$$x_i = L_x - L_{sample} \left( \frac{\tanh(r_x \tilde{x})}{\tanh(r_x)} \right) \quad (3.3b)$$

This approach allows for a good degree of control over the grid, especially in the region around the sample. High aspect ratio cells are acceptable in some parts of the grid, namely the far field regions and in places where the velocity is strongly aligned with the grid. Near the sample, it is desirable to come as close as possible to achieving  $\Delta x = \Delta y$  owing to the behavior of the flow as it impinges upon the sample surface and changes direction within

a small region. In the case of a flow without a test sample (such as the study performed in section 4.5),  $r_x$  is set to a very small value allowing for constant grid spacing in the  $x$ -direction.

In the  $y$ -direction, the grid is uniform from the centerline to the edge of the inlet. From the edge of the inlet to the edge of the domain, the grid is stretched in a method similar to that used for the  $x$ -direction grid generation. Between the jet centerline (the axis of symmetry) and  $y = d_{inlet}/2$ , the grid generation is performed as:

$$dy = \frac{0.5d_{inlet}}{n_{y,inlet}} \quad (3.4a)$$

$$y(1) = 0; \quad y_j = j_{j-1} + dy \quad (3.4b)$$

where  $d_{inlet}$  is the inlet diameter and  $n_{y,inlet}$  is the number of grid points along the inlet. The boundary condition in equation 3.4b must be applied in order to successfully generate the grid. Owing to the geometry utilized in this work where the test sample diameter is always smaller than the inlet diameter, this approach has the benefit of ensuring uniform, fine grid spacing in  $y$  not just on the leading edge of the sample, but also within the region above it where there are still sharp velocity gradients.

Beyond the edge of the inlet, the grid in  $y$  is generated per the following:

$$\tilde{y} = \frac{j - n_{y,inlet} - 1}{n_y - n_{y,inlet} + 1} \quad (3.5a)$$

$$\tilde{y} = 1.0 - \tilde{y} \quad (3.5b)$$

$$y_j = 0.5d_{domain} - 0.5(d_{domain} - d_{inlet}) \left( \frac{\tanh(r_y \tilde{y})}{\tanh(r_y)} \right) \quad (3.5c)$$

where  $\tilde{y}$  is a transformed coordinate in the range  $[0, 1]$ ,  $d_{domain}$  is the diameter of the whole domain (sometimes the diameter of the test chamber, but using the full diameter of the chamber is not necessary to achieve a valid solution), and  $r_y$  is the stretching factor for the grid in  $y$ . This method allows for  $\Delta y$  to be very closely matched at the interface between the uniform and stretched regions of the grid and, with stretching, allows for a high density

of grid points towards the center of the domain with more sparse grid spacing towards the edges where the velocity field is essentially zero.

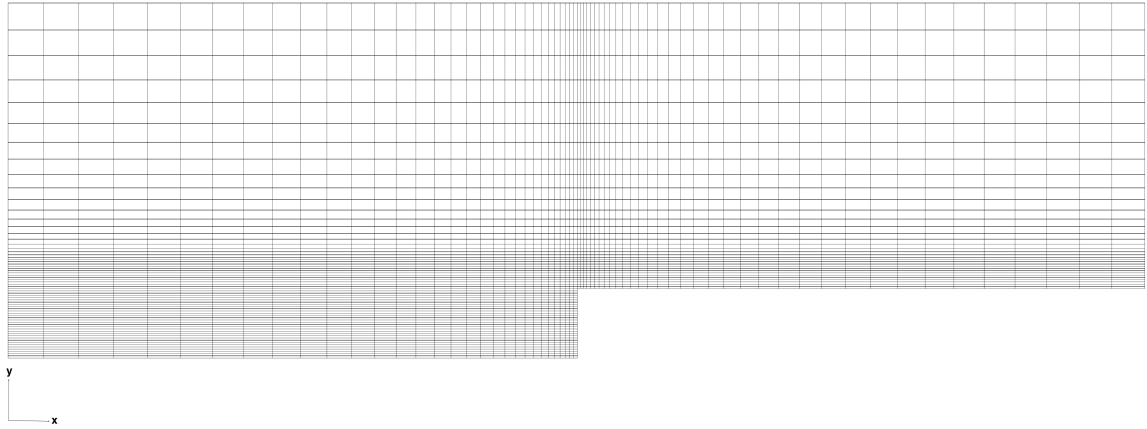


Figure 3.6: Grid for cases with a sample in the flow. Generated using equations 3.2-3.5 at low resolution ( $64 \times 64$ ) for clarity. Here,  $r_x = 1.9$  and  $r_y = 2.0$ .

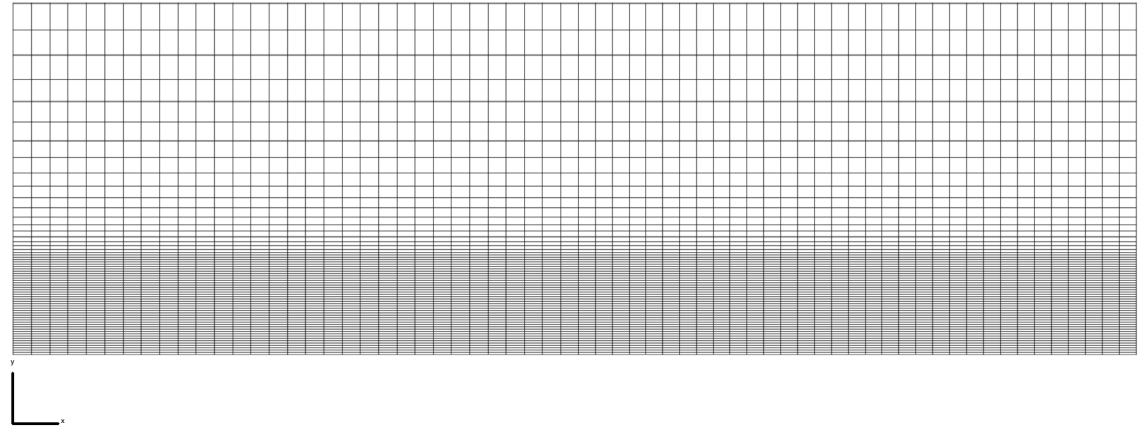


Figure 3.7: Grid for a free jet with no obstacle in the flow. Generated using equations 3.2-3.5 at low resolution ( $64 \times 64$ ) for clarity. For this grid,  $r_x = 0.001$  and  $r_y = 2.0$ .

Figure 3.6 shows the grid used for a case with a sample in the flow. The effects of stretching in  $x$  and  $y$  are visible and it is seen that cell aspect ratios near the sample

leading edge and corner are near unity, however at the low resolution shown here the aspect ratios are farther from unity than is the case for actual simulations. Figure 3.7 shows the grid at low resolution for the case of a free jet with no obstacle in the flow. It is seen that the grid is dense within the bounds of the inlet diameter and becomes more sparse towards the outer edge. As will be seen in later sections, the plasma jet does not expand significantly wider than the inlet diameter within this domain, thus this grid choice is adequate.

### 3.3.2 Grid independence

A grid independence study was performed in order to determine an appropriate grid resolution at which to efficiently and accurately simulate the plasma jet. Simulations were performed using identical conditions with increasing resolution in the grid. The test article boundary layer temperature profile was used as the metric to gauge grid independence owing to its importance in the present work. Grid independence is achieved when increasing grid resolution no longer changes the solution by an appreciable amount.

The conditions for this study were chosen to be representative of typical test conditions: the sample surface is held constant at 800 K with a catalytic efficiency of  $\gamma = 1$ . This limiting value was chosen because it represents the condition in which the surface would theoretically experience the highest heat flux and thus the boundary layer temperature profile would be most sensitive to the grid resolution near the surface. Table 3.2 summarizes the grids used for this study.

<b>Resolution (<math>n_x \times n_y</math>)</b>	<b><math>n_{x,\text{sample}}</math></b>	<b><math>n_{y,\text{inlet}}</math></b>
96 $\times$ 96	48	64
192 $\times$ 192	96	128
384 $\times$ 384	192	256

Table 3.2: Grid parameters for independence study.

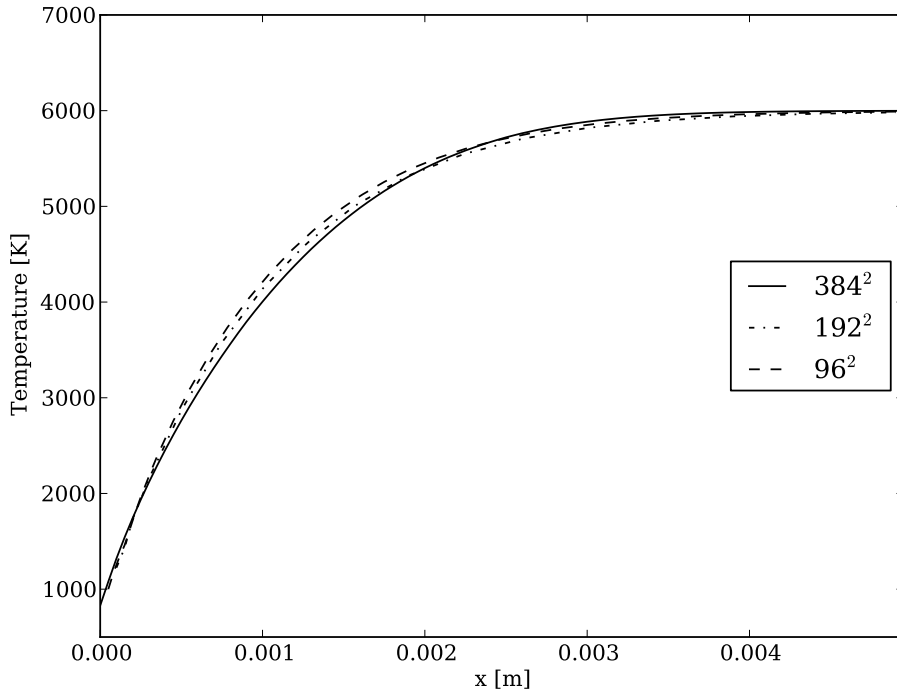


Figure 3.8: Boundary layer temperature profile computed with varying grid resolution.

A plot of temperature profiles for different grid densities is seen in figure 3.8. It is seen that despite the large differences in resolution, all grids predict a very similar temperature profile. The coarsest grid,  $n_x = n_y = 96$ , results in the steepest temperature gradient, predicting the highest temperatures across the boundary despite matching the conditions at the wall and the free stream very well. This behavior suggests that this grid can adequately model the free stream of the plasma jet but gradients within the boundary layer begin to pose problems. The grids with resolutions  $192^2$  and  $384^2$  are seen to predict much more similar profiles. Despite the similarity between the two, the fine grid with  $n_x = n_y = 384$  is selected for the simulations performed in this work. It is expected that the higher resolution will provide better stability and more accurate results for varying boundary and free stream conditions. Owing to NGA's parallel scaling ability, discussed in the next section, no loss

of performance arises from the selection of a finer grid.

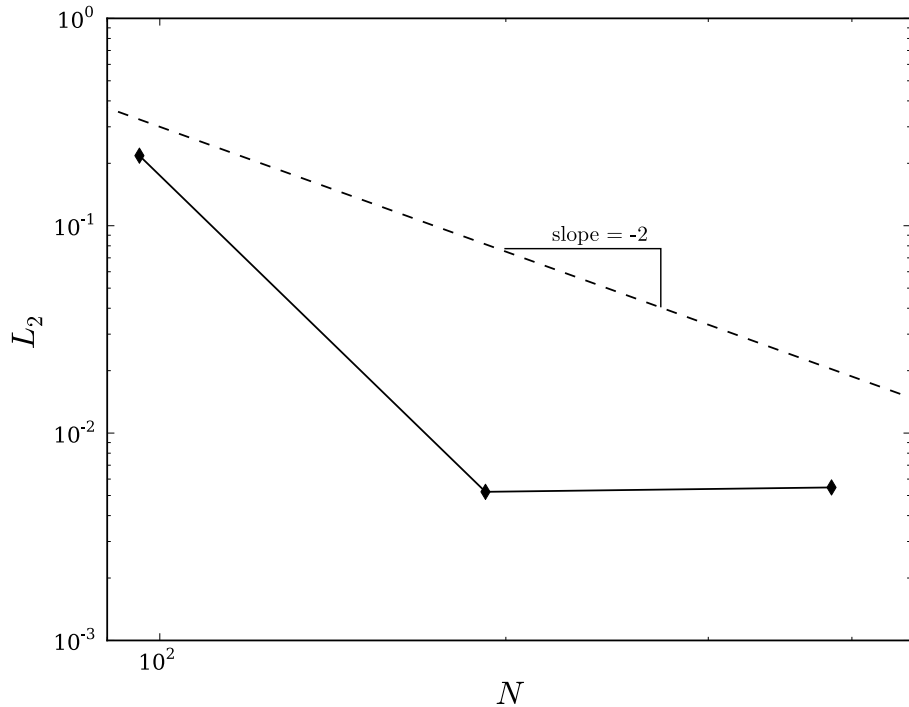


Figure 3.9:  $L_2$  error norm for temperature plotted against grid resolution,  $N = N_x = N_y$ . Near second order convergence is achieved with  $m = -1.92$ .

Figure 3.9 shows the computed  $L_2$  error norm for the temperature profiles seen in figure 3.8. Confirming the conclusion from the preceding paragraph, it is seen that there is no change in the error between  $N = 192$  and  $N = 384$ . Viewed from this perspective, it indicates that the  $N = 192$  solution may be erroneous, as the convergence of error between that and the coarse grid occurs at a rate higher than the order of any schemes utilized in this work. Thus, the use of the fine grid,  $N = 384$ , is validated.

## 3.4 Parallel scaling

Parallel scaling is a measure of the efficiency of a code when used on an arbitrarily high number of processor cores. This work does not focus on the quantification of NGA's scaling, however it has benefitted greatly from it. Ideal parallel scaling is achieved when the time to perform a simulation at one resolution on some number of processors is the same as the time required to perform the same simulation at a higher resolution and proportionally higher number of processors. Although the present work has not come close to touching the bounds of NGA's capability, it has been shown that NGA's performance scales almost linearly up to almost 50,000 processors on a grid with 1.6 billion cells [52].

## 3.5 Gas mixtures

### 3.5.1 5 species air

The present simulations use a 5 species air mixture consisting of N, O, NO, N<sub>2</sub>, and O<sub>2</sub>. This mixture was chosen for its relative simplicity while still being valid to use for comparison to experimental results obtained in the ICP torch facility. Furthermore, it has been used as a benchmark mixture in previous work [26] [27] [53]. The validity of 5 species air can be assessed by comparing its equilibrium composition with that of 11 species air at a pressure of 160 torr, which is a typical operating pressure for the plasma torch facility. This is seen in figures 3.10 and 3.11. The same data is seen on semi-log plots in figures 3.12 and 3.13 to better show the behavior of minor species. The compositions are virtually identical up to 8000 K, at which point the mass fraction of ionized nitrogen molecules becomes non-negligible. Although the plasma jet may feature temperatures above 8000 K, the boundary layer is the primary region of interest in the present work and typically only sees temperatures in that range at its outer edge. Owing to the lower temperatures, a much smaller degree of ionization occurs. Thus, the 5 species air mixture can be assumed to be valid for these studies. In addition, the selection of this mixture reduces computational cost

as it requires the integration of six fewer scalar transport equations and chemical source terms.

In addition to the reduced computational demand resulting from fewer transported scalars, the 5 species mixture considers fewer chemical reactions, namely 5 instead of the 19 required for computations with an 11 species mixture [1]. The chemical reactions considered for the mixture are seen in equations 3.6. Reaction rates for this mixture can be found in Appendix C.

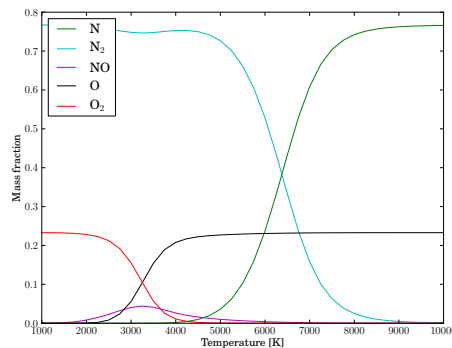


Figure 3.10: Major species mass fractions for 5 species air mixture.

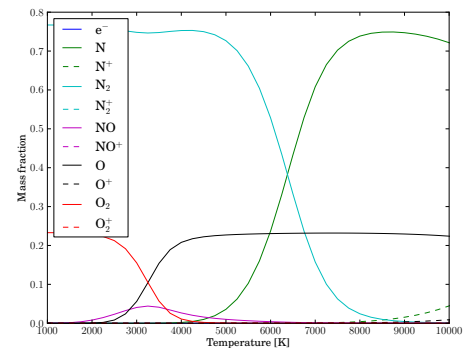


Figure 3.11: Major species mass fractions for 11 species air mixture.

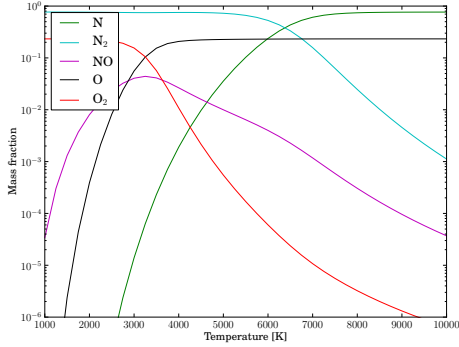


Figure 3.12: Minor species mass fractions for 5 species air mixture.

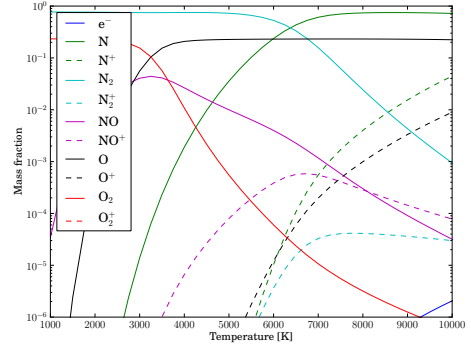


Figure 3.13: Minor species mass fractions for 11 species air mixture.

### 3.5.2 Oxygen - Argon

As an effort toward studying the effects of surface chemistry on oxygen recombination in the UVM ICP facility, a mixture of oxygen and argon is utilized. In addition to stabilizing the behavior of the plasma jet, the presence of argon in the flow lowers the partial pressure of oxygen, with the lower concentration slowing the oxygen reaction rates. The resultant partial pressure of oxygen in this mixture is similar that which occurs in air tests in the experimental facility. Achieving this condition with the addition of argon allows the plasma to maintain temperatures and total pressures similar to these tests as well.

The reaction set for this mixture is seen in equations 3.7(a-f). In experimental measurements of the boundary layer, the reverse reaction of equation 3.7a is the mechanism of interest owing to the absence of ionized species and electrons within the boundary layer in this flow regime. The mechanism in equation 3.7f also affects gas phase recombination of oxygen, but it is likely not a factor in surface chemistry. Reaction rates for this mixture are found in Appendix A.





Figure 3.14 shows the composition of this mixture in LTE at 10 kPa. It is seen that molecular oxygen begins to dissociate at roughly 2000 K and by 4000 K is fully dissociated leaving only atomic oxygen.

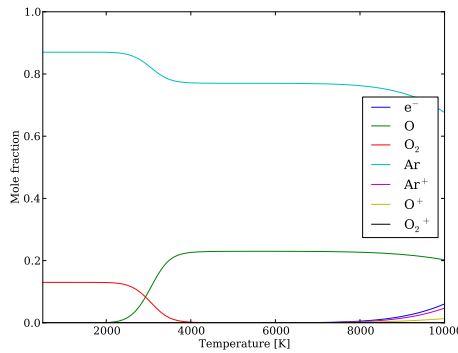


Figure 3.14: Mole fractions for  $O_2$  / Ar mixture in LTE.

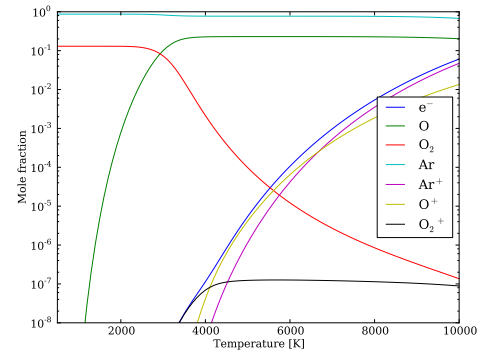


Figure 3.15: Log plot of mole fractions for  $O_2$  / Ar mixture in LTE.

Figure 3.15 shows the same data plotted on a log scale to better illustrate the minor species contribution to the mixture chemistry. It is seen that at 6000 K, electrons exhibit the largest minor species population with a value of approximately  $10^{-4}$ . At 5000 K, which is the highest boundary layer edge temperature studied in this work (see section 4.2.1), the electron mole fraction is an order of magnitude lower, at  $10^{-5}$ . With regard to the study of homogenous oxygen recombination in the boundary layer, the small population of charged species at these temperatures likely has little to no effect on the current work.

### 3.5.3 5 species nitrogen

A nitrogen mixture composed of  $\text{N}_2$ ,  $\text{N}$ ,  $\text{N}^+$ ,  $\text{N}_2^+$ , and  $e^-$  is utilized in this work to study the interaction of nitrogen plasma with test articles with various catalytic efficiencies and also to study the behavior of the plasma jet with an artificially-imposed nonequilibrium inlet condition. The reactions used in this mixture are seen below in equations 3.8[a-d]. Reaction rates for this mixture are tabulated in Appendix B.



Figure 3.16 shows the behavior of the major species mole fractions up to 10,000 K at 10 kPa. It is seen that at 6000 K, the highest boundary layer edge temperature studied for in this work, the mole fractions of  $\text{N}$  and  $\text{N}_2$  are approximately equal to 0.5.

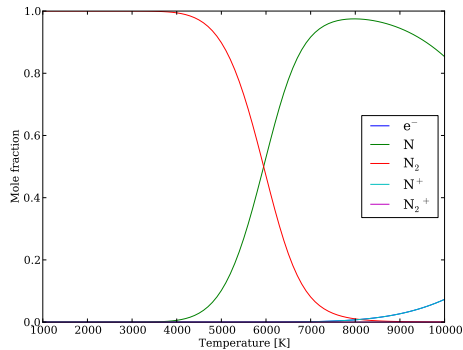


Figure 3.16: Mole fractions for 5 species  $\text{N}_2$  mixture in LTE.

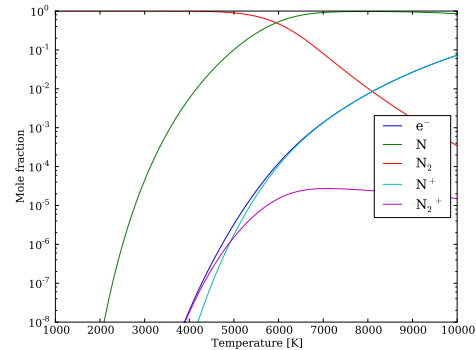


Figure 3.17: Log plot of mole fractions for 5 species  $\text{N}_2$  mixture in LTE.

Figure 3.17 shows the same data but utilizing a log scale to show the behavior of the minor species ( $\text{N}_2^+$ ,  $\text{N}^+$ ,  $e^-$ ). At 6000 K, electrons and atomic nitrogen ions both have mole

fraction of approximately  $10^{-4}$ . As with the assumption made for ionized species in the oxygen-argon mixture, it is unlikely that these species contribute anything to homogenous nitrogen recombination. This is supported when noting that at 3900 K, the mole fractions of all minor species drop below  $10^{-8}$ . In addition, the experimental setup at the UVM ICP torch facility is presently only equipped to measure neutral atomic species.

### 3.6 Inlet conditions

In an inductively coupled plasma torch, the plasma is generated within a quartz confinement tube upstream of the test chamber. Gas is injected in an annulus around the outer edge of the tube and is inductively heated within the quartz tube by the magnetic field generated with an oscillating electrical current running through copper coils surrounding the tube. Depending on the configuration and flow requirements, gas can be injected straight in or it can be injected with a swirl component. The lower portion of figure 3.1 shows a diagram of the injection region, the quartz tube, and the copper coils surrounding the tube.

Owing to the complexity of the gas injection and the previously discussed grid limitations, simulations have been performed from the quartz tube exit onward. Based on previous work that sought to quantify the chemical state of the flow in the quartz tube ([22], [23], [30]), it is assumed that as the flow enters the test chamber, it is in local thermodynamic equilibrium. Thus, inlet conditions are specified using the LTE composition for a given temperature and pressure. The inlet composition is set in such a way that the use of LTE values is not necessary and nonequilibrium conditions can also be imposed. This capability is used and studied in detail in section 4.5.

In the experimental facility, mass flow is the metric used to control the speed of the plasma jet. Computationally, this is inconvenient because the present work models only the region from the outlet of the quartz tube without considering a cold gas at uniform temperature being inductively heated. Owing to the spatial temperature and density gradients at this location, accurately imposing a mass flow boundary condition wherein velocities would

have to be calculated would be needlessly difficult. Instead, a velocity inlet is used in this work.

A previous study [54] characterized the velocity at which the plasma exits the quartz tube (*i.e.* the test chamber inlet) using a pitot probe and assumptions about the condition of the plasma at this location. The inlet velocity was determined to be 190 m/s, however it was noted that there is some uncertainty in this value. Regardless, this value is certainly within a valid, plausible range and is the inlet velocity value used in this work.

### 3.6.1 Velocity inlet boundary condition

Owing to the limitations of the present method of algebraic grid generation, a scheme for a velocity inlet was devised such that there was not a need to provide grid resolution sufficient to capture near-wall behavior at the inlet, resulting in a significant decrease in computational cost. The exact velocity inlet conditions in the facility are not known: to date, no studies have been performed to determine the velocity profile at the exit of the quartz tube. Thus, it was necessary to make an assumption about the inlet condition. Based on the work of Magin [29], it was determined that a parabolic profile would be appropriate for this work.

Within the bounds of the inlet (in this context,  $[0, R_{inlet}]$ , where  $R_{inlet}$  is the radius of the quartz tube), the velocity profile is given most generally by:

$$U_j = 8.0 U_{max} \frac{(y_{m,j} - y_{min})(y_{max} - y_{m,j})}{(y_{max} - y_{min})^2} \quad (3.9)$$

where  $U_j$  is the inlet value at a  $y$  location,  $U_{max}$  is the maximum value of the inlet velocity,  $y_{min}$  is the lower bound of the inlet (in cylindrical coordinates for a centerline-based inlet, this is zero), and  $y_{max}$  is the location of the outer edge of the inlet, equivalent to  $R_{inlet}$ . Mid-point  $y$  values are used owing to the staggered grid for scalar and vector quantities: the  $U$  component of velocity is calculated on the cell faces in  $x$ , locations which in turn exist at mid-point values in  $y$ .

Similarly, the same expression can be written for the  $W$  component of velocity ( $\theta$ -

direction in cylindrical coordinates, or swirl velocity in the context of ICP torches):

$$W_j = 8.0W_{max} \frac{y_{m,j} - y_{min}}{(y_{max} - y_{min})^2} \quad (3.10)$$

As all of the present work is performed in axisymmetric coordinates, this capability is not utilized. At all inlet locations,  $V = 0$ . For a single, centerline-based inlet, the velocity profile beyond  $R_{inlet}$  is given by:

$$U = 0; \quad V = 0; \quad W = 0; \quad (3.11)$$

The nature of equations 3.9 and 3.10 is such that the computed profiles approximate the location of a wall at  $y = R_{inlet}$ , (*i.e.*  $U = W = 0$ ) and the transition between the physical inflow and the numerical zero inflow condition is sufficiently smooth to be numerically stable.

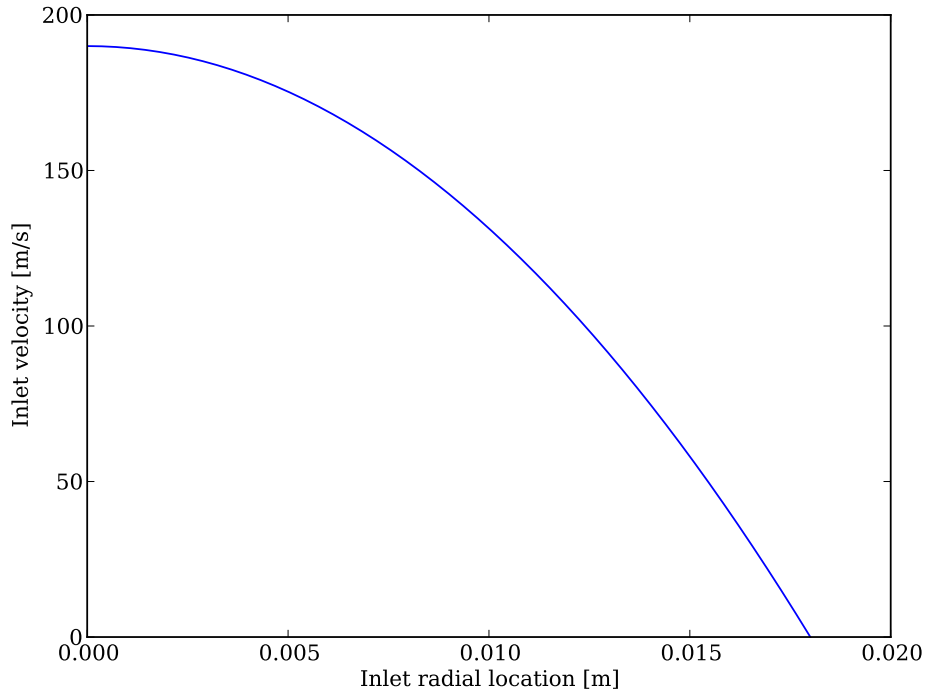


Figure 3.18: Inlet  $U$  velocity profile computed from equation 3.9 with  $R_{inlet} = 0.018$  [m], representative of UVM ICP facility geometry.

Figure 3.18 shows a plot of the inflow profile for  $U_{max} = 190$  [m/s] and  $R_{inlet} = 0.018$  [m], which is representative of the quartz tube exit in the UVM ICP facility. The transition from the physical inflow to the numerical zero inflow using this profile is smooth enough that there is no entrainment of ambient gas at the inlet and the plasma jet remains well-behaved.

### 3.6.2 Temporal inlet velocity ramping

During the start-up of the experimental facility, the plasma jet does not instantaneously reach full speed from a resting state. Rather, the velocity increases steadily until it reaches a maximum value, albeit over a short timescale. Similarly, in the present simulations, a start-up period is modeled during which the jet inlet velocity is incrementally increased in a linear fashion (in the case of constant  $\Delta t$ ) until reaching a set maximum. The inlet velocity at any time,  $k$ , during this ramping period is written as:

$$U_{in}^k = c \cdot U_{max} \Delta t + U_{in}^{k-1} \quad (3.12)$$

where  $U_{in}^k$  is the inlet velocity at the current time step,  $U_{in}^{k-1}$  is the inlet velocity at the previous time step,  $U_{max}$  is the maximum value for the inlet velocity, and  $c$  is an arbitrary factor used to control the rate at which the ramping takes place. In addition to providing a more realistic model of the starting jet, this increases the stability of the computations and helps to minimize time step limitations resulting from a large temporal velocity gradient while the jet develops.

### 3.6.3 Temperature and species inlet boundary conditions

The exact temperature profile at the outlet of the quartz tube is not known, however it is certain that the temperature scales in some way from a relatively low value at the edge of the quartz tube to a peak value at the center of the plasma flow. A 2013 study [38] sought to characterize the differences in the resulting flow field between an inlet featuring a uniform temperature profile and thus constant species composition and a non-uniform temperature profile (similar in shape to the one seen in figure 3.18) with the LTE species

composition at each temperature. It was found that the uniform profile led to better agreement between numerical results and experimentally-obtained temperature and species profiles on the boundary layer of the test article. In addition, the added complexity of a non-uniform profile did not significantly alter the bulk flow field. Accordingly, a uniform temperature and species profile was chosen as the inlet condition for this work.

### 3.7 Velocity field initialization from analytical solution

In order to more rapidly achieve a fully-developed solution, the velocity field of the entire plasma jet can be initialized from an analytical solution. Temporal ramping of the inlet velocity allows for detailed study of the effects of starting the plasma jet, but can be an inefficient approach to take when seeking a solution to the fully-developed plasma jet. Furthermore, the method of ramping is slightly non-physical in that during the start-up of the actual ICP facility, the test gas flows into the chamber at ambient temperature before the power supply is turned on and plasma is generated within the quartz tube. Thus, starting a simulation from an analytical solution for a velocity field at room temperature and with an inlet condition featuring high temperature gas is proposed as an inherently physical approach towards efficiently obtaining a solution for the plasma jet, including flow around a test article if need be.

The initial field is calculated based on the following expression:

$$U_{i,j} = U_{max} e^{\left(\frac{-100y_{m,j}^2}{(2.5R_{inlet}+0.05)^2}\right)} \quad (3.13)$$

Owing to the lack of expansion in the plasma jet, the constant width of the jet in the axial direction obtained with this equation does not hinder the advancement of the solution.

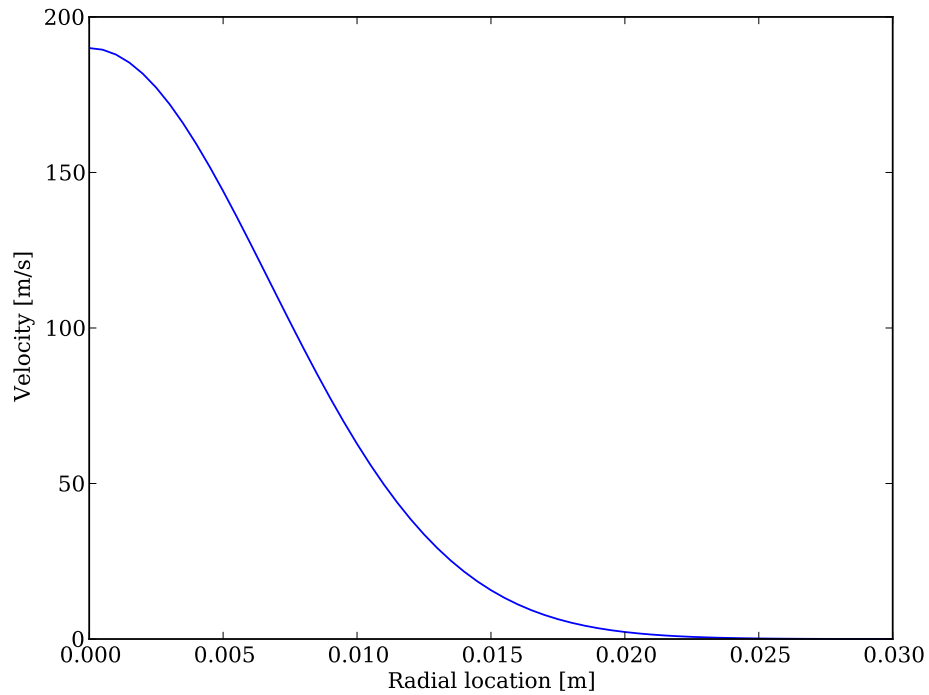


Figure 3.19: Profile of axial velocity field for simulation initialization, from equation 3.13.

A plot of the initial velocity field profile is seen in figure 3.19. This velocity profile is imposed along the entire domain for simulations both with and without a sample in the flow. For the latter, this results in abnormally high velocities within the sample boundary layer region in the first few time steps. In spite of this, these high velocities quickly dissipate and a more regular boundary layer develops around the sample.

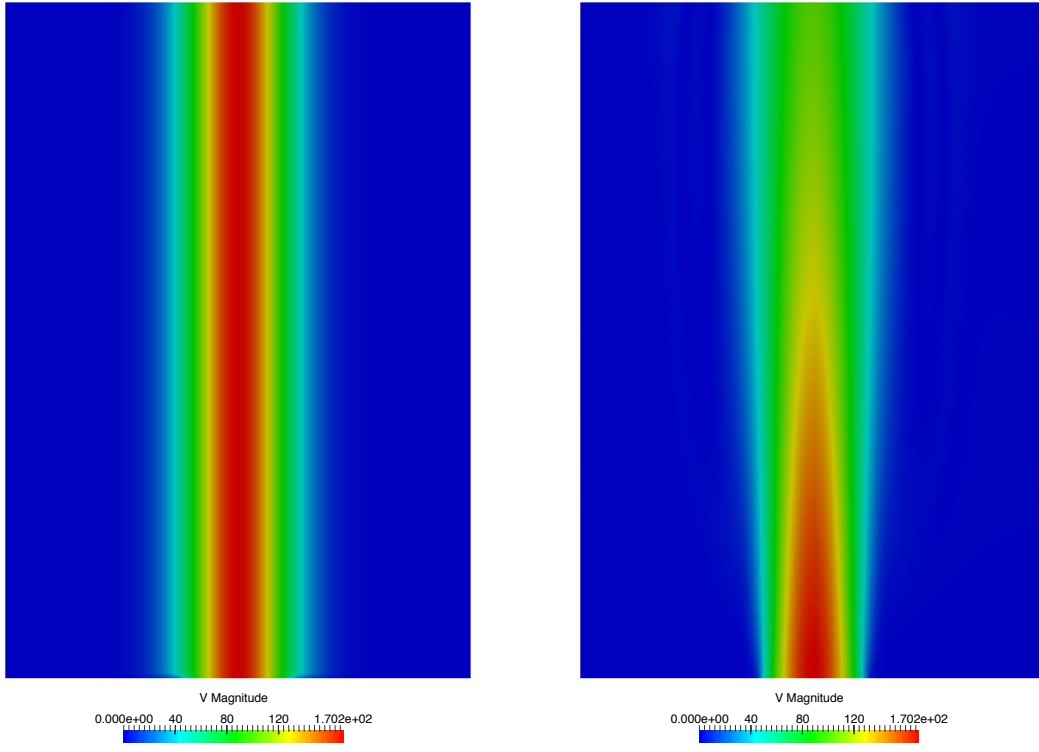


Figure 3.20: Contours of velocity for initial field calculated using equation 3.13.

Figure 3.21: Contours of velocity for fully-developed, steady plasma jet.

Figure 3.20 shows the velocity field over the entire computational domain computed from equation 3.13. It can be seen that there is no variation in the width of the jet at any axial location. Accordingly, for a fixed radial location, the velocity is identical at all axial locations. As discussed previously, this velocity field initially exists at the low temperature conditions found in the test chamber prior to torch start-up. Figure 3.21 shows the fully-developed, steady plasma jet that develops from the field seen in the previous figure. This velocity field develops after the torch is started and high temperature gas is transported along the the jet, resulting in gradients in the axial and radial directions in temperature, velocity, density, and composition. It is seen that the fully-developed plasma jet does not expand significantly over this range owing to the low density and high viscosity of the plasma.

# Chapter 4

## Results

Multiple sets of simulations were performed to assess the performance of the implementation of finite rate chemistry and high temperature gas properties in NGA: a study was performed quantifying the code's performance relative to experimental measurements; a code-to-code validation was performed based on an experimental test case; finally, simulations were performed studying nonequilibrium behavior of the plasma jet in a way that could not easily be replicated experimentally.

Numerical experiments were performed to compare experimental determinations of TPS material catalytic behavior with computational results. This series of simulations used two mixtures: argon-buffered oxygen and nitrogen. Freestream temperatures between 4500 K and 6000 K and wall temperatures between 650 K and 1500 K were studied for those mixtures over a range of experimentally-determined and limiting ( $\gamma = [0, 1]$ ) catalytic recombination probabilities. Results from these simulations are compared to experimentally-obtained results for test materials including cold quartz, copper, and monolithic silicon carbide ( $\alpha$ -SiC); these materials represent a wide range of catalytic behaviors for oxygen and nitrogen recombination. In general, good agreement was found between numerical and experimental results within the estimated experimental error.

A code-to-code validation exercise was performed relative to a previous study under-

taken the code LEMANS [39] which modeled a test case in the UVM ICP facility for a simple nitrogen mixture with varying catalytic efficiencies for the test article surface. The results show good agreement with the previously published data, suggesting that the present implementation of high temperature gas capability to NGA is sufficient and yields accurate solutions for simulating the UVM ICP facility.

Another series of numerical studies were performed investigating the nonequilibrium behavior of a nitrogen plasma free jet without a test article in the flow using a nonequilibrium inlet condition. Specifically, a significant overpopulation of atomic nitrogen was specified at the inlet in order to observe if, and how, the state of the gas trends towards local thermodynamic equilibrium within the jet. Two parametric studies were performed: the first used artificially altered recombination reaction reaction rates at a constant pressure; the second used the standard accepted reaction rate set while varying the operating pressure of the torch.

## 4.1 Experimental technique

Within the UVM ICP facility, translational temperature and relative species mole fractions are measured using two-photon absorption laser-induced fluorescence (TALIF, or two-photon LIF). Light at 532 nm is emitted from a frequency-doubled Nd-YAG dye laser which in turn pumps a tunable dye laser with a wavelength range of 600-700 nm. This light is frequency-tripled through a harmonic oscillator which generates ultraviolet light in wavelengths between 200 and 233 nm. The available wavelength is dependent upon the dye used within the tunable dye laser. The range of 200-233 nm is suitable to measure the two-photon absorption transitions of oxygen and nitrogen atoms relevant to the present study. The ultraviolet light is split and sent to the ICP torch and microwave discharge flow reactor (MDFR). The MDFR is used to obtain absorption measurements at a known temperature and pressure (300 K and 0.5 torr, respectively). Assessing the signal from this known condition allows for a calculation of the laser line width, which is necessary to

determine temperature within the plasma jet. In both the MDFR and the ICP torch, laser pulse energy and LIF signal are measured. The configuration is such that the laser beam through the ICP torch can be moved normal to the stagnation point of a test article, allowing for spatially-resolved measurements of the boundary layer. A schematic of the experimental configuration can be seen in figure 4.1.

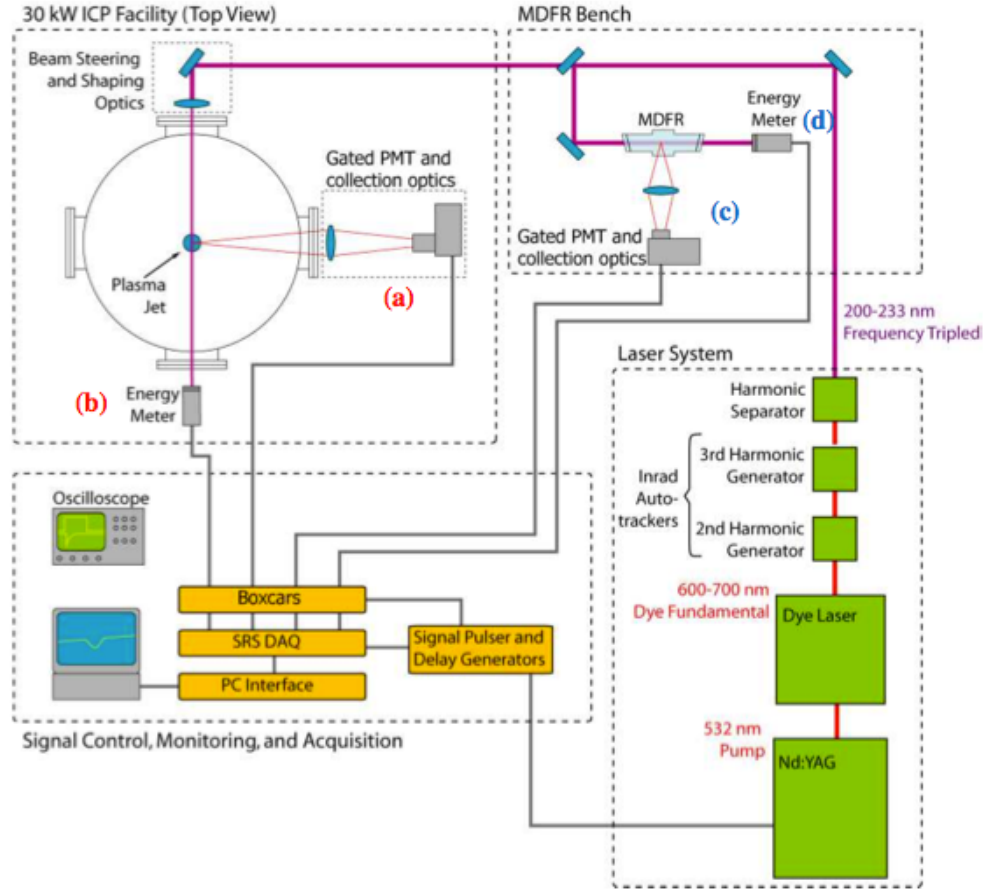


Figure 4.1: Schematic of TALIF measurement configuration in the UVM ICP facility. [6]

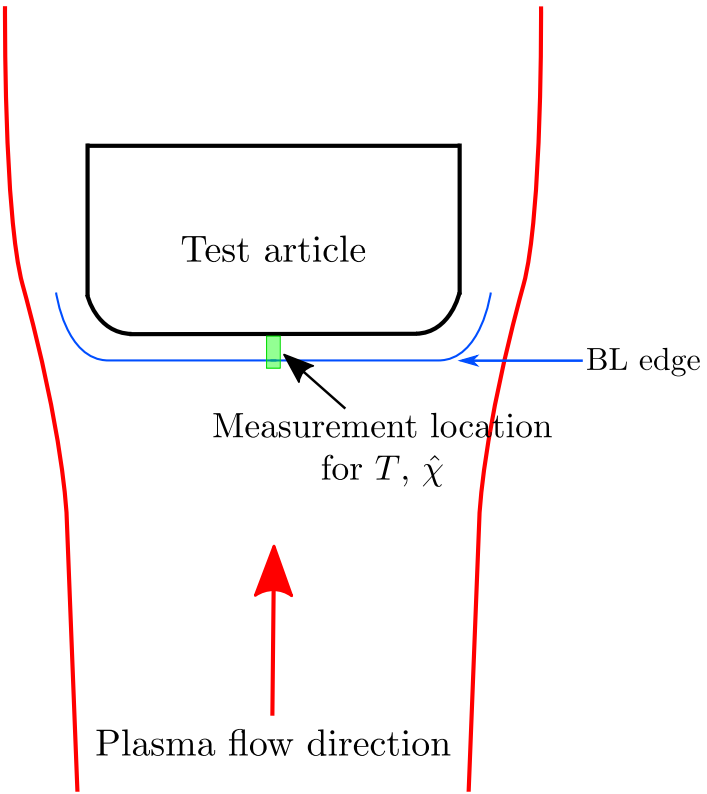


Figure 4.2: Schematic of stagnation point measurement location for temperature and species composition.

A schematic of the stagnation point measurement location is seen in figure 4.2. Typical experimental measurements cover the region at the stagnation point from the sample surface to an arbitrary distance beyond the boundary layer edge, typically on the order of 4-5 mm. All numerical results presented in sections 4.2 and 4.3 have been taken from the analogous location in the computational domain.

#### 4.1.1 Calculation of temperature and relative mole fractions

Translational temperature is determined from the Doppler width of the excitation line profile. Both laser line width and Doppler broadening contribute to the spectral profile, thus it is necessary to calculate the laser line width based on measurements of the known,

controlled conditions with the MDFR.

$$T_{measured} = \frac{M_i c^2}{8 \ln(2) k n_A \omega_0^2} [\Delta \omega_{T,ICP}^2 - (\Delta \omega_{T,MDFR}^2 - \Delta \omega_{D,MDFR}^2)] \quad (4.1)$$

where  $\Delta$  represents a line width.  $M_i$  is the molecular weight of the probed atomic species,  $k$  is Boltzmann's constant, and  $n_A$  is Avogadro's number. The subscripts refer to the measurement location: ICP for the test chamber and MDFR for the flow reactor.

Owing to uncertainties in the temperature measurement due to a broad laser line width, a fit is performed to on the measured translational temperature profile with the measured wall temperature serving as an anchor point:

$$T_{fit} = f(T_{measured}, T_{wall}) \quad (4.2)$$

Using the curve fit for temperature, the number density of the plasma flow is calculated from the ideal gas law:

$$n_{fit(y)} = \frac{P_{\text{static}}}{k_B T_{fit}(y)} \quad (4.3)$$

where  $y$  represents a location within the boundary layer above the sample surface. With the total number density of the flow, it is possible to calculate the mole fraction of the probed species based on the ratio of the integrated area of the signal to the number density.

$$\chi_i = \frac{n_i}{n_{\text{total}}} = \frac{\text{area}(y)}{n_{fit}(y)} \quad (4.4)$$

Finally, the mole fraction at each point in the boundary layer is scaled to the value at the boundary layer edge ( $y = \delta$ ), yielding the relative mole fraction,  $\hat{\chi}_i$ , of species  $i$ :

$$\hat{\chi}_i(y) = \frac{\chi_i(y)}{\chi_i(\delta)} \quad (4.5)$$

#### 4.1.2 Determination of TPS material catalytic efficiencies

The following method to determine TPS material catalytic rate coefficients is thoroughly described by Meyers in [6]. Re-writing equation 2.26 in the form presented by Goulard [10],

the balance of diffusive mass fluxes at the wall is expressed as:

$$\vec{J}_{i,w} = \rho_w D_{i,w} \left( \frac{\partial y_i}{\partial n} \right) \quad (4.6)$$

where  $D_{i,w}$  is the diffusion coefficient for the atomic species and  $n$  is the coordinate normal to the wall. With more detail, this expression can be written in terms of a balance between the rate of atom production/consumption on the surface and the arriving diffusive flux:

$$k_w y_{i,w} \rho_w = \rho_w D_{i,w} \left( \frac{\partial y_i}{\partial n} \right) \quad (4.7)$$

This expression can be written in a form more convenient to the present work utilizing mole fraction:

$$k_w \chi_{i,w} n_w = n_w D_{i,w} \left( \frac{\partial \chi_i}{\partial n} \right) \quad (4.8)$$

Written in this form, it is clear that this is much better suited to measurements of relative mole fraction. Substituting in relative mole fraction and re-arranging to solve for the reaction rate,  $k_w$ , it is written:

$$k_w = \frac{D_{i,w}}{\hat{\chi}_{i,w}} \left( \frac{\partial \hat{\chi}_i}{\partial n} \right)_w \quad (4.9)$$

After determining the gradient of the relative species mole fraction at the wall, Goulard's expression for the catalytic rate coefficient  $\gamma$  is given as:

$$\gamma_i = \frac{k_{i,w}}{\sqrt{RT_w/2\pi M_i}} \quad (4.10)$$

$\gamma$  values computed using this expression can then be implemented as a parameter for the catalytic boundary conditions implemented in NGA.

## 4.2 Argon-buffered oxygen mixture in UVM ICP facility

A series of simulations was performed using a mixture of argon and oxygen as the gas mixture (see section 3.5.2 for more details about the mixture chemistry). The intent of these simulations was to compare the performance of NGA to experimentally-obtained results for translational temperature and relative oxygen atom mole fractions within the boundary layer of a test article. The reference data and conditions for these test cases is found in [6]. Argon was introduced in order to reduce oxidation rates, owing to the dependence of reaction rates on species concentration seen in equation 2.64.

The original experiments were performed using three sample materials: copper, cold quartz, and monolithic silicon carbide ( $\alpha$ -SiC). Copper was chosen for its strong catalytic effects for oxygen recombination. Cold quartz was used because it is typically weakly catalytic for oxygen recombination and serves as a low-catalytic reference.  $\alpha$ -SiC was used as it represents a slightly more realistic TPS material choice, with a catalytic efficiency slightly higher than quartz. Both the quartz and copper samples are water-cooled whereas the  $\alpha$ -SiC is allowed to reach a higher temperature without cooling.

<b>Case</b>	<b><math>T_\infty</math></b>	<b><math>T_{wall}</math></b>	<b>Experimental <math>\gamma</math></b>	<b>Surface material</b>
O <sub>2</sub> /Ar-1	5000	650	0.0274	Copper
O <sub>2</sub> /Ar-2	4500	800	0.000562	Cold quartz
O <sub>2</sub> /Ar-3	4500	1500	0.001057	$\alpha$ -SiC after 10 minutes in flow
O <sub>2</sub> /Ar-4	4500	1500	0.003579	$\alpha$ -SiC after 65 minutes in flow

Table 4.1: Conditions for O<sub>2</sub>-Ar simulations.

An outline of the experimental conditions is seen in Table 4.1, with the experimental  $\gamma$  values being calculated from the method in section 4.1.2. In addition to the experimental  $\gamma$  values, the limiting cases of  $\gamma = 0$  and  $\gamma = 1$  were simulated in order to show the theoretical upper and lower bounds for the relative mole fraction of oxygen within the

boundary layer. All simulations were performed at the operating pressure of 160 torr (21.3 kPa) and an ambient chamber temperature of 300 K. Within the code, transported species are represented in terms of mass fraction, but in order to directly compare numerical results with experimental results, mass fraction has been converted to relative mole fraction.

#### 4.2.1 Copper test article, $T_\infty = 5000$ K, $T_w = 650$ K

A copper test article was simulated using the experimentally-derived catalytic efficiency  $\gamma = 0.0274$  for a freestream temperature of 5000 K and a sample surface temperature of 650 K. Copper is not a realistic TPS material, however it is generally considered to efficiently promote oxygen recombination which makes it ideal for experimental assessments of catalytic behavior. This high catalytic efficiency is reflected in the relatively large  $\gamma$  value.

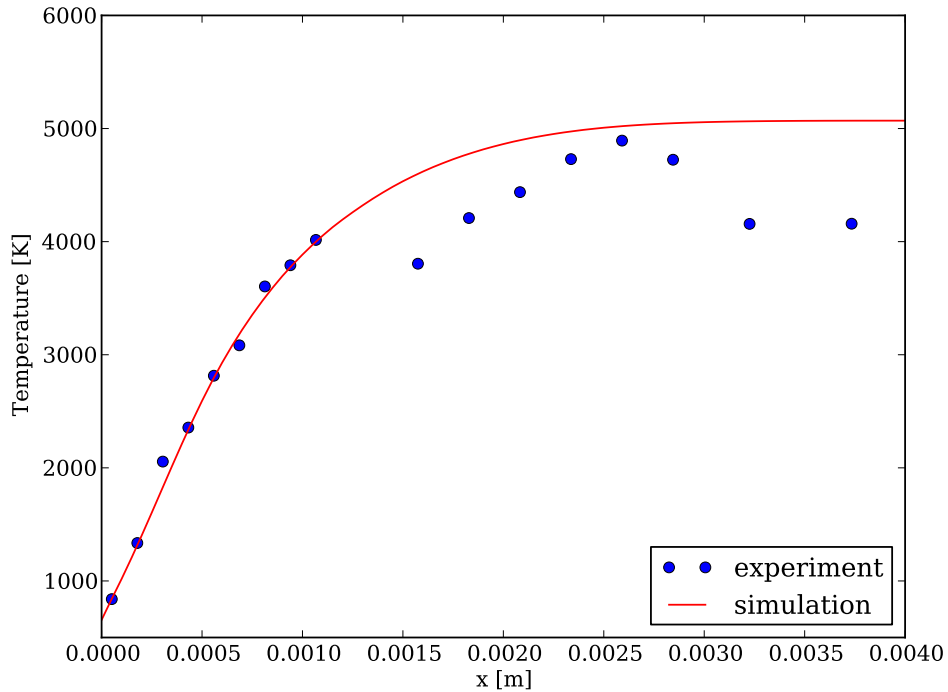


Figure 4.3: Temperature profile for case O<sub>2</sub>/Ar-1.

Figure 4.3 shows a plot of computed temperature overlaid with experimental tempera-

ture data obtained using LIF measurements. Both data sets support the assumption that the thermal boundary thickness is approximately 3 mm. Within the first 1 mm of the boundary layer, very good agreement is seen between the numeral and experimental data. Beyond this, there is some scatter in the experimental data but the overall trend remains visible.

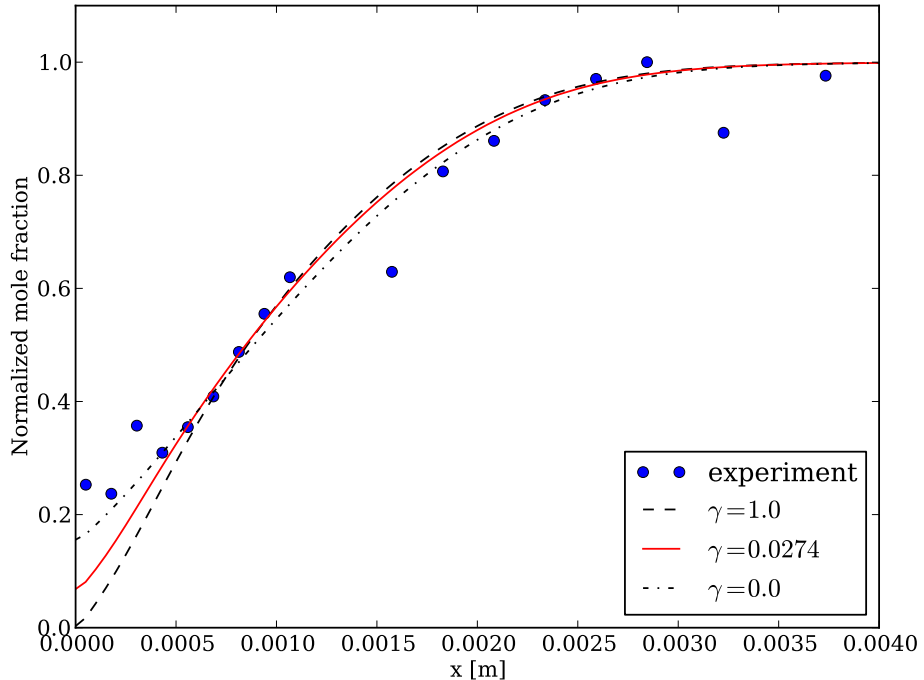


Figure 4.4: Relative O atom mole fraction from simulations compared to measured LIF data for case O<sub>2</sub>/Ar-1.

Figure 4.4 shows numerically-computed relative oxygen mole fractions plotted with experimental data. In addition to the experimentally-derived value  $\gamma = 0.0274$ , the cases for  $\gamma = 1$  and  $\gamma = 0$  were simulated to show the theoretical bounds for the boundary layer composition. It is seen that the numerical data are in good agreement with the experimental data to within 0.0005 mm of the sample surface, at which point the values diverge significantly. The experimental results suggest a relative mole fraction on the wall

of approximately 0.2, however for  $\gamma = 0.0274$ , the computed surface composition is approximately  $\hat{\chi} = 0.06$ . This discrepancy could be explained by the laser beam being clipped near the surface in experimental measurements, resulting in an erroneous signal. Even the theoretical limiting case of  $\gamma = 0$  does not quite approach the experimental wall value.

Interestingly, it is seen that within the middle of the boundary layer, the computed composition for  $\gamma = 0$  is higher than that of  $\gamma = 1$ . This a trend that is observed in all of the cases using the oxygen-argon mixture with varying degrees of overlap between the two profiles. This phenomenon may be occurring as a result of the slower oxygen reaction rates with the presence of argon in the mixture. For a lower  $\gamma$  value, the wall composition of atomic oxygen is higher, thus resulting in a shallower gradient across the boundary layer than occurs for a higher  $\gamma$  value. In the presence of slower reaction rates, it is possible that the species gradient at the wall has a stronger effect on the composition of the entire boundary layer. The wall composition is, of course, still competing with a supply of atomic oxygen from the boundary layer edge which is depleted largely through diffusion but with a minor contribution from gas phase reactions. It is this balance between diffusion and gas phase recombination that may be contributing to the behavior of the composition for different  $\gamma$  values.

#### 4.2.2 Cold quartz test article, $T_\infty = 4500$ K, $T_w = 800$ K

A cold quartz test article with a surface temperature of 800 K and a boundary layer edge temperature of 4500 K was simulated using the experimentally-computed catalytic efficiency of  $\gamma = 0.000562$ , in addition to the limiting cases of  $\gamma = 1$  and  $\gamma = 0$ . Owing to the low catalytic efficiency of cold quartz, the computed  $\gamma$  value is significantly lower than that of copper.

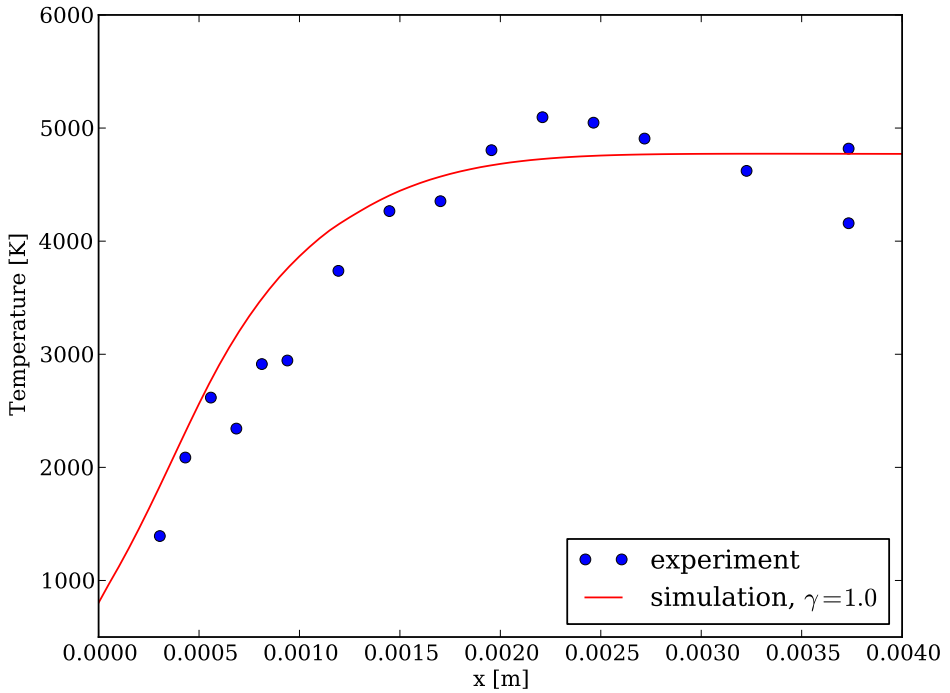


Figure 4.5: Temperature profile from simulation compared with LIF data for case O<sub>2</sub>/Ar-2

Figure 4.5 shows the computed temperature profile overlaid with experimentally-measured temperature values across the boundary layer. Generally good agreement is seen in the trend between the two data sets, however the experimental measurements fall significantly below the predicted values around 1 mm from the sample surface. At the boundary layer edge, more scatter is observed relative to the computed temperature while still maintaining the general trend of the profile.

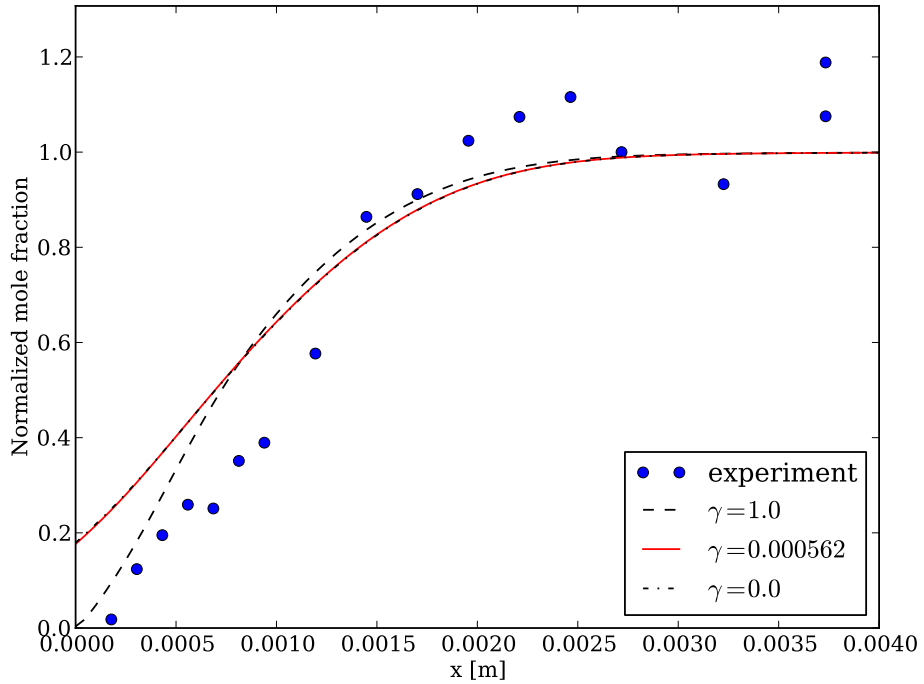


Figure 4.6: Relative O atom mole fraction from simulations compared to measured LIF data for case O<sub>2</sub>/Ar-2.

Figure 4.6 shows the computed relative mole fractions for  $\gamma = [0, 0.000562, 1.0]$  overlaid with the experimental data used to calculate the value  $\gamma = 0.000562$ . Much like the temperature profile, both data sets show a similar trend and a boundary layer thickness of approximately 3 mm. From the sample surface to  $x = 1.5$  mm, the measured values fall significantly below the computed relative mole fraction profile. Beyond that, a few points match the computed profile but generally the experimental data are greater than the computed profile. This could result from the selection of the data point representing the boundary layer edge location, with all points normalized relative to that value. However, the trend of the experimental data is such that choosing a different point with which to normalize the data would only result in better agreement between the near-surface data points or the points near the boundary layer edge, but not both.

This data set exhibits the same behavior seen in the previous section wherein the curves for  $\gamma = 1$  and  $\gamma = 0$  intersect each other, resulting in a higher atomic population mid-way through the boundary layer for higher  $\gamma$  values. As with the previous case, it is suspected that the gradient at the wall imposed through the diffusive source term is competing with gas phase reactions taking place further away from the surface near the boundary layer edge.

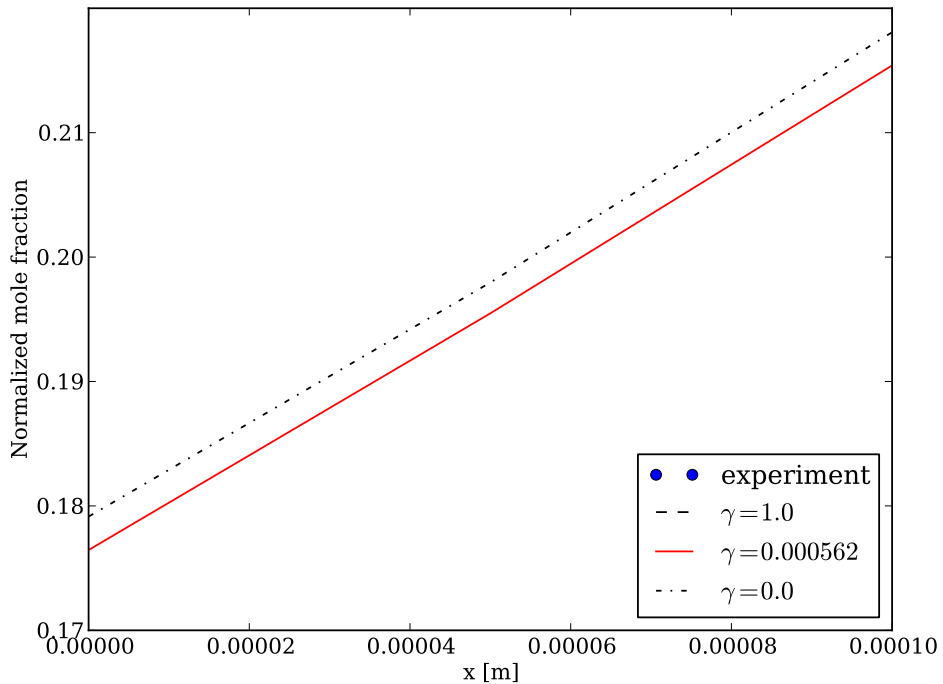


Figure 4.7: Detailed view of the 0.1 mm region above the sample surface to show slight differences in curves for  $\gamma = 0$  and  $\gamma = 0.000582$  for case O<sub>2</sub>/Ar-2.

It is also observed in figure 4.6 that the curves for  $\gamma = 0$  and  $\gamma = 0.000562$  appear, superficially, to be identical. Figure 4.7 shows these two curves in the region 0.1 mm away from the wall where it is seen that the two profiles are very similar, but not identical, to one another. This suggests that the use of cold quartz as a reference for a non-catalytic surface is a valid one. Owing to the wall temperature and hence gas phase recombination taking

place, in the effective absence of surface-promoted recombination, there is still a significant gradient in the population of atomic oxygen across the boundary layer.

#### 4.2.3 $\alpha$ -SiC test article, $T_\infty = 4500$ K, $T_w = 1500$ K

An  $\alpha$ -SiC test article with a wall temperature of 1500 K and a boundary layer edge temperature of 4500 K was simulated for the experimentally-derived catalytic efficiencies  $\gamma = 0.001057$ ,  $\gamma = 0.003579$ , and the limiting cases of  $\gamma = 1$  and  $\gamma = 0$ . The two calculated  $\gamma$  values are for the cases of a sample after 10 minutes of exposure to the plasma flow and 65 minutes of exposure, respectively.

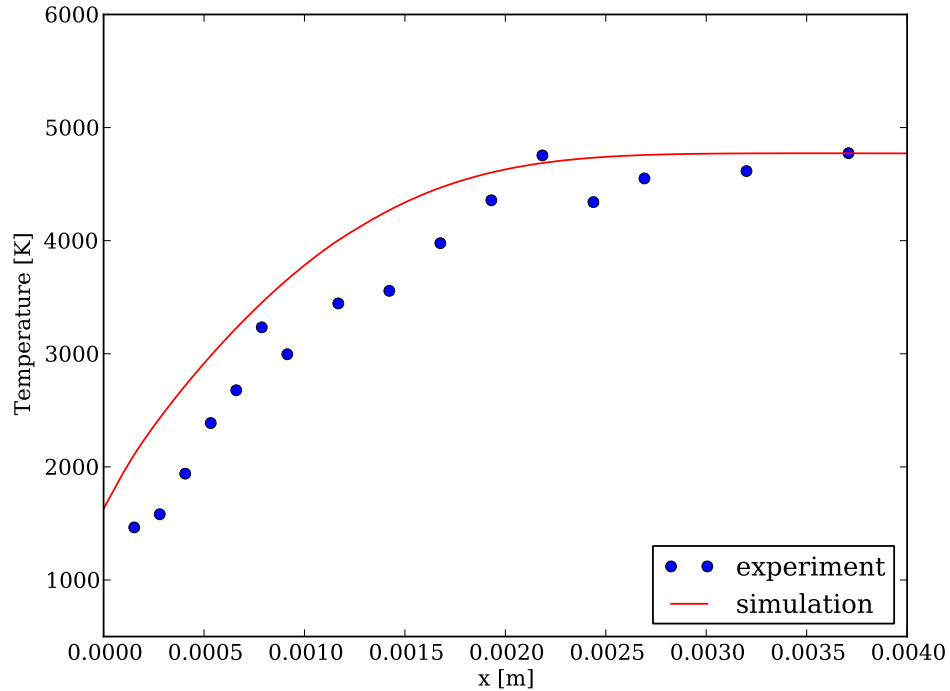


Figure 4.8: Temperature profile from simulation compared with LIF data for case O<sub>2</sub>/Ar-3,  $\gamma = 0.001057$ .

Figure 4.8 shows the computed temperature profile overlaid with experimentally-measured data for case O<sub>2</sub>/Ar-3, representing a sample that has been exposed to the plasma flow for

10 minutes with  $\gamma = 0.001057$ . Both data sets show the same trend in the temperature across the boundary layer, but the experimental data falls below the computed temperature profile at almost every point, giving the appearance that the  $x$ -coordinate of one set may be shifted. The experimental uncertainty for temperature measurements is assumed to be approximately 500 K [55]. When taking this into account, the agreement between the experimental and numerical data is largely within the bounds of the assumed uncertainty.

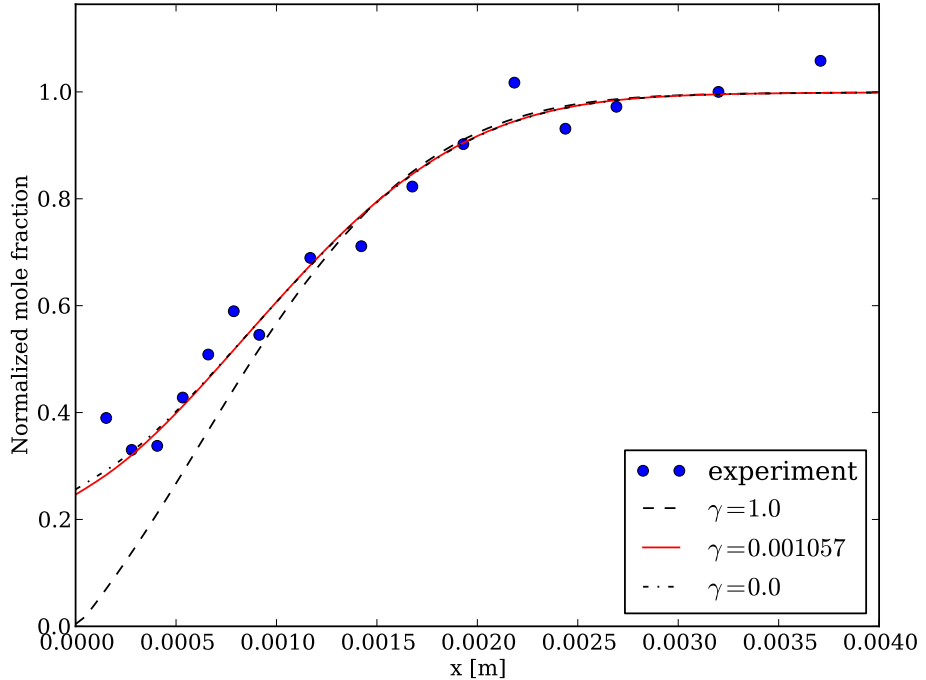


Figure 4.9: Relative O atom mole fraction from simulations compared to measured LIF data for case O<sub>2</sub>/Ar-3,  $\gamma = 0.001057$ .

Figure 4.9 shows computed relative oxygen mole fractions overlaid with experimental data for the case  $\gamma = 0.001057$ . Overall, both data sets follow a very similar trend and agree with one another. Near the sample surface, there is scatter in the experimental data which appears to suggest that the numerical results may be under-predicting the atomic oxygen population near the wall. Further out in the boundary layer, however, the agreement

between the two sets is much better. The departures from the numerical solution in the boundary layer edge region could be the result of fluctuations in the plasma jet between measurements. It is seen that the curve for  $\gamma = 0.001057$  predicts a very similar wall and gas phase atomic composition to  $\gamma = 0$ . When considered with experimental data, this suggests that  $\alpha$ -SiC after 10 minutes in the plasma flow (*i.e.* not yet considerably altered by ablative processes) is reasonably non-catalytic for oxygen recombination. Accordingly, this implies that much of the recombination taking place is likely due to gas phase reactions.

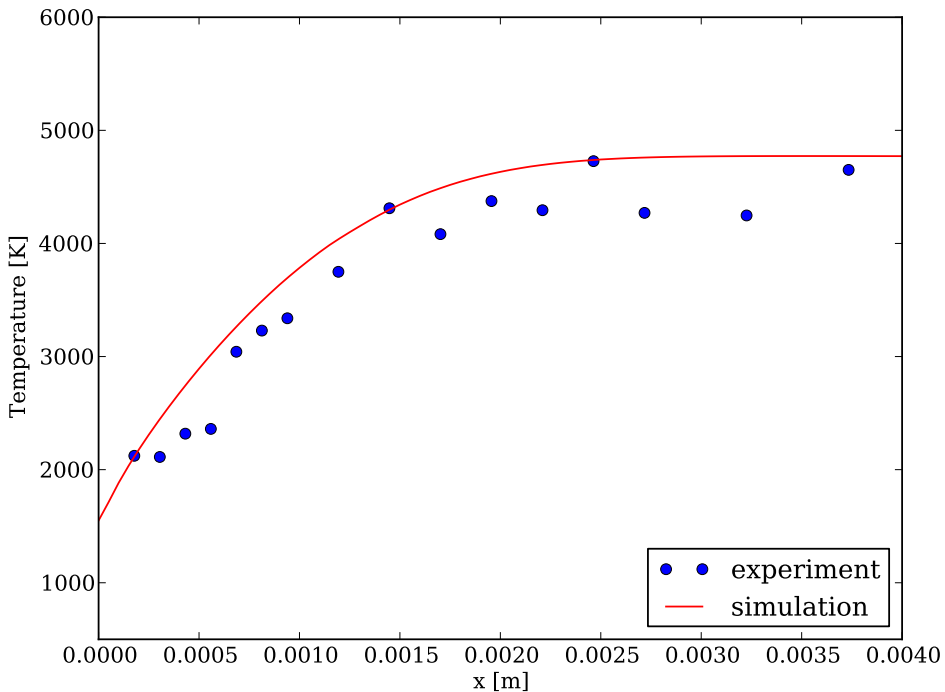


Figure 4.10: Temperature profile from simulation compared with experimental data for case O<sub>2</sub>/Ar-4,  $\gamma = 0.003579$ .

Figure 4.10 shows computed temperature overlaid with experimental data for case O<sub>2</sub>/Ar-4 with  $\gamma = 0.003579$ . As with case O<sub>2</sub>/Ar-3, there is good agreement between the measured and computed data, but the experimental data points are generally lower than the predicted value for a given location above the sample surface. Again, the predicted

temperature profile is bounded within the experimental uncertainty of 500 K.

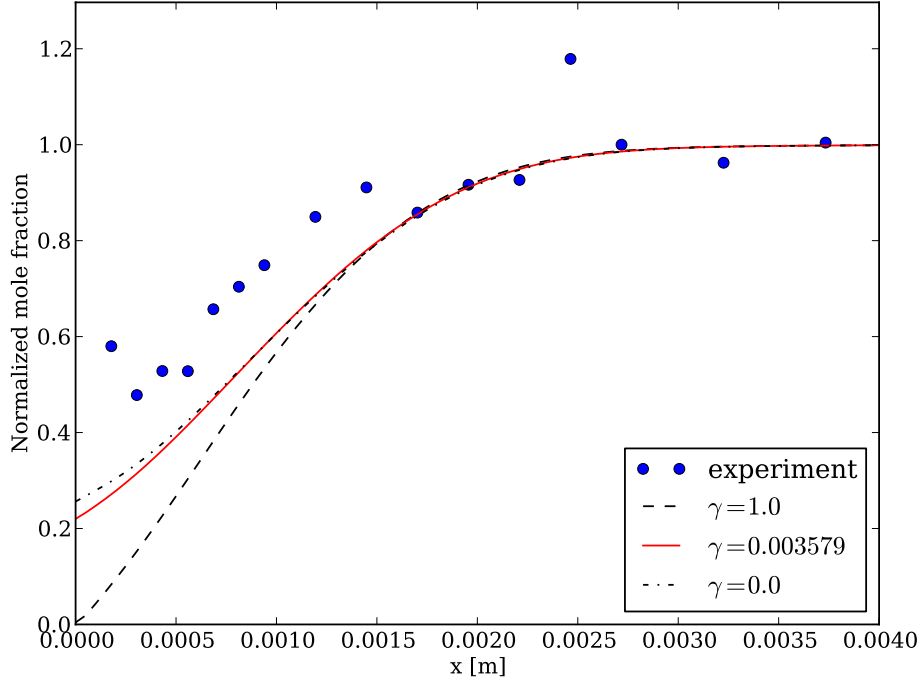


Figure 4.11: Relative O atom mole fraction from simulations compared to measured LIF data for case O<sub>2</sub>/Ar-4,  $\gamma = 0.003579$ .

Figure 4.11 shows computed and experimental relative oxygen mole fractions for case O<sub>2</sub>/Ar-4,  $\gamma = 0.003579$ . Less agreement is seen between these data sets than in the previous case, although from  $x = 1.5$  mm to the boundary layer edge, there is very good agreement between the two. The experimental data from the wall to  $x = 1.5$  mm imply that the numerical results may be substantially under-predicting the population of atomic oxygen in this region. Near the wall, the difference between the two data sets is such that even when considering the experimental uncertainty of 25%, there does not appear to be good agreement. Owing to the low  $\gamma$  value, it is conceivable that this under-prediction is due to uncertainties in the reaction rates for oxygen recombination, leading to a lower population than is achieved in reality with the steady flux of dissociated oxygen from the boundary

layer edge.

It is seen that with the slightly increased catalytic efficiency relative to case O<sub>2</sub>/Ar-3, the wall population of atomic oxygen is noticeably lower, as well as the population in the region approximately 0.5 mm above the boundary layer. Further out in the boundary layer, profiles for both  $\gamma = 0.003579$  and  $\gamma = 0.001057$  collapse onto the curve for  $\gamma = 0$ . While the difference in wall populations for the two  $\gamma$  values is small, it is significant enough to suggest that after 65 minutes in the plasma flow,  $\alpha$ -SiC undergoes morphological changes which increase its catalytic efficiency for oxygen recombination. Indeed, the notion of a change in surface composition is supported by Owens [56] who found that in oxidizing plasmas,  $\alpha$ -SiC develops a layer of SiO<sub>2</sub> after prolonged exposure.

### 4.3 Pure nitrogen in UVM ICP facility

A series of simulations were performed using a pure nitrogen mixture (see section 3.5.3 and Appendix B for details on LTE behavior and tabulated reaction rates, respectively). These simulations were performed to validate NGA by comparison to experimentally-obtained data for translational temperature and relative nitrogen mole fraction within the boundary layers of test articles with varying catalytic efficiencies and wall temperatures.

The use of a variable catalytic efficiency,  $\gamma$ , is intended to serve as a representation of the different materials used in original experiments. These materials were copper, cold quartz, and monolithic silicon carbide ( $\alpha$ -SiC). Copper is known to be highly catalytic with regard to nitrogen recombination. Conversely, cold quartz is strongly non-catalytic.  $\alpha$ -SiC is representative of a more realistic TPS material and is found to be weakly catalytic for nitrogen recombination. In the experimental facility, the quartz and copper samples are water-cooled and the  $\alpha$ -SiC sample is used without active cooling.

<b>Case</b>	<b><math>T_\infty</math></b>	<b><math>T_{\text{wall}}</math></b>	<b>Experimental <math>\gamma</math></b>	<b>Surface material</b>
N <sub>2</sub> -1	6000	650	0.0173	Copper
N <sub>2</sub> -2	6000	800	0.000755	Cold quartz
N <sub>2</sub> -3	6000	1500	0.00587	$\alpha$ -SiC

Table 4.2: Conditions for N<sub>2</sub> simulations

A table of the relevant conditions is seen in Table 4.2. In addition to the experimentally-derived  $\gamma$  values, the limiting cases of  $\gamma = 1$  and  $\gamma = 0$  were performed in order to show the theoretical limiting cases for species composition within the boundary layer. All simulations were performed at the operating pressure of 160 torr and an ambient chamber temperature of 300 K. Further detail about the experimental measurements and setup can be found in [6] and [57]. It is worth noting that the experimental data presented in this section is considered preliminary.

### 4.3.1 Copper, $T_\infty = 6000$ K, $T_w = 650$ K

A copper test article with a surface temperature of 650 K and boundary layer edge temperature of 6000 K was simulated using the experimentally-derived catalytic efficiency of  $\gamma = 0.0173$ , in addition to the limiting cases of  $\gamma = 1$  and  $\gamma = 0$ . Copper is known to be strongly catalytic to atomic nitrogen recombination and this is reflected in the relatively high  $\gamma$  value.

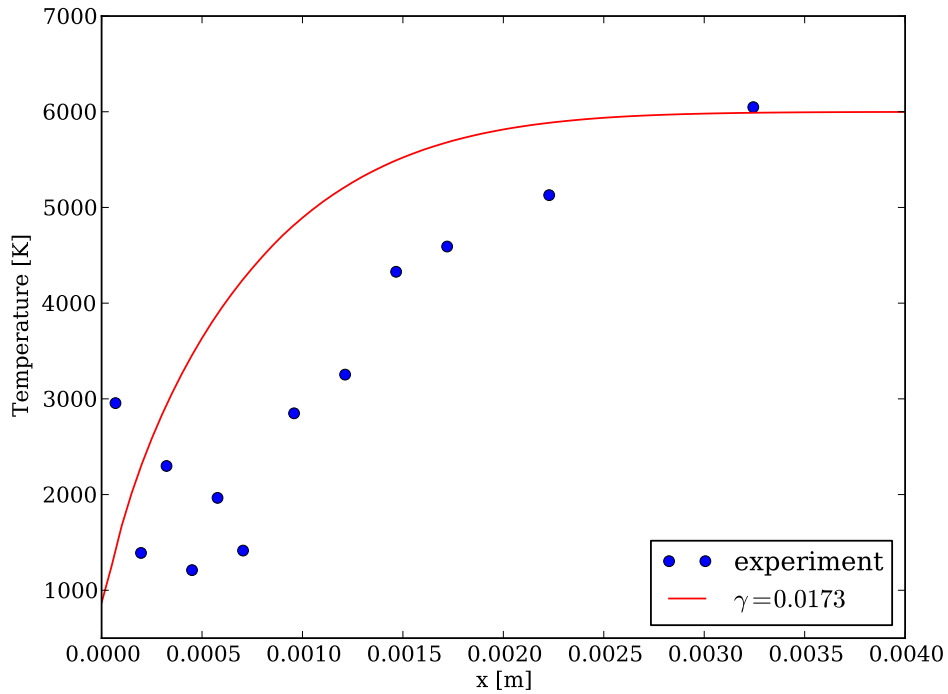


Figure 4.12: Temperature profile from simulation compared with LIF data for case N<sub>2</sub>-1,  $\gamma = 0.0173$ .

Figure 4.12 shows a plot of computed temperature overlaid with experimentally measured temperature data. It is seen that the wall and boundary layer edge temperatures are loosely in agreement while the bulk of the experimental data falls well below the simulated temperature profile. This behavior suggests that for this condition, the simulated bound-

ary layer is thinner than actually occurs in the experimental facility. Owing to the similar wall and edge conditions, the simulated data qualitatively appears to have a much steeper temperature gradient. Even when accounting for the experimental uncertainty of 500 K, there is a marked difference between the measured and simulated data. This could be the result of uncertainties at the inlet in the experimental facility which would have effects on the boundary layer thickness on the test article.

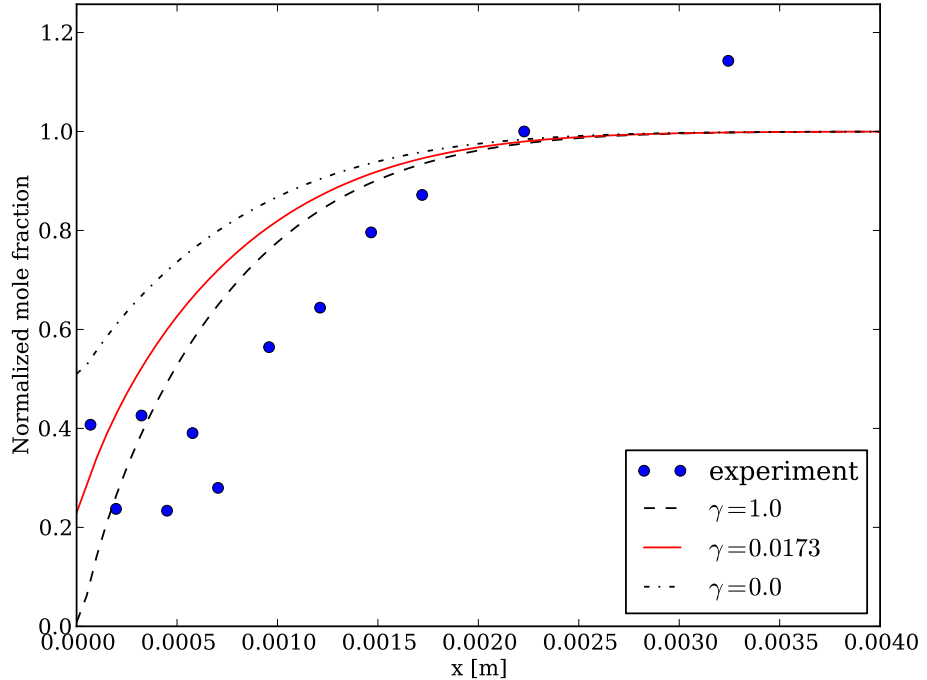


Figure 4.13: Relative N atom mole fraction from simulations compared to measured LIF data for case N<sub>2</sub>-1,  $\gamma = 0.0173$ .

Figure 4.13 shows computed relative nitrogen mole fractions for  $\gamma = [0, 0.0173, 1.0]$  overlaid with the experimental data used to derive the value  $\gamma = 0.0173$ . As with the previous plot of the temperature profile, the two data sets show a similar trend but the experimental data suggests that the actual boundary layer thickness is greater than that seen in the simulated data. In spite of this disagreement, it is seen that in both cases the relative

mole fraction of atomic nitrogen features a steep gradient near the wall, indicating that the atomic nitrogen population is being depleted. The relatively high catalytic efficiency indicates that surface recombination is likely the dominant mechanism here but the low wall temperature, and consequently low temperature in the near-wall region, may also indicate that gas phase recombination is occurring before atoms reach the wall through diffusive processes.

#### 4.3.2 Cold quartz test article, $T_\infty = 6000 \text{ K}$ , $T_w = 800 \text{ K}$

A cold quartz test article with a wall temperature of 800 K and a boundary layer edge temperature of 6000 K was simulated for the experimentally-derived catalytic efficiency of  $\gamma = 0.000755$ , in addition to the bounding cases of  $\gamma = 1$  and  $\gamma = 0$ .

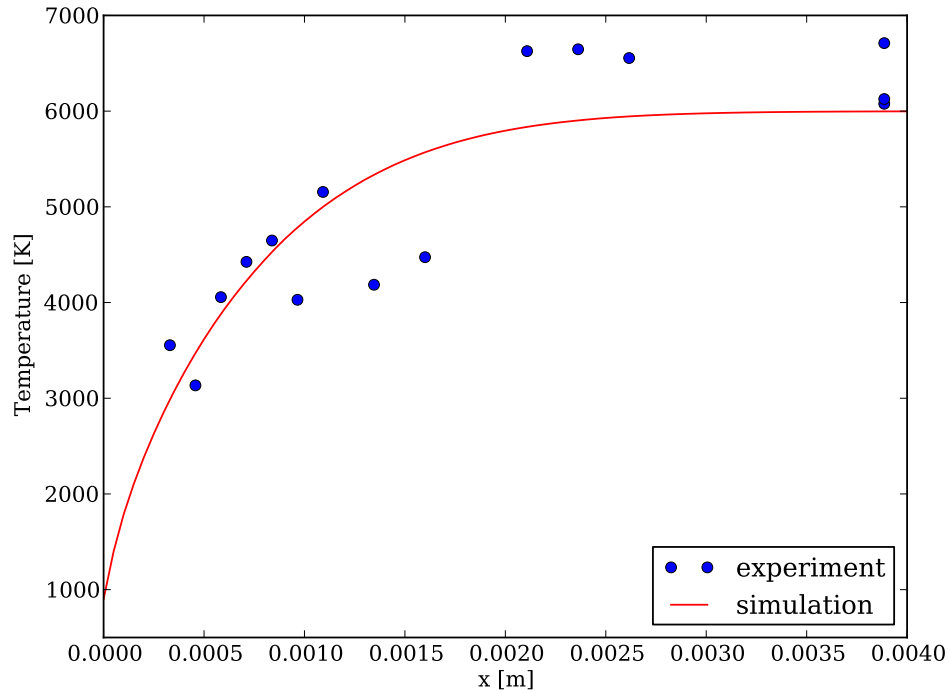


Figure 4.14: Temperature profile from simulation compared with LIF data for case N<sub>2</sub>-2,  $\gamma = 0.000755$ .

Figure 4.14 shows computed temperature overlaid with experimentally measured temperature data. Generally good agreement is seen within the first 1.5 mm of the boundary layer, although some experimental data points fall well below the computed temperature profile. At the farthest measurement location from the surface, at slightly less than  $x = 4$  mm, there are two experimental data points taken at the same location that are within the experimental uncertainty and close to the boundary layer edge temperature of 6000 K. Unlike the boundary layer thickness observed in Case N<sub>2</sub>-1, the simulation and experimental data both suggest a thickness of approximately 3 mm. This is in keeping with the value observed in other data sets within this work and serves as further evidence that the behavior seen in the previous case is anomalous.

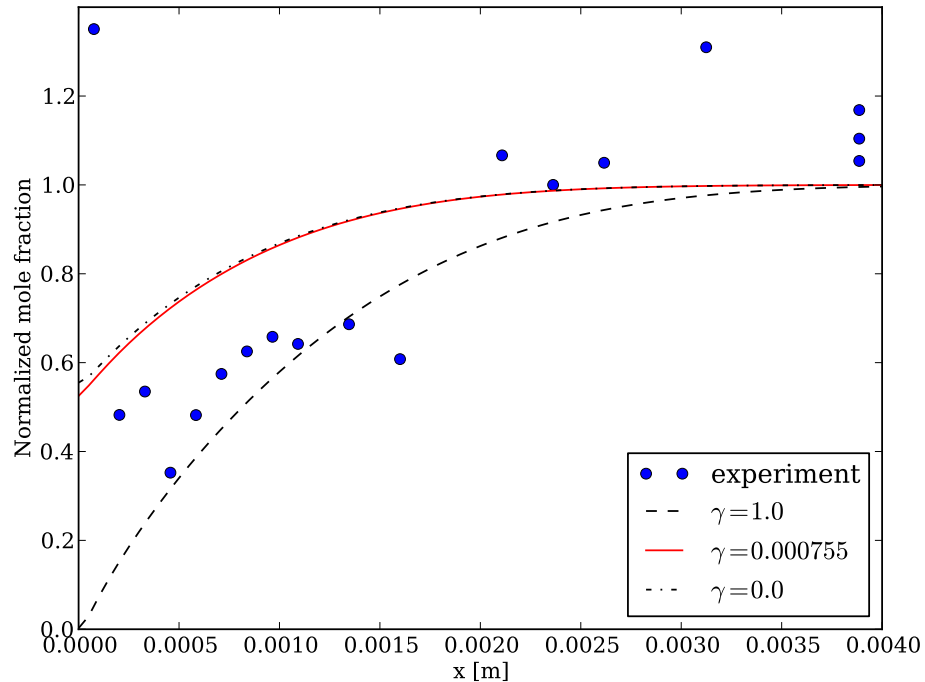


Figure 4.15: Relative N atom mole fraction from simulations compared to measured LIF data for case N<sub>2</sub>-2,  $\gamma = 0.000755$ .

Figure 4.15 shows computed temperature overlaid with the experimental data used to

derive the catalytic efficiency  $\gamma = 0.000755$ . Both data sets show similar trends of a declining atomic nitrogen populated towards the sample surface, but the simulation significantly over-predicts the atomic population within the boundary layer. The curve for  $\gamma = 0.000755$  predicts a wall composition of  $\hat{\chi} = 0.52$  while the trend of the experimental data suggests that  $\hat{\chi} \approx 0.2$  is a more realistic value. For low  $\gamma$  values in this configuration, it is apparent that the atomic nitrogen population is strongly driven by the wall catalytic efficiency. This suggests that gas phase recombination for this case may not be playing a strong role in the near-wall population in light of the fact that at the temperatures seen in this region, there should exist a minimal atomic population.

#### 4.3.3 $\alpha$ -SiC test article, $T_\infty = 6000$ K, $T_w = 1500$ K

A monolithic silicon carbide test article with a wall temperature of 1500 K and a boundary layer edge temperature of 6000 K was simulated for the experimentally-derived catalytic efficiency of  $\gamma = 0.00587$ , in addition to the bounding cases of  $\gamma = 1$  and  $\gamma = 0$ .

Figure 4.16 shows computed temperature overlaid with experimental data. Good agreement is seen between both data sets with regard to both the boundary layer thickness and the temperature profile within the boundary layer. All but one near-wall data point fall within the experimental uncertainty range relative to the computed profile and the single outlying point may be the result of the laser beam being clipped near the surface, as discussed in previous sections.

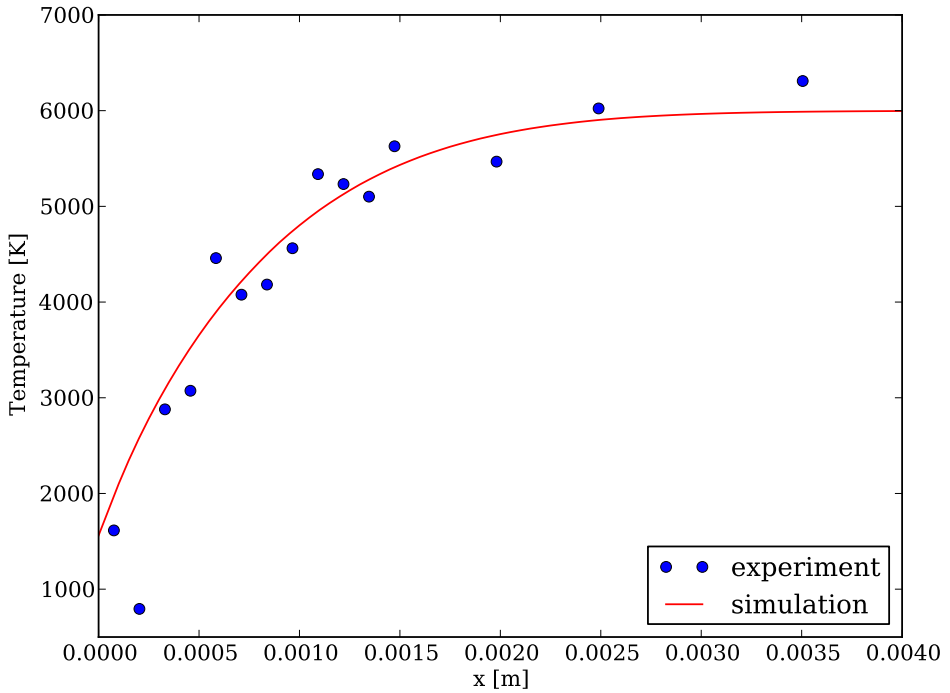


Figure 4.16: Temperature profile from simulation compared with LIF data for case N<sub>2</sub>-3,  $\gamma = 0.00587$ .

Figure 4.17 shows computed relative nitrogen mole fractions overlaid with the experimental data used to derive the catalytic efficiency  $\gamma = 0.00587$  for an  $\alpha$ -SiC test article. All but two experimental data points fall within the theoretical bounds of  $\gamma = [0, 1]$  for the boundary layer composition. There is a significant amount of scatter in the experimental data, but its trend supports the computed profile for  $\gamma = 0.00587$ . For this configuration, it is seen that this catalytic efficiency results in an atomic nitrogen population within the boundary layer that seems to fall neatly between the upper and lower bounds for the composition, suggesting that  $\alpha$ -SiC is moderately catalytic with regard to atomic nitrogen recombination. This notion is further reinforced by the catalytic efficiency falling between the values for cold quartz and copper, although it should be apparent to the reader that the relationship between  $\gamma$  and wall composition is strongly nonlinear.

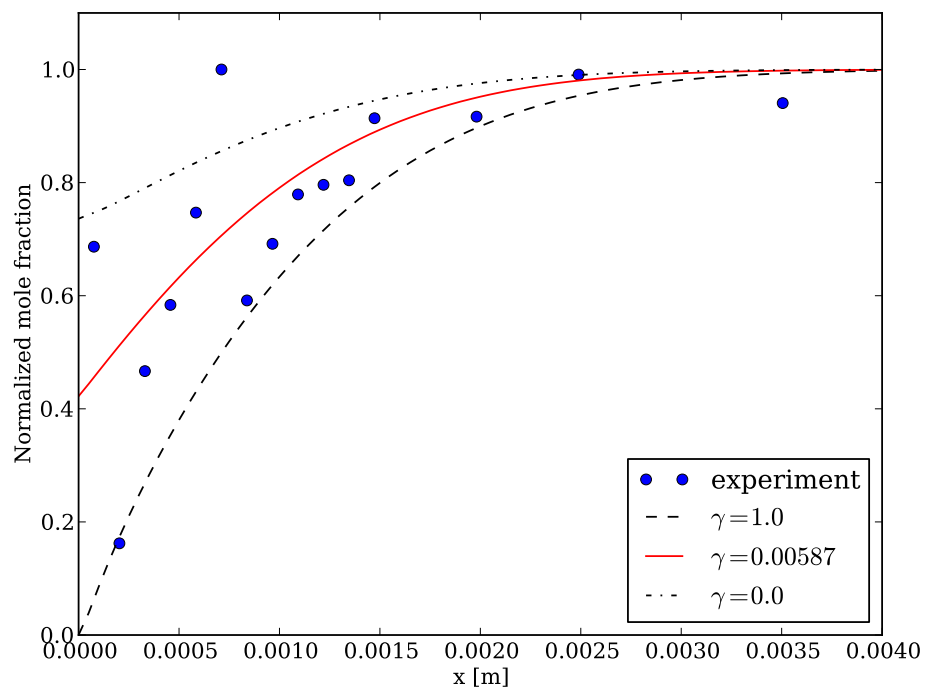


Figure 4.17: Relative N atom mole fraction from simulations compared to measured LIF data for case N<sub>2</sub>-3,  $\gamma = 0.00587$ .

## 4.4 Code-to-code validation of UVM ICP facility model

A code-to-code validation of the Mutation++ implementation in NGA was performed relative to a 2013 study [55] in which the code LEMANS [39] was used to model the UVM ICP torch facility. Validation is undertaken by direct comparison of boundary layer temperature and species concentration profiles, the latter reported in terms of relative number density.

The previous study utilized a 2 species nitrogen mixture ( $N$ ,  $N_2$ ) and one reversible reaction:



whereas the present work utilizes the 5 species nitrogen mixture seen in Appendix B using Park's rates [58]. The previous study used a finite rate surface chemistry model which simulated the test article material as a carbon surface and considered a carbon nitridation efficiency. Owing to the absence of this surface chemistry mechanism in the present work, only cases in which the nitridation efficiency was set to zero are considered, thus allowing for a direct comparison between the catalytic model implemented here and the more complex finite rate surface model.

The relevant parameters characterizing the simulated cases are seen in table 4.3. These conditions are representative of a relatively low pressure test to probe for atomic nitrogen in the experimental facility. The familiar bounding conditions of  $\gamma = 0$  and  $\gamma = 1$  are simulated, in addition to  $\gamma = 0.07$ , an experimentally-determined value representative of pure carbon interacting with a nitrogen plasma.

$P_{\text{operating}}$ [kPa]	$T_{\text{in}}$ [K]	$T_{\text{wall}}$ [K]	$\gamma$
12.5 kPa	7000	1590	0.0, 0.07, 1.0

Table 4.3: Conditions simulated for comparison between NGA and LEMANS..

Nitrogen atom composition in the boundary layer is reported here in terms of relative number density. This metric was chosen by the authors of the previous study as a way to

compare computational results to experimental results which were expressed only in relative terms. Number density of a species can be computed from the simulated quantities of mass fraction and mixture density:

$$n_i = y_i \rho \frac{N_A}{\mathcal{M}_i} \quad (4.12)$$

and is then converted to a relative value by scaling to the number density at the boundary layer edge:

$$\hat{n}_i = \frac{n_i}{n_i(\delta)} \quad (4.13)$$

In order to compare to experimental data, the authors of the previous study then scaled these values to the experimental data based on the experimental value (also in relative number density) at the measured point furthest from the sample surface. This last step results in a non-unity value at the boundary layer edge, counter to what would be expected from equation 4.13. Consequently, the results obtained with NGA have been scaled to the boundary layer edge values reported by the authors in order to make a direct comparison.

Figure 4.18 shows the computed boundary layer temperature profiles from both codes for  $\gamma = 0$  and  $\gamma = 1$ . The profile for  $\gamma = 0.07$  has been omitted from this plot because it essentially falls on top of the  $\gamma = 1$  curve. Despite the clutter, it is apparent that the temperature profiles for these catalytic efficiencies differ significantly from one another but both codes feature an similar predictions.

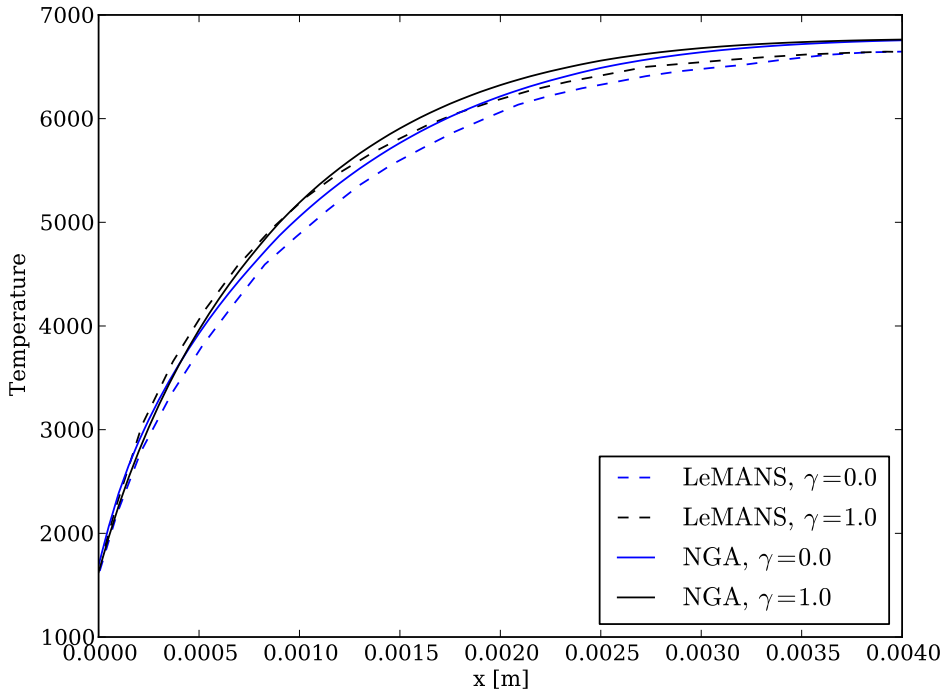


Figure 4.18: Temperature profiles from NGA and LEMANS for  $\gamma = 0, 1$ .

Figure 4.19 shows the temperature profiles from both codes for  $\gamma = 0$ . Both curves follow a very similar trend yet NGA predicts a higher ( $\sim 100$  K) boundary layer edge temperature resulting in a higher temperature across the entire boundary layer. Since the inlet conditions are identical, the higher edge temperature computed with NGA could be indicative of two possible occurrences: 1) recombination reactions in the freestream are proceeding more slowly, leading to less chemical energy being released into the flow; or 2) enthalpy decreases more slowly along the jet axis, leading to a higher-enthalpy condition at the boundary layer edge.

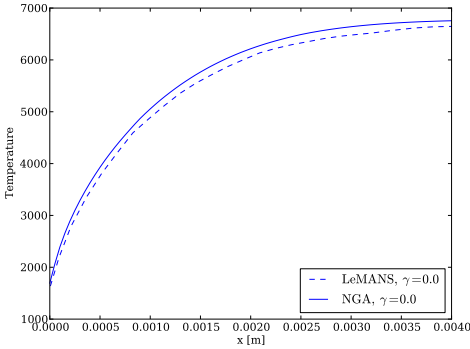


Figure 4.19: Temperature profiles for  $\gamma = 0.0$  from NGA and LEMANS.

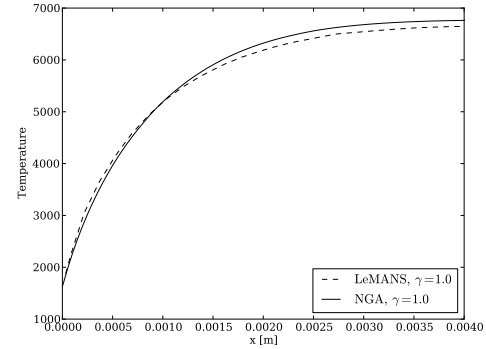


Figure 4.20: Temperature profiles for  $\gamma = 1.0$  from NGA and LEMANS.

Figure 4.20 shows the temperature profiles from both codes for  $\gamma = 1$ . Again, both curves follow a similar trend and NGA predicts a slightly higher boundary layer edge temperature, again about 100 K above the value predicted by LEMANS. At approximately  $x = 0.001$  m, the temperature profiles cross and in the near-wall region, LEMANS predicts higher temperatures. This has the result that NGA predicts a very slightly shallower temperature gradient at the wall even though the apparent boundary layer thicknesses are practically identical. The higher edge temperature with NGA could be explained by the same reasons mentioned in the discussion for the  $\gamma = 0$  temperature profile. The shallower temperature gradient at the wall likely results from a comparative under-prediction of heat released at the wall due to surface recombination, in effect the result the of differences in the chemical models applied.

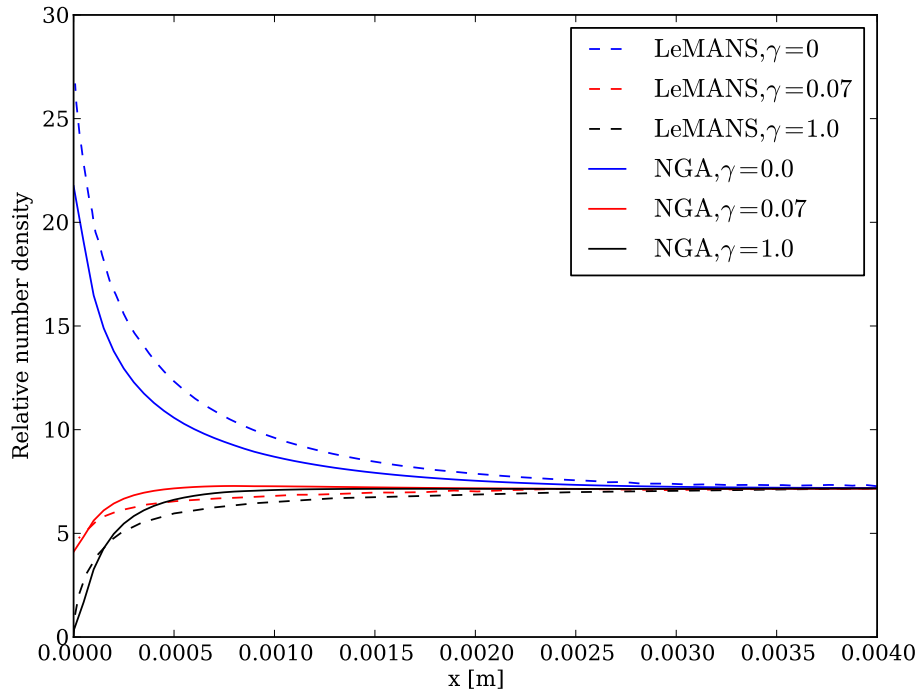


Figure 4.21: Relative nitrogen atom number density profiles from NGA and LEMANS for varying  $\gamma$  values.

Figure 4.21 shows relative nitrogen atom number density profiles across the boundary layer for all three catalytic efficiencies. For  $\gamma = 0$ , it is seen that NGA significantly under-predicts the wall population of nitrogen atoms, resulting in a much lower atomic population across the entire boundary layer. It is probable that this difference results from the use of different reaction rate sets (Park rates in NGA and Gnoffo's 1989 rates [24] in LEMANS) for the gas phase, as  $\gamma = 0$  implies that no surface chemistry takes place. The predicted wall compositions for  $\gamma = 0.07$  are very similar, however in the middle part of the boundary layer NGA predicts a slightly higher atomic population. The profiles for  $\gamma = 1$  show a trend similar to that observed for temperature: NGA predicts a higher concentration of nitrogen atoms for the outer part of the boundary layer, but near the wall the curves cross and the species gradient computed by NGA ends up being shallower. Despite this, both

codes predict the same result of a negligible population of atoms residing on the wall. This is to be expected, as  $\gamma = 1$  implies that all atoms will recombine to molecules at the wall.

The outcomes of this validation exercise suggest that NGA provides similar performance to LEMANS with regard to predicting boundary layer temperature and species concentration profiles for a simulation of the UVM ICP facility, despite it being, at its core, a very different code. The differences that exist in predictions of wall composition, and to a lesser extent temperature, can likely be explained by differences in the thermochemical models implemented in each code. Owing to the validity of the methods used by both, nothing seen here suggests that the models implemented into NGA for plasma modeling require reconsideration, rather, the results of this validation serve as a data point towards confirmation of its ability to accurately simulate high temperature, reacting plasmas.

## 4.5 Effects of nonequilibrium behavior of nitrogen on plasma jet composition

A series of simulations were performed to investigate the effect of reaction rates for nitrogen recombination on the composition of the plasma jet relative to LTE values. Experimental data obtained in the plasma torch facility suggests that when hot, graphite is highly catalytic to nitrogen recombination. The surface recombination rate may be faster than the gas phase recombination rate being driven by temperature, which when paired with a high surface temperature would result in a boundary layer that is strongly in nonequilibrium all the way to its edge. The boundary layer edge composition can also significantly affect the state of the boundary layer; this study aims to characterize the effect of nonequilibrium inlet composition on the boundary layer edge composition.

In order to study the sensitivity of gas phase nitrogen to recombination reaction rates, nonequilibrium inlet conditions were specified in order to assess the behavior of atomic nitrogen within the plasma jet. Specifically, the nonequilibrium conditions at the inlet were formulated such that there existed an overabundance of nitrogen atoms relative to the LTE composition for a given temperature. A summary of these inlet conditions is seen in Table 4.4.

Case	T <sub>in</sub>	y <sub>N</sub>	y <sub>N<sub>2</sub></sub>
LTE	6000	0.263279	0.736662
Overpopulated N atom	6000	0.5	0.5

Table 4.4: Inlet conditions for N<sub>2</sub> nonequilibrium simulations.

Nonequilibrium effects were examined in a parametric study first by varying the reaction rate for nitrogen recombination at a constant pressure. While this approach cannot be replicated experimentally, it provides insight into the role of reaction rates in the chemical composition of the plasma jet. The second study utilized fixed reaction rates and instead

varied the ambient pressure of the test chamber. This approach has the benefit of being completely physical and is possible to study experimentally. In both cases, the computed mass fraction of nitrogen is compared to the LTE values for the temperature at any given point.

The geometry used in this study is the standard configuration used in previous sections in the absence of an obstacle in the flow. The computational field extends 20 centimeters downstream from the ICP torch exit. This distance was chosen because it is significantly longer than any outlet-to-sample distance currently used in the UVM facility (indeed, using a larger distance for TPS material testing is counter to achieving high boundary layer edge temperatures) and also because it represents a viable physical range over which the plasma jet can be observed using experimental techniques. This study thus allows for an estimation of what the boundary layer edge conditions would be at a given point in the flow. Results presented in this section are taken when the jet is fully developed and no longer evolving in time.

In the interest of a visualization, Figure 4.22 shows contours of nitrogen atom mass fraction for a fully-developed jet with an LTE inlet condition. It is seen that the mass fraction appears to remain at a fairly constant value for the first half of the jet. As the jet expands and dissipates, the nitrogen atom population begins to decrease noticeably as a result of the temperature decreasing as the jet flows into the much cooler ambient gas.

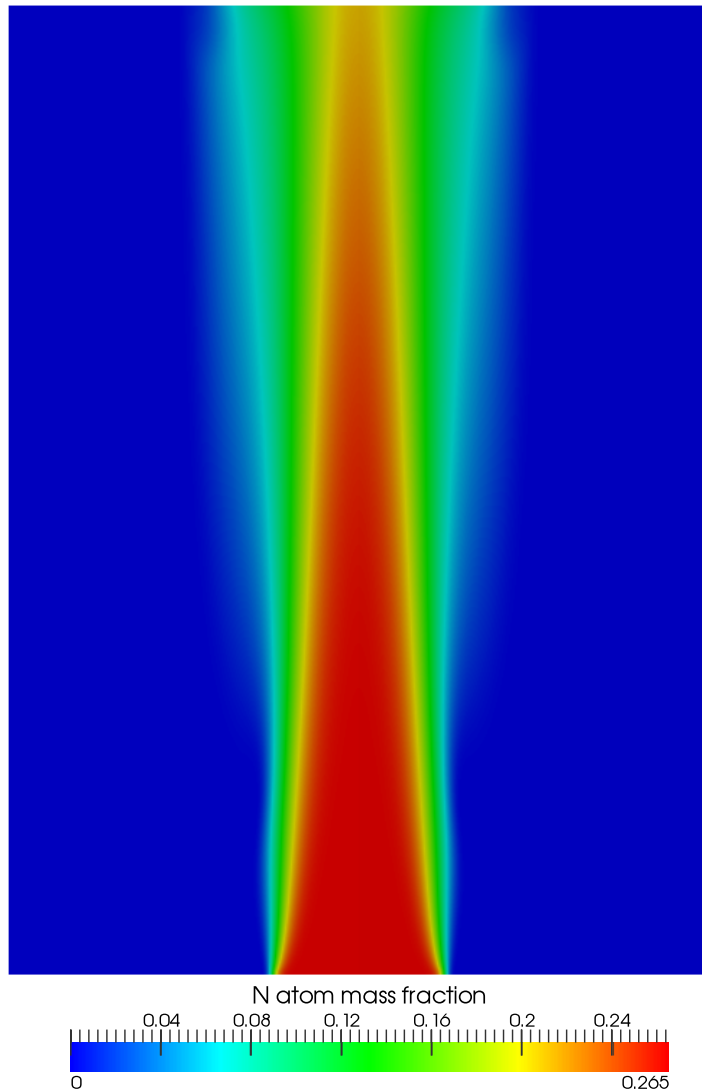


Figure 4.22: Contours of nitrogen atom mass fraction for LTE inlet conditions,  $T_{in} = 6000K$ .

#### 4.5.1 Effect of varying N atom recombination reaction rates

Simulations were performed utilizing three different scaled reaction rates for nitrogen atom recombination:  $0.1k_f$ ,  $k_f$ , and  $10k_f$ . This approach lacks the direct physical analogue of the pressure-varying approach seen in Section 4.5.2, but provides a clear view into the effects of the recombination rate on temperature and composition within the plasma jet.

Figure 4.23 shows the atomic nitrogen mass fraction along the jet centerline for the

three different reaction rates. As is expected, the mass fractions for the artificially-adjusted reaction rates serve as bounds to the case utilizing standard reaction rates. It is seen that for the slow case,  $k_f = 0.1k_f$ , recombination takes place very gradually and never converges towards the value seen for standard  $k_f$ . Although the nitrogen mass fraction for the slow case does not converge towards the standard case within this domain, over a longer domain it would be expected to eventually do so once the temperature is such that it no longer supports a nonequilibrium population of N atoms.

Conversely, and intuitively, recombination takes place very quickly for  $k_f = 10k_f$ , showing a sharp drop in N mass fraction within the first centimeter of the domain, briefly staying constant, and then decreasing along the remainder of the domain. By  $x = 0.07$  [m], it is evident that faster recombination rates result in a tendency to trend towards the standard case much faster than is seen with slower reaction rates.

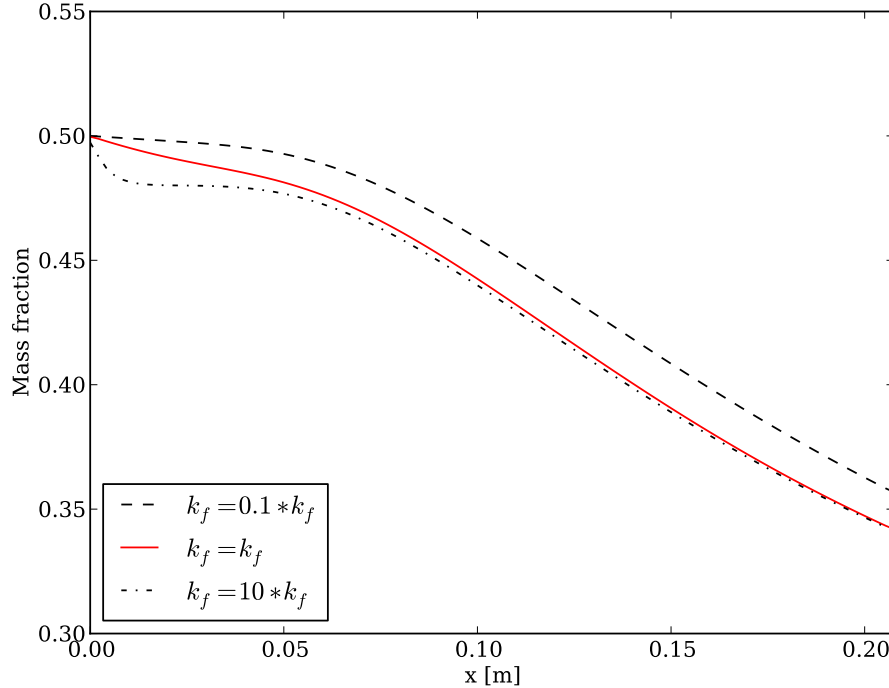


Figure 4.23: Mass fraction of N atom along plasma jet axis for varying inlet conditions.

Figure 4.24 shows the same data as figure 4.23 but zoomed to the first half of the domain to more clearly show differences in the behavior of the cases.

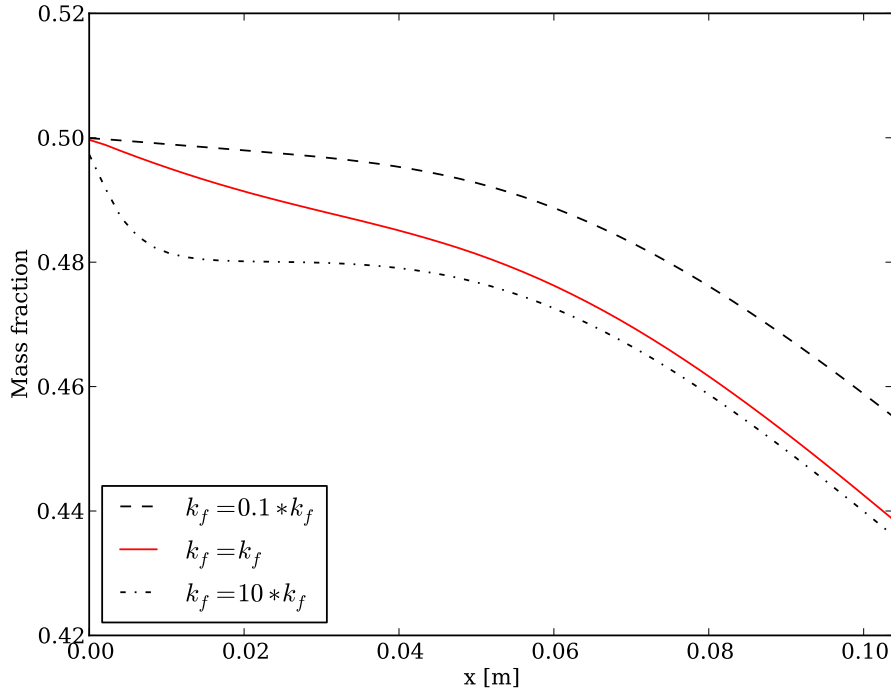


Figure 4.24: Mass fraction of N atom along plasma jet axis for varying inlet conditions.

Figure 4.25 shows the resultant temperature along the plasma jet for the various cases. It is seen that for the slow case, the temperature increase is relatively minimal. Interestingly, it reaches its maximal value (roughly  $x = 0.06$ ) before the standard case ( $x = 0.07$ ) yet well after the fast case ( $x = 0.04$ ). Similar to the behavior of the atomic mass fractions, the temperature for the slow case does not converge towards the values computed using standard  $k_f$ . Mirroring the behavior of the mass fraction, the fast case very quickly reaches its maximum temperature and proceeds to decrease along the axis as it converges towards the computed temperatures for the standard case. The drastically different behavior in temperature is expected, even with the relatively small differences in mass fraction, owing

to the dependence of temperature on the species production rate, per equations 2.33 and 2.34.

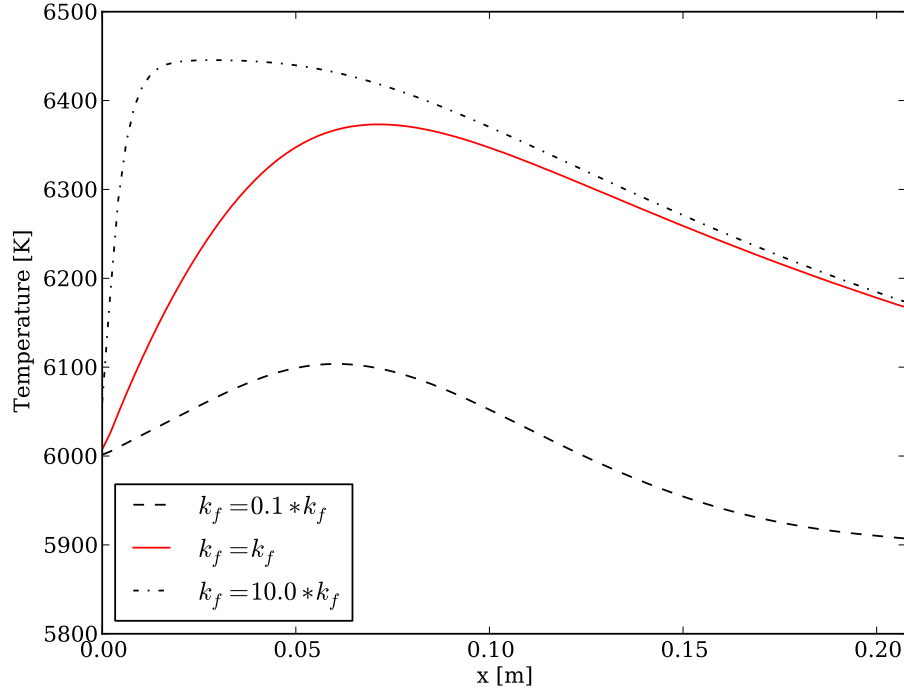


Figure 4.25: Temperature along plasma jet axis for varying values of  $k_f$ .

Figure 4.26 compares the computed, nonequilibrium mass fraction with the LTE values for the resultant temperature profile seen in figure 4.25 for the slow reaction rate of  $k_f = 0.1k_f$ . Owing to the temperature increase downstream from the inlet, the LTE mass fraction of N atom increases accordingly, but it is seen that the nonequilibrium values resulting from the overpopulated inlet condition remain significantly different from the LTE values across the domain. This is not unexpected: the slower reaction rates combined with the high speed of the jet result in a strongly nonequilibrium composition along the entire length of the jet. Owing to this result, if a test article were placed in this flow utilizing the slowed reaction rates, the boundary layer edge composition would be in nonequilibrium,

which could prevent the entire boundary layer from reaching equilibrium regardless of the conditions of the sample surface.

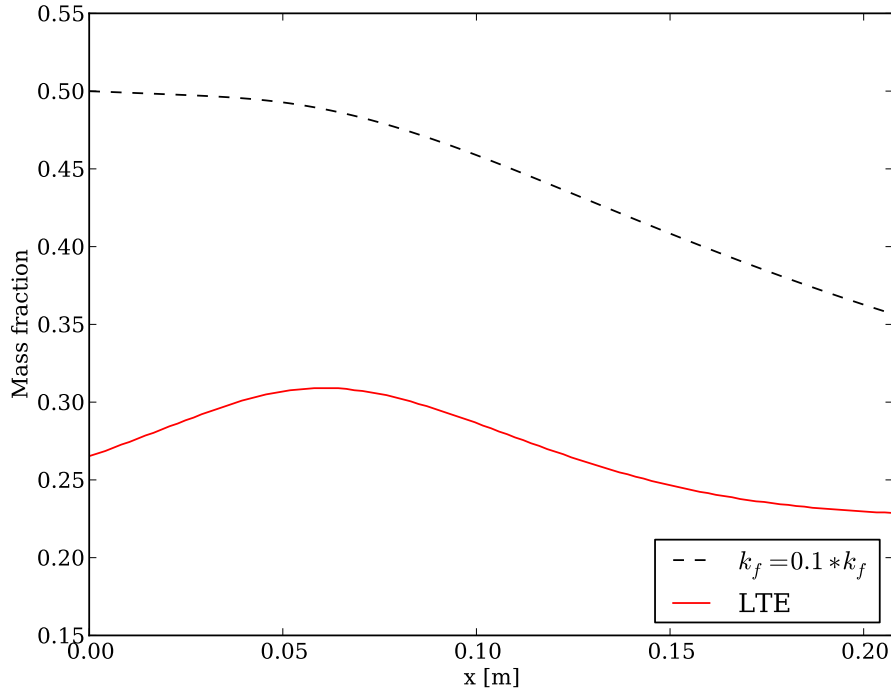


Figure 4.26: Mass fraction of N atom along plasma jet axis for  $k_f = k_f/10$ .

Figure 4.27 shows the computed nonequilibrium N atom mass fraction with the LTE values for the temperature profile from figure 4.25 for standard reaction rates. Comparing the nonequilibrium values seen here with those for  $0.1k_f$ , it is seen that the nonequilibrium population of N atom decreases noticeably faster. This faster recombination and resultant temperature increase cause the composition of the jet to tend towards equilibrium in a very visible manner. The sharp increase in temperature drives an increase in the LTE N atom mass fraction, reaching a maximum that coincides with the maximum temperature at approximately  $x = 0.07$ . Although standard reaction rates for N atom recombination result in a composition that is much closer to equilibrium, a test article placed in the flow

would likely feature a boundary layer with an edge composition that is at least weakly in nonequilibrium. Depending on the test article material and surface temperature, it is possible that the boundary layer would remain in nonequilibrium, however owing to the edge composition, the existence of an equilibrium boundary layer is more probably when applying standard reaction rates rather than artificially slowed rates.

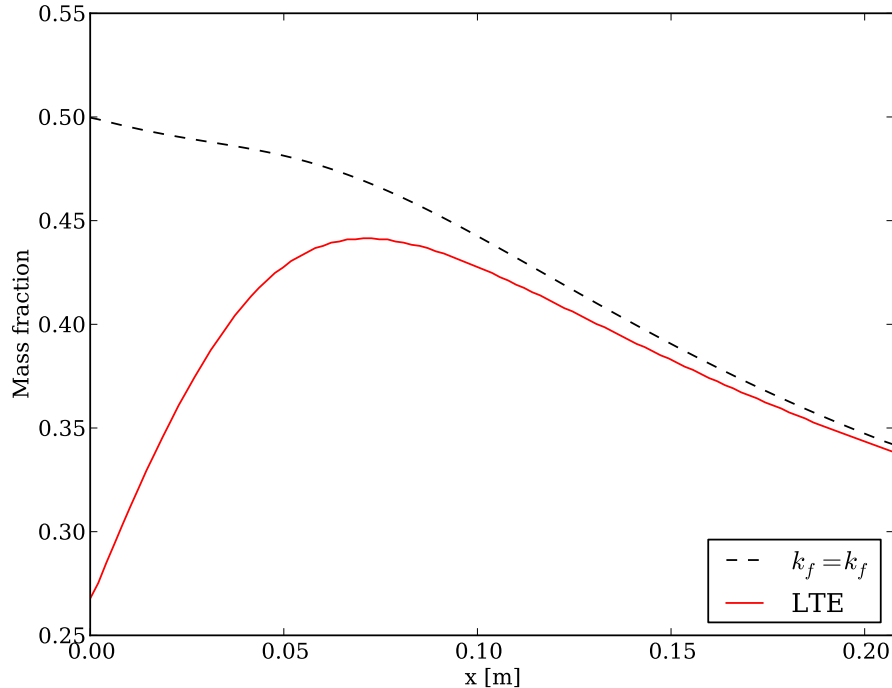


Figure 4.27: Mass fraction of N atom along plasma jet axis for  $k_f$  at published value.

Lastly, figure 4.28 shows computed nonequilibrium N atom mass fraction compared with the LTE values at the resultant temperature for the artificially increased reaction rate of  $k_f = 10k_f$ . Owing to the rapid recombination, a sharp temperature increase is observed in figure 4.25. Accordingly, after this rapid increase, the N atom mass fraction briefly stabilizes before beginning to decrease with increasing axial distance along the jet. This region of near-constant N atom mass fraction could be caused by the combination of the

upstream nonequilibrium composition balancing with the increase in temperature before the temperature decreases as the jet slowly dissipates along the axis. It can be seen that with a fast reaction rate and large temperature increase, the conditions in the jet reach an equilibrium condition around  $x = 0.03$  [m] from the inlet. Thus, if a sample were placed into this flow, the boundary layer edge would be in equilibrium.

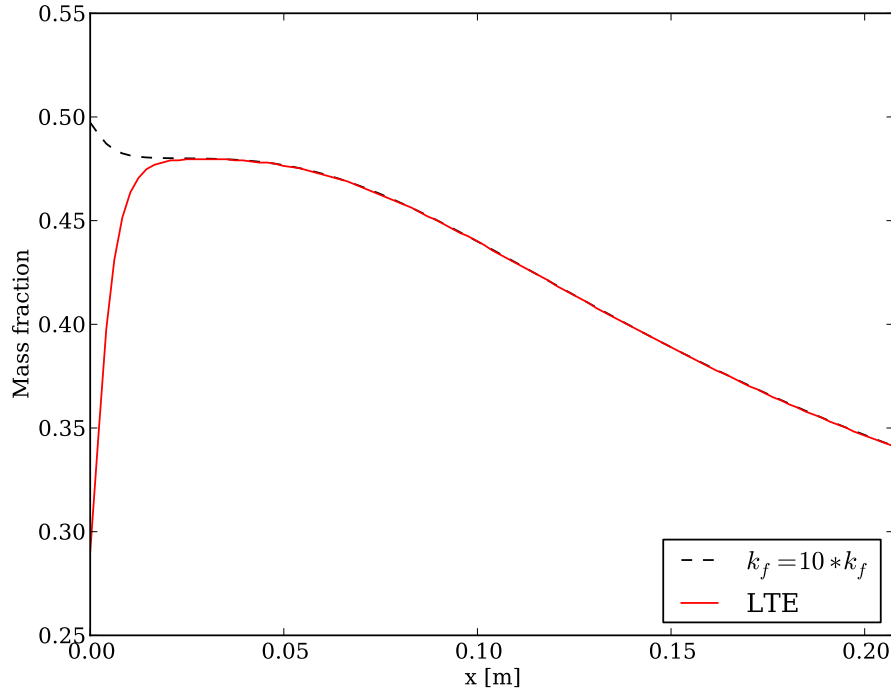


Figure 4.28: Mass fraction of N atom along plasma jet axis for  $k_f = 10k_f$ .

In this section, simulations were performed studying nitrogen atom mass fraction and temperature along the centerline of the plasma jet for artificially altered recombination rates for nitrogen recombination:  $k_f = \{0.1k_f, k_f, 10k_f\}$ . It was observed that with slowed rates, there is minimal temperature increase and the composition of the jet never reaches equilibrium as a result of the nonequilibrium inlet conditions dominating the composition of the jet faster than the gas phase chemistry is able to proceed towards equilibrium, resulting

in a strongly nonequilibrium flow throughout the jet. Using standard reaction rates, a more modest temperature increase was observed and N atom mass fraction trended towards equilibrium along the jet but did not fully achieve an LTE condition within the simulated domain. At the highest reaction rate,  $k_f = 10k_f$ , a drastic temperature increase was seen along with a rapid, yet initially small, shift in composition to equilibrium, resulting in the jet being in equilibrium from  $x = 0.03$  [m] onwards. These preliminary results suggest that for constant nonequilibrium inlet conditions, reaction rates for recombination play a vital role in the composition of flow despite the high speed of the jet and resultant low residence time.

#### 4.5.2 Effect of varying pressure on plasma jet composition and temperature

Simulations were performed utilizing standard reaction rates at pressures of 10 kPa, 15 kPa, 20 kPa, and 30 kPa. A table summarizing these conditions can be seen in Table 4.5. This represents a viable range of operating pressures for the UVM ICP facility. Unlike the method utilized in Section 4.5.1, the method used in this section can be replicated in an experimental facility and is completely physically meaningful.

Case	Pressure [Pa]
1	10132
2	15198
3	20264
4	30396

Table 4.5: Pressures used for  $\text{N}_2$  nonequilibrium simulations.

The previous method of varying reaction rates featured in identical inlet conditions which then changed as the jet evolved downstream. The approach of varying the operating

pressure of the jet results different inlet conditions, specifically different mixture densities for each pressure. While the downstream variations in temperature for varying reaction rates altered the gas density further along in the flow, the differences in inlet density result in flows with completely different Reynolds numbers. While the Reynolds numbers differ for the cases of different pressure, in all cases the flows remained laminar within the region simulated. At higher pressures and thus higher Reynolds numbers, it is believed that instabilities develop in the plasma jet, resulting in chaotic behavior which is not well-suited to materials testing.

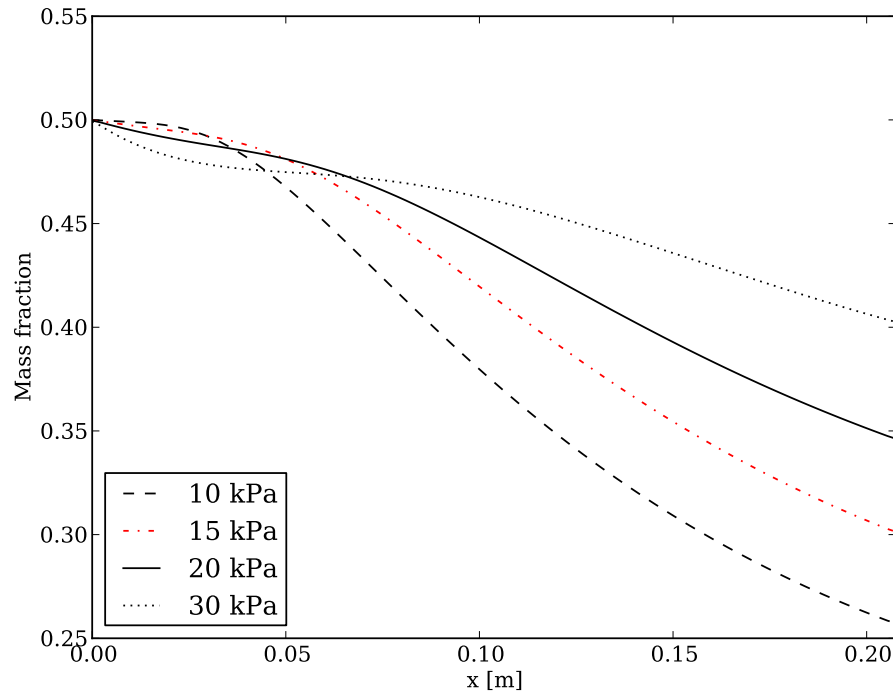


Figure 4.29: Mass fraction of N atom along plasma jet axis for varying pressures.

Figure 4.29 shows the computed N atom mass fraction along the jet centerline for the different pressure cases. It is seen that over the full length of the simulated domain, the degree of recombination is inversely proportional to the operating pressure of the jet. Figure

4.30 shows a zoomed view of the same data over the first 5 cm of the simulated region. Within the first 2 cm from the inlet, it is seen that recombination takes place in a more intuitive way, with the highest degree of recombination taking place for the highest pressure.

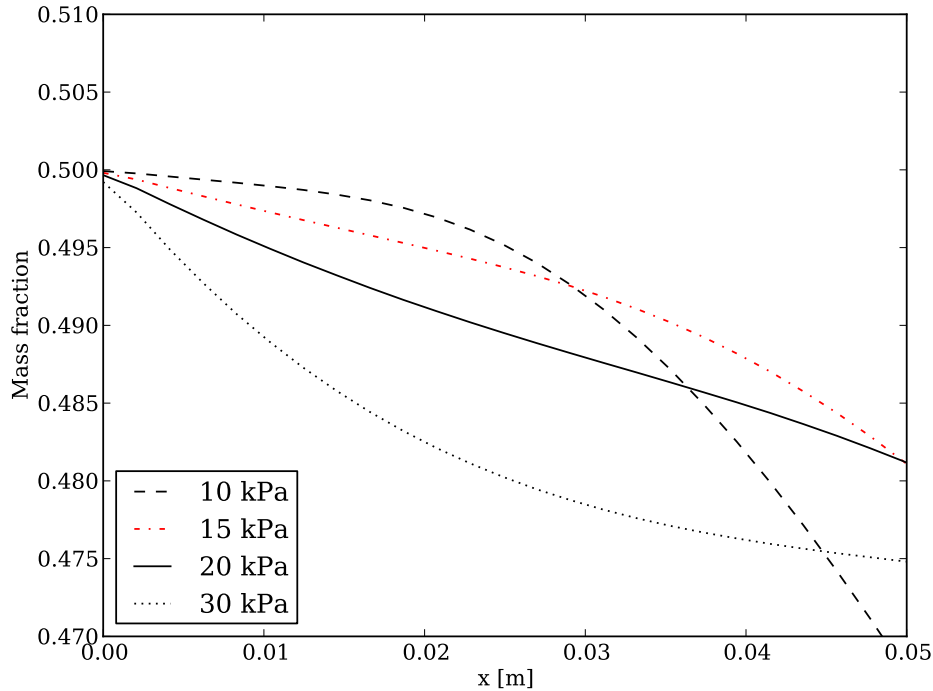


Figure 4.30: Mass fraction of N atom along plasma jet axis for varying pressures. Zoomed to the first 5 cm of the simulated domain to more clearly show nonequilibrium behavior near inlet.

The recombination behavior at different pressures is more easily understood when combined with the computed temperature profiles in figure 4.31. Similar to the simulations wherein reaction rates were varied, large differences are observed in the temperature profile along the jet centerline for different pressures. At the lowest pressure of 10 kPa, a very slight increase in temperature is seen. As pressure is increased, temperature downstream of the inlet increases. The computed temperature is a function of mixture enthalpy, mixture spe-

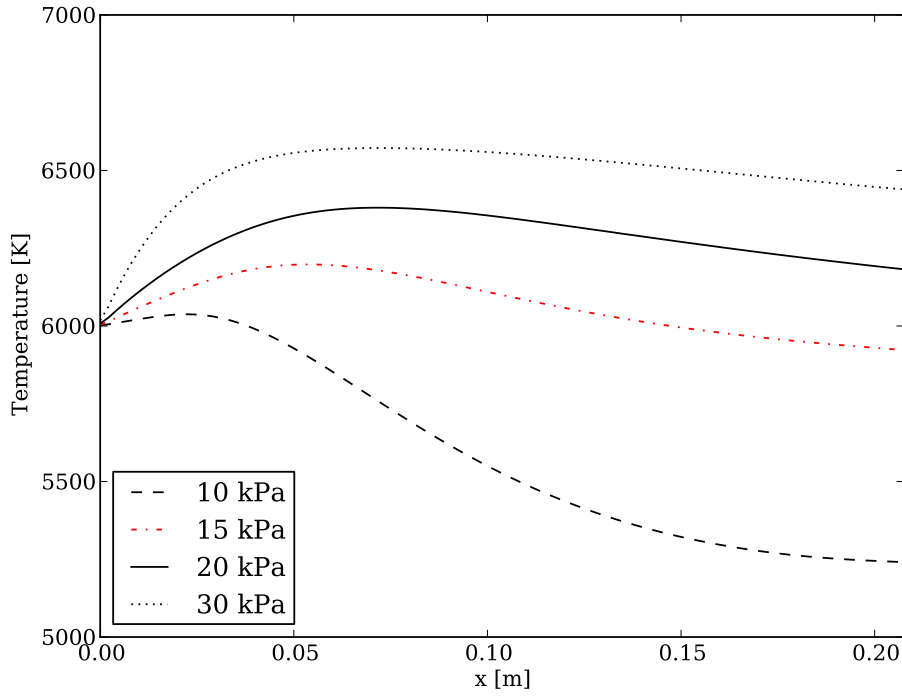


Figure 4.31: Temperature along plasma jet axis for varying pressures.

cific heat, and species production rates. Within the studied range of pressures and constant inlet temperature, neither the mixture enthalpy nor specific heat vary significantly. This suggests, unsurprisingly, that the temperature increase within the jet is a strong function of species production rates, which in turn are a function of the pressure or, more accurately, density of the mixture. As discussed in Section 1.1.2, there have been numerous studies which concluded that the conditions within the induction region are in equilibrium. If this were the case and the equilibrium condition held even at the quartz tube outlet, then the inlet composition specified for these simulations would be erroneous. In reality, it is probable that the inlet composition is 1) not in equilibrium; and 2) not as far from equilibrium as is simulated here. If these two points are valid, specifically the latter, then the temperature increase within the jet downstream of the inlet would likely be significantly less than what

is observed here.

Figure 4.32 shows the nonequilibrium N atom mass fraction compared with the equilibrium values at the resultant temperature at 10 kPa. It is seen that the computed nonequilibrium conditions from the overpopulated inlet remain far from equilibrium over the entire domain, despite the relatively high LTE N atom population that would exist due to the low pressure. At this low pressure, the species production rates appear to be sufficiently low to keep the composition strongly in nonequilibrium while at the same time causing very little temperature increase, as seen in Figure 4.31.

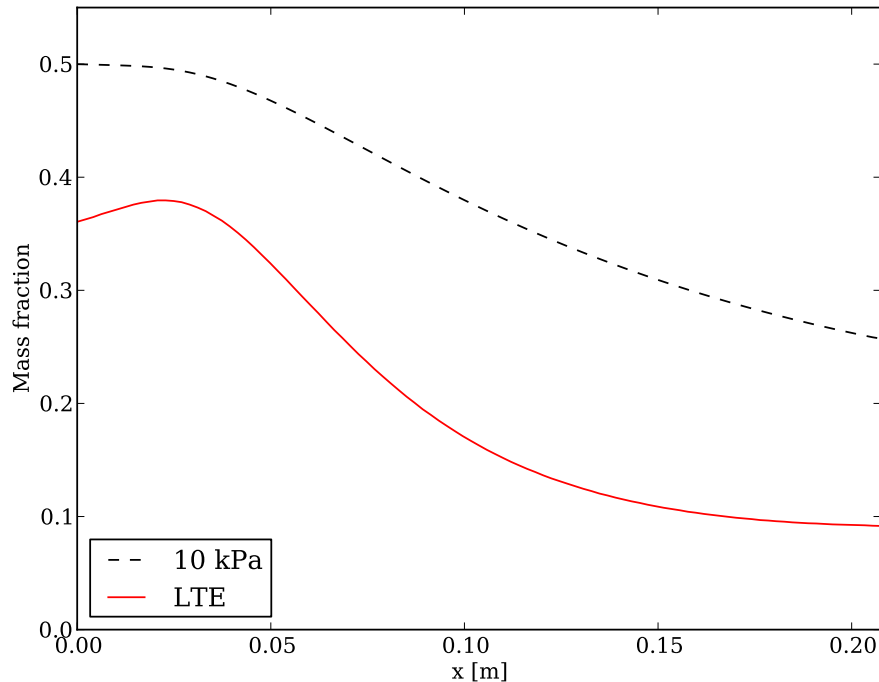


Figure 4.32: Nonequilibrium mass fraction of N atom along plasma jet axis compared to LTE values at 10132 Pa.

Figure 4.33 shows nonequilibrium N atom mass fraction overlaid with equilibrium mass fraction for the plasma jet at 15 kPa. At this pressure, it is seen that the equilibrium N

atom mass fraction at the inlet is significantly lower than the 10 kPa case, however the greater temperature increase in the freestream leads to a higher LTE population of N atom further downstream in the jet. At this pressure, the nonequilibrium conditions trend more clearly towards an LTE composition than the case of 10 kPa but they still do not fully achieve this within the simulated domain. With regard to the composition in roughly the middle of the domain where a test article would be placed ( $x \approx 10$  cm), the computed N atom mass fraction is still well out of equilibrium and would result in a nonequilibrium condition at the boundary layer edge.

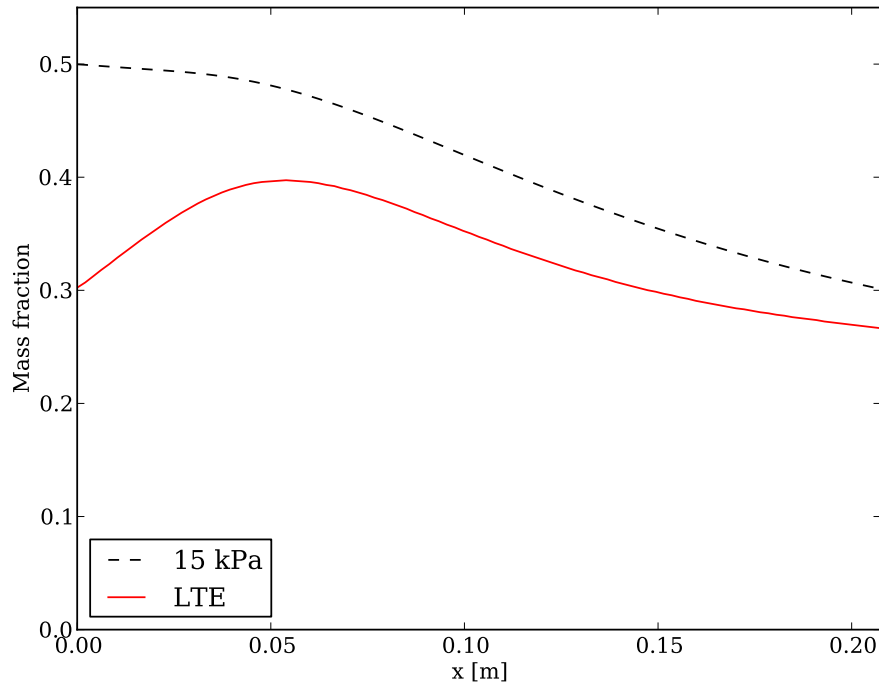


Figure 4.33: Nonequilibrium mass fraction of N atom along plasma jet axis compared to LTE values at 15198 Pa.

Figure 4.35 shows nonequilibrium N atom mass fraction overlaid with equilibrium mass fraction for the plasma jet at 20 kPa. This pressure is commonly used in the UVM ICP torch

facility and thus is indicative of experimental conditions. As is expected with increasing pressure, the equilibrium population of nitrogen atoms at the inlet decreases relative to the lower pressure cases but the maximum LTE population in the freestream is greater. The higher temperature is a direct result of the higher species production rates which occur at this increased pressure. As a consequence of this temperature, the nonequilibrium nitrogen population quickly converges towards the LTE values at the resultant temperature. For a typical experimental configuration with the test article approximately 10 centimeters from the inlet, the boundary layer edge would be weakly in nonequilibrium.

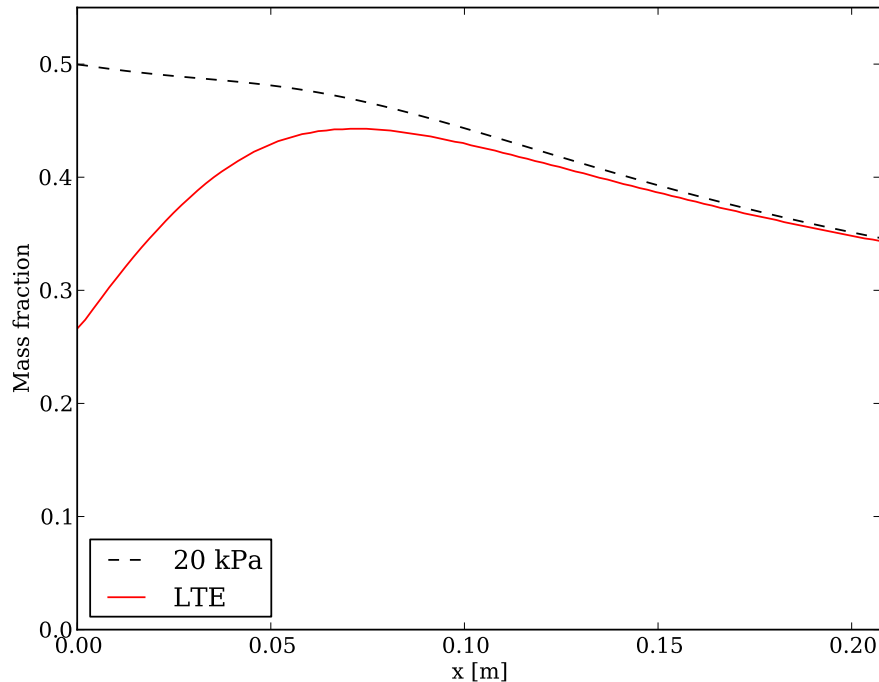


Figure 4.34: Nonequilibrium mass fraction of N atom along plasma jet axis compared to LTE values at 20264 Pa.

Figure 4.35 shows nonequilibrium N atom mass fraction overlaid with equilibrium mass fraction for the plasma jet at 30 kPa. Compared to the lower pressure cases, the decrease

in the nonequilibrium nitrogen population in the first 5 centimeters from the inlet is substantial. Owing to the high pressure, the recombination reactions proceed at a faster rate and hence release more energy into the flow. The combination of high pressure and resultant high temperature leads to the simulated nonequilibrium flow converging to the LTE composition at that temperature at approximately 8 centimeters from the inlet. If a test article were placed in this flow, its boundary layer edge would very likely be in equilibrium. However, while still a fairly low pressure, this configuration results in a flow regime prone to the instabilities discussed at the beginning of this section.

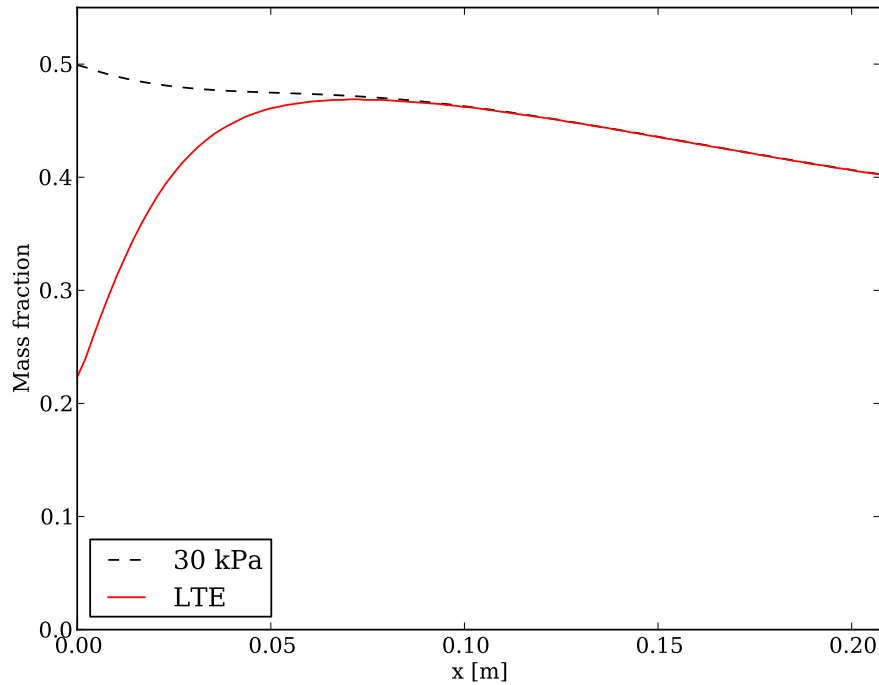


Figure 4.35: Nonequilibrium mass fraction of N atom along plasma jet axis compared to LTE values at 30396 Pa.

In this section, simulations were performed studying the effects of varying the plasma torch operating pressure on the composition and temperature of the plasma jet flow. It was

seen that at the lowest studied pressure of 10 kPa, the flow remained strongly in nonequilibrium and showed minimal temperature increase in the freestream from recombination reactions. At 15 kPa, a more marked temperature increase was observed and while the flow remained firmly in nonequilibrium, the trend suggests that over a longer domain the atomic nitrogen population would reach an LTE condition. At a pressure of 20 kPa, a temperature increase of approximately 400 K was observed and the atomic nitrogen population converged to equilibrium by the end of the domain, although at likely locations for a test article the flow was still weakly in nonequilibrium. At the maximum pressure studied of 30 kPa, a visible decrease in the nitrogen population occurred immediately downstream of the inlet in conjunction with a temperature increase of more than 500 K. The atomic nitrogen population converged to an equilibrium condition at approximately 8 cm downstream of the inlet and maintained this condition for the remainder of the domain. These simulations suggest that for the range of operating pressures used in typical experiments utilizing nitrogen in the UVM ICP torch facility, the boundary layer edge is at least weakly in nonequilibrium and thus the entirety of the boundary layer very likely experiences a nonequilibrium condition.

# Chapter 5

## Summary and future work

### 5.1 Contributions of this dissertation

A numerical model has been developed and implemented into the NGA CFD code for high temperature thermodynamic and transport properties, finite rate gas phase chemical kinetics, and surface catalytic efficiency in order to simulate the inductively coupled plasma torch facility at the University of Vermont. Thermodynamic properties are computed from statistical thermodynamics and transport properties are calculated from kinetic theory. This framework can simulate dissociated and ionized plasmas of arbitrary composition using any number of chemical species.

Validation of the plasma jet model has been undertaken by way of comparison to experimental measurements of temperature and relative species mole fractions in the boundary layer of a test article in oxygen-argon and nitrogen plasmas. Good agreement is seen between numerical and experimental results for cases with different surface temperatures and catalytic efficiencies. In cases where the agreement between results is poorer, the discrepancy can be attributed to scatter in the experimental data.

A code-to-code validation was performed benchmarking results from NGA to previously published results obtained with the code LEMANS using a nitrogen mixture and the UVM ICP torch geometry for varying catalytic efficiencies. Good agreement is seen

between the results for species concentrations and temperature at modest and high values of catalytic efficiencies. For non-catalytic surfaces, differences between the models are apparent and attributable to differences the gas phase reaction rates set between the codes.

Finally, a study was performed investigating the effects of varying recombination reaction rates and operating pressure on the behavior of a nitrogen plasma jet with a nonequilibrium inlet condition in order to determine the composition at the boundary layer edge for a test article. It was found that for standard reaction rates and normal operating pressures the boundary layer edge would exist in a mildly nonequilibrium state. Lower reaction rates and lower pressures resulted in a more strongly nonequilibrium composition. Conversely, higher pressures and faster reaction rates resulted in a plasma jet whose composition very quickly achieved an equilibrium condition.

## 5.2 Recommendations for future work

**Improvements in geometric capability.** At present, a major limitation in NGA is its inability to model irregular geometry. Coupling the framework developed in this dissertation with the capability to utilize level set and immersed boundary methods would provide the ability to simulate physically realistic test article geometries with rounded corners while maintaining simplicity in grid generation and, accordingly, obviating the need to alter the core of the flow solver. In addition, these methods would open the door for ablation modeling.

**Radiation modeling.** In nitrogen plasmas, interaction with a carbon surface at elevated temperatures results in the formation of the cyanogen radical,  $\text{CN}^-$  [59]. This molecule is a strong radiator and contributes significantly to the heat flux experienced on by a TPS material. A first step towards modeling radiative effects into NGA would be the introduction of a radiative equilibrium boundary condition wherein the heat transferred from the gas phase to the surface is balanced by heat radiated from the wall. This boundary condition would allow for more realistic simulation of wall temperature based on material emissivities.

The most thorough method to model radiation in NGA would be the inclusion of an external library such as NEQAIR.

**Electromagnetic forces.** The inclusion of models for the electromagnetic forces in the induction region of the ICP torch would allow for a more complete model of the facility. Detailed study of the fluid dynamics and chemistry that take place within the quartz tube could be performed, thus facilitating more realistic inlet conditions for the plasma jet and, by extension, better predictions of boundary layer temperature profiles and chemical compositions.

## Appendix A

# Reaction constants for O<sub>2</sub> / Ar hybrid mixture

Reaction	A	n	$\theta$ [K]
$O_2 + O \rightleftharpoons 2O + O$	$2.0(10^{21})$	-1.5	59,360
$O_2 + O_2 \rightleftharpoons 2O + O_2$	$2.0(10^{21})$	-1.5	59,360
$O + e^- \rightleftharpoons O^+ + e^- + e^-$	$3.9(10^{33})$	-3.78	158,500
$O + O \rightleftharpoons O_2^+ + e^-$	$1.1(10^{13})$	0.0	80,600
$Ar + e^- \rightleftharpoons Ar^+ + e^- + e^-$	$1.369(10^9)$	+0.5	135,300
$Ar + Ar \rightleftharpoons Ar^+ + Ar + e^-$	$3.056(10^{13})$	+0.5	135,300
$O_2 + Ar \rightleftharpoons 2O + Ar$	$2.0(10^{21})$	-1.5	59,700

Table A.1: Reaction rates for 7 species O<sub>2</sub>-Ar mixture.

## Appendix B

# Reaction constants for 5 species N<sub>2</sub> mixture

Reaction	A	n	$\theta$ [K]
$N_2 + N \rightleftharpoons 2N + N$	$3.0(10^{22})$	-1.6	113,200
$N_2 + N_2 \rightleftharpoons 2N + N_2$	$7.0(10^{21})$	-1.6	113,200
$N_2 + N_2^+ \rightleftharpoons 2N + N_2^+$	$7.0(10^{21})$	-1.6	113,200
$N_2 + N^+ \rightleftharpoons 2N + N^+$	$7.0(10^{21})$	-1.6	113,200
$N_2 + e^- \rightleftharpoons 2N + e^-$	$3.0(10^{24})$	-1.6	113,200
$N + e^- \rightleftharpoons N^+ + 2e^-$	$2.50(10^{34})$	-3.82	168,600
$N + N \rightleftharpoons N_2^+ + e^-$	$2.0(10^{13})$	0.0	67,500

Table B.1: Reaction rates for 5 species N<sub>2</sub> mixture.

## Appendix C

# Reaction constants for 5 species air mixture

Reaction	A	n	$\theta$ [K]
$N_2 + N \rightleftharpoons 2N + N$	$3.0(10^{22})$	-1.6	113,200
$N_2 + NO \rightleftharpoons 2N + NO$	$3.0(10^{22})$	-1.6	113,200
$N_2 + N_2 \rightleftharpoons 2N + N_2$	$7.0(10^{21})$	-1.6	113,200
$O_2 + N_2 \rightleftharpoons 2O + N_2$	$1.0(10^{22})$	-1.5	59,360
$O_2 + NO \rightleftharpoons 2O + NO$	$1.0(10^{22})$	-1.5	59,360
$O_2 + O_2 \rightleftharpoons 2O + O_2$	$1.0(10^{22})$	-1.5	59,360
$N_2 + O \rightleftharpoons NO + N$	$5.69(10^{12})$	+0.42	42,938
$O_2 + N \rightleftharpoons NO + O$	$2.49(10^9)$	+1.18	4005.5
$NO + NO \rightleftharpoons N + O + NO$	$5.0(10^{15})$	0.0	75,500
$NO + N \rightleftharpoons N + N + O$	$5.0(10^{15})$	0.0	75,500
$NO + O \rightleftharpoons N + O + O$	$5.0(10^{15})$	0.0	75,500

Table C.1: Reaction rates for 5 species air mixture.

# References

- [1] Gupta, R., Yos, J., Thompson, R. & Lee, K. A Review of Reaction Rates and Thermodynamic and Transport properties for an 11-species Air Model for Chemical and Thermal Nonequilibrium Calculations to 30,000 K. Tech. Rep., NASA (1990).
- [2] Owens, W. *Development of a 30kW Inductively-coupled Plasma Torch for High Temperature Aerospace Material Testing at UVM*. Master's thesis, University of Vermont (2011).
- [3] Desjardins, O., Blanquart, G., Balarac, G. & Pitsch, H. High order conservative finite difference scheme for variable density low Mach number turbulent flows. *Journal of Computational Physics* **227**, 7125–7159 (2008).
- [4] Owens, W. private communication (December 2015).
- [5] Owens, W. *Aero-Thermal Characterization of Silicon Carbide Flexible TPS using a 30kW ICP Torch*. Ph.D. thesis, University of Vermont (2015).
- [6] Meyers, J., Owens, W. & Fletcher, D. Surface catalyzed reaction efficiencies in nitrogen and oxygen plasmas from laser induced fluorescence measurements (2013).
- [7] Allen, H. J. & Eggers, A. J. A Study of the motion and aerodynamic heating of ballistic missiles entering the Earth's atmosphere at high supersonic speeds. Tech. Rep., National Advisory Committee for Aeronautics (1958).

- [8] Lees, L. Laminar Heat Transfer Over Blunt-Nosed Bodies at Hypersonic Flight Speeds. *Jet Propulsion* 259–269 (1956).
- [9] Fay, J. & Riddell, F. Theory of Stagnation Point Heat Transfer in Dissociated Air. *Journal of the Aeronautical Sciences* **25**, 73–85 (1958).
- [10] Goulard, R. On Catalytic Recombination Rates in Hypersonic Stagnation Heat Transfer. In *ARS 12th Annual Meeting*, 737–745 (1958).
- [11] Mostaghimi, J., Proulx, P. & Boulos, M. I. A two-temperature model of the inductively coupled rf plasma. *Journal of applied physics* **61**, 1753–1760 (1987).
- [12] Gnoffo, P. A., Weilmuenster, K. J., Hamilton, H. H., Olynick, D. R. & Venkatapathy, E. Computational aerothermodynamic design issues for hypersonic vehicles. *Journal of Spacecraft and Rockets* **36**, 21–43 (1999).
- [13] Cheatwood, F. M. & Gnoffo, P. A. *User's manual for the Langley Aerothermodynamic Upwind Relaxation Algorithm (LAURA)* (National Aeronautics and Space Administration, Langley Research Center, 1996).
- [14] Sutton, K. & Gnoffo, P. Multi-component diffusion with application to computational aerothermodynamics. In *7th AIAA/ASME Joint Thermophysics and Heat Transfer Conference* (1998).
- [15] Riley, C. J. & Cheatwood, F. M. Distributed-memory computing with the langley aerothermodynamic upwind relaxation algorithm (LAURA). *Advances in Engineering Software* **29**, 317–324 (1998).
- [16] Gnoffo, P. A. *et al.* Functional equivalence acceptance testing of fun3d for entry, descent, and landing applications. *AIAA Paper* **2558**, 24–27 (2013).

- [17] Mazaheri, A., Bruce III, W. E., Mesick, N. J. & Sutton, K. Methodology for flight-relevant arc-jet testing of flexible thermal protection systems. *Journal of Spacecraft and Rockets* 1–12 (2014).
- [18] Wright, M. J., Candler, G. V. & Bose, D. Data-Parallel Line Relaxation Method for the Navier Stokes Equations Introduction **36** (1998).
- [19] Marschall, J. & Maclean, M. Finite rate surface chemistry model, i: Formulation and reaction system examples. In *42nd AIAA Thermophysics Conference* (2011).
- [20] Palmer, G. E., White, T. & Pace, A. Direct coupling of the NEQAIR radiation and DPLR CFD codes. *Journal of Spacecraft and Rockets* **48**, 836–845 (2011).
- [21] Pekakovic, D. A., Marschall, J., Duan, L. & Martin, M. P. Nitric oxide production from surface recombination of oxygen and nitrogen atoms. *Journal of Thermophysics and Heat Transfer* **22**, 178–186 (2008).
- [22] Bottin, B. *Aerothermodynamic Model of an Inductively-Coupled Plasma Wind Tunnel*. Ph.D. thesis, Von Karman Institute (1999).
- [23] Degrez, G., Vanden Abeele, D., Barbante, P. & Bottin, B. Numerical simulation of inductively coupled plasma flows under chemical non-equilibrium **14** (2002).
- [24] Gnoffo, P. & Gupta, R. Conservation equations and physical models for hypersonic air flows in thermal and chemical nonequilibrium. Tech. Rep., NASA.
- [25] Selle, S. & Riedel, U. Transport coefficients of reacting air at high temperatures. In *AIAA Reno 2000* (2000).
- [26] Barbante, P. F. Computation of Nonequilibrium High-Temperature Axisymmetric Boundary Layer Flows. *Journal of Thermophysics and Heat Transfer* **16**, 490–497 (2002).

- [27] Barbante, P. F. *Accurate and Efficient Modelling of High Temperature Nonequilibrium Air Flows*. Ph.D. thesis.
- [28] Kolesnikov, A., Pershin, I. & Vasil'evskii, S. Catalycity tests of Si-based TPM in dissociated CO<sub>2</sub> mixture and extrapolation from ground to entry conditions in the Martian atmosphere. In *3rd International Symposium on Atmospheric Reentry Vehicles and Systems* (2003).
- [29] Magin, T. *A model for inductive plasma wind tunnels*. Ph.D. thesis (2004).
- [30] Rini, P., Degrez, G. & Vanden Abeele, D. Elemental Demixing in Inductively Coupled Air Plasma Torches at High Pressures. *Journal of Thermophysics and Heat Transfer* **20**, 31–40 (2006). URL <http://doi.aiaa.org/10.2514/1.15884>.
- [31] Lani, A. *et al.* Numerical study of elemental demixing in atmospheric entry flow regimes near local thermodynamic equilibrium. In *European Conference on Computational Fluid Dynamics* (ECOOMAS, The Netherlands, 2006).
- [32] Rini, P. & Degrez, G. Elemental Demixing in Air and Carbon Dioxide Stagnation Line Flows **18** (2004).
- [33] Fletcher, D. G., Thömel, J., Chazot, O. & Marschall, J. Realization of a Gas-Surface Interaction Test Case for Model Validation (2009).
- [34] Chazot, O. P. An integrated experimental and computational study of heating due to surface catalysis under hypersonic conditions. Tech. Rep., DTIC Document (2012).
- [35] Candler, G., Johnson, H. & Drayna, T. DNS of transitional flows on cones at hypersonic conditions. In *ESA Special Publication*, vol. 692, 153 (2011).
- [36] Lani, A. *An object oriented and high performance platform for aerothermodynamics simulation*. Ph.D. thesis, von Karman Institute for Fluid Dynamics (2008).

- [37] Barbante, P. F. Reacting flows simulation with applications to ground to flight extrapolation Local Heat Transfer Simulation for Stagnation Point. In *RTO-EN-AVT-142*, 1–20 (2007).
- [38] Anna, A. *Numerical Modeling of Surface Chemistry Processes for Hypersonic Entry Environments*. Ph.D. thesis, University of Michigan (2013).
- [39] Scalabrin, L. C. & Boyd, I. D. Numerical simulation of weakly ionized hypersonic flow for reentry configurations. *AIAA Paper* **3773**, 2006 (2006).
- [40] Pierce, C. D. *Progress Variable Approach for Large-Eddy Simulation of Turbulent Combustion*. Ph.D. thesis, Stanford University (2001).
- [41] Falgout, R., Jones, J. & Yang, U. *hypre*, a library of parallel high performance preconditioners. *Computational Science* **2331**, 632–641 (2002).
- [42] Liu, X.-D., Osher, S. & Chan, T. Weighted essentially non-oscillatory schemes. *Journal of computational physics* **115**, 200–212 (1994).
- [43] Jiang, G.-S. & Shu, C.-W. Efficient implementation of weighted eno schemes. *Journal of computational physics* **126**, 202–228 (1996).
- [44] Colonius, T. & Ran, H. A super-grid-scale model for simulating compressible flow on unbounded domains. *Journal of Computational Physics* **182**, 191–212 (2002).
- [45] Byrne, G. & Thompson, S. DVODE documentation. URL <http://www.radford.edu/~thompson/vodef90web/>.
- [46] Liang, L., Puduppakkam, K. & Meeks, E. Towards using realistic chemical kinetics in multidimensional cfd. In *Nineteenth International Multidimensional Engine Modeling User's Group Meeting* (2009).

- [47] Magin, T. E. & Degrez, G. Transport algorithms for partially ionized and unmagnetized plasmas. *Journal of Computational Physics* **198**, 424–449 (2004). URL <http://linkinghub.elsevier.com/retrieve/pii/S0021999104000361>.
- [48] Vincenti, W. & Kruger, C. *Introduction to Physical Gas Dynamics* (Krieger Publishing Co., 1967), 2nd edn.
- [49] Palmer, G. & Wright, M. J. Comparison of Methods to Compute High-Temperature Gas Viscosity. *Journal of Thermophysics and Heat Transfer* **17**, 232–239 (2003).
- [50] Jeans, J. *An Introduction to the Kinetic Theory of Gases* (Cambridge University Press, 1960), 6th edn.
- [51] Goldstein, M. New formulation of the multicomponent laminar boundary-layer problem. *Physics of Fluids (1958-1988)* **10**, 823–830 (1967).
- [52] Desjardins, O. CTFLab - NGA (2014). URL <http://ctflab.mae.cornell.edu/nga.html>. Online, accessed 2014-08-20.
- [53] Rini, P. *Analysis of differential diffusion phenomena in high enthalpy flows, with application to thermal protection material testing in ICP facilities*. Ph.D. thesis (2006).
- [54] Smith, S. F. *Investigations of subsonic and supersonic flow characteristics of an inductively coupled plasma torch*. Master's thesis.
- [55] Anna, A., Alkandry, H. & Boyd, I. Computational modeling of gas-surface interactions for high-enthalpy reacting flows. In *51st AIAA Aerospace Sciences Meeting including the New Horizons Forum and Aerospace Exposition* (2013).
- [56] Owens, W., Meyers, J. & Fletcher, D. Surface catalysis and oxidation of flexible thermal protection materials in air plasma. In *44th AIAA Thermophysics Conference* (2013).
- [57] Owens, W., Meyers, J., AJ, L., Smith, S. & Fletcher, D. Direct Assessment of Surface-Catalyzed Reaction Efficiencies. In *STO-MP-AVT-199* (2012).

- [58] Park, C. Review of chemical-kinetic problems of future NASA missions, I: Earth entries. *Journal of Thermophysics and Heat transfer* **7**, 385–398 (1993).
- [59] Lutz, A. J., Owens, W., Meyers, J., Fletcher, D. & Marschall, J. *Investigation of CN production from carbon materials in nitrogen plasmas*. Master's thesis, University of Vermont (2011).
- [60] Aessopos, A. Similarity transformation methods in the analysis of the two dimensional steady compressible laminar boundary layer. Tech. Rep. 1 (2004).
- [61] Anna, A. & Boyd, I. D. Computation of Surface Catalysis for Graphite Exposed to High-Enthalpy Nitrogen Flow. In *50th AIAA Aerospace Sciences Meeting*, January, 1–14 (2012).
- [62] Bane, S. P. M., Ziegler, J. L. & Shepherd, J. E. Development of One-Step Chemistry Models for Flame and Ignition Simulation. Tech. Rep., GALCIT (2010).
- [63] Barbante, P. F. Heat Flux Duplication Between Ground Facility and Hypersonic Flight. *Journal of Thermophysics and Heat Transfer* **23**, 684–692 (2009). URL <http://doi.aiaa.org/10.2514/1.35808>.
- [64] Barbante, P. F. Accurate and Efficient Modelling of High Temperature Nonequilibrium Air Flows .
- [65] Bergeron, D. A Research Code to Study Solutions of the Boundary Layer Equations in Body Conformal Coordinates. Tech. Rep., National Defense Canada (1991).
- [66] Boersma, B. J. A staggered compact finite difference formulation for the compressible Navier Stokes equations. *Journal of Computational Physics* **208**, 675–690 (2005).
- [67] Bose, D., Mccorkle, E. & Thompson, C. Analysis and Model Validation of Shock Layer Radiation in Air. In *46th AIAA Aerospace Sciences Meeting* (2008).

- [68] Bose, D., Palmer, G. & Wright, M. Uncertainty Analysis of Laminar Aeroheating Predictions for Mars Entries. *Journal of Thermophysics and Heat Transfer* **20**, 652–662 (2006). URL <http://doi.aiaa.org/10.2514/1.20993>.
- [69] Brémare, N., Hyun, S. Y., Studer, D., Boubert, P. & Vervisch, P. Radiation and Chemistry of CO<sub>2</sub> and Air Inductive Plasmas as Freejets and in Interaction with Samples. *7th European Symposium on Aerothermo for Space Vehicles* (2010).
- [70] Building, G. B. Numerical Solution of Boundary Layer Equations Example : Development of a Flat-Plate Boundary Layer (2008).
- [71] Burr, K., Akylas, T. & Mei, C. Two-Dimensional Laminar Boundary Layers. 1–33.
- [72] Carter, J., Edwards, D. E. & Werle, M. A New Coordinate Transformation for Turbulent Boundary Layer Flows. Tech. Rep., United Technologies Research Center.
- [73] Chabut, E. & Lengrand, J. C. A Comparison of Different Numerical Approaches for Calculating a Martian Entry Flow. In *European Conference for Aerospace Sciences*.
- [74] Chazot, O. Experimental Studies on Hypersonic Stagnation Point Chemical Environment. In *RTO-EN-AVT-142* (2007).
- [75] Chen, Y.-k. & Milos, F. S. Navier Stokes Solutions with Finite Rate Ablation for Planetary Mission Earth Reentries. *Journal of Spacecraft and Rockets* **42** (2005).
- [76] Copeland, R., Pallixt, J. B. & Stewart, D. A. Surface-Catalyzed Production of NO from Recombination of N and O Atoms. *Journal of Thermophysics and Heat Transfer* **12** (1998).
- [77] Fletcher, D. G., Lutz, A. J., Meyers, J. M., Owens, W. P. & Uhl, J. Species and Temperature Gradient Measures in the Reacting Boundary Layer over ICP Test Samples. In *7th European Symposium on Aerothermodynamics for Space Vehicles* (2011).

- [78] Fletcher, D. G. & Playez, M. Characterization of Supersonic and Subsonic Plasma Flows (2006).
- [79] Henningson, D. S. & Berggren, M. Fluid Dynamics : Theory and Computation (2005).
- [80] Hunt, R. & Wilks, G. Continuous Transformation Computation of Boundary Layer Equations between Similarity. *Journal of Computational Physics* **40**, 478–490 (1981).
- [81] Jameson, A., Schmidt, W. & Turkel, E. Numerical Solution of the Euler Equations by Finite Volume Methods Using Runge-Kutta Time-Stepping Schemes. Tech. Rep., Princeton University.
- [82] Keller, H. B. Numerical methods in boundary-layer theory. *Ann. Rev. Fluid Mech.* **10**, 417–433 (1978).
- [83] Lam, S. H. H. The Prandtl Boundary Layer Theory (2004).
- [84] Loyd, B. & Murman, E. M. Finite Volume Solution of the Compressible Boundary-Layer Equations. Tech. Rep., NASA (1986).
- [85] Magin, T. Physico-chemical Models for High Enthalpy and Plasma Flows (2009).
- [86] Kreyszig, E. *Advanced Engineering Mathematics* (John Wiley & Sons, 2006), 9th edn.
- [87] White, F. *Viscous Fluid Flow* (McGraw-Hill, Inc, 1974), 1st edn.
- [88] Giordano, N. J. & Nakanishia, H. *Computational Physics* (Pearson Prentice Hall, 2006), 2nd edn.
- [89] Owens, W., Meyers, J. & Fletcher, D. Direct Assessment of Surface-Catalyzed Reaction Efficiency (2012).
- [90] Nourgaliev, R. & Theofanous, T. High fidelity interface tracking in compressible flows: Unlimited anchored adaptive level set. *Journal of Computational Physics* 836–866 (2006).

- [91] Scalabrin, L. & Boyd, I. Development of an unstructured navier-stokes solver for hypersonic nonequilibrium aerothermodynamics. In *38th AIAA Thermophysics Conference* (2005).
- [92] Fletcher, D. private communication (June 2014).
- [93] Rini, P., Abeele, D. V. & Degrez, G. Closed form for the equations of chemically reacting flows under local thermodynamic equilibrium. *Physical Review E* **72**, 011204 (2005).
- [94] Sarma, G. Physico-chemical modelling in hypersonic flow simulation. *Progress in Aerospace Sciences* **36**, 281–349 (2000).
- [95] Olejniczak, J. & Fletcher, D. An experimental and computational study of the freestream conditions in an arc-jet facility. In *31st AIAA Plasmadynamics and Lasers Conference* (AIAA, 2000).